3D segmentation and registration for minimal invasive prostate cancer therapy

Ke Wu

▶ To cite this version:

Ke Wu. 3D segmentation and registration for minimal invasive prostate cancer therapy. Signal and Image processing. Université de Rennes, 2014. English. ⟨NNT : 2014REN1S015⟩. ⟨tel-00962028v2⟩

HAL Id: tel-00962028
https://theses.hal.science/tel-00962028v2

Submitted on 29 Aug 2014

THÈSE / UNIVERSITÉ DE RENNES 1
sous le sceau de l'Université Européenne de Bretagne

pour le grade de

DOCTEUR DE L'UNIVERSITÉ DE RENNES 1

Mention : Traitement du Signal et Télécommunications

Ecole doctorale MATISSE

présentée par

WU Ke

Préparée à l'unité de recherche LTSI – INSERM U1099
Laboratoire de Traitement du Signal et de l'Image
UFR ISTIC

3D Segmentation and Registration for Minimal Invasive Prostate Cancer Therapy

**Thèse soutenue à Rennes
le 5 Mars 2014**

devant le jury composé de :

CHAPELON Jean-Yves
DR INSERM, Labtau INSERM U1032, Lyon, France
/ *président*

BETROUNI Nacim
CR INSERM, Unité INSERM U703, Loos, France /
rapporteur

KOUAME Denis
PU, IRIT-UMR 5505, Université Paul Sabatier,
Toulouse, France / *rapporteur*

BLANC Emmanuel
Directeur R&D, EDAP, Vaulx-en-Velin, France /
examinateur

DILLENSEGER Jean-Louis
MC-HDR, LTSI, INSERM U1099, Université de
Rennes 1, France / *directeur de thèse*

SHU Huazhong
PU, LIST, SouthEast University, Nanjing, Chine / *co-
directeur de thèse*

Acknowledgements

WU Ke

January, 2014

Résumé étendu de la Thèse en français

Partie I : Contexte de l'étude et des travaux menés durant la Thèse

Chapitre 1 : Contexte de l'étude : le traitement du cancer de la prostate.

Le cancer de la prostate est le deuxième cancer le plus diagnostiqué dans le monde. Par exemple, en 2008, il représentait 14 % (903 500) des nouveaux cas de cancer. Il représente également la 6ème cause de mortalité par cancer chez les hommes (Jemal, Bray et al. 2011). De plus, environ un tiers des patients diagnostiqués présente en plus un ou plusieurs symptômes, comme des mictions fréquentes, la nycturie (miction accrue la nuit), la difficulté à commencer et à maintenir un flux constant d'urine, hématurie (sang dans l'urine), et la dysurie (douleur de miction). Le cancer de la prostate peut également causer des problèmes liés la fonction sexuelle telle la difficulté à atteindre l'érection ou l'éjaculation douloureuse.

Généralement le cancer de la prostate débute lorsque des cellules normales de la prostate mutent en cellules cancéreuses. Statistiquement, l'adénocarcinome de la prostate est le plus courant dans la zone périphérique. Dans un premier temps, ces cellules cancéreuses sont localisées dans les glandes prostatiques normales. C'est la condition connue sous le nom de carcinome in situ ou néoplasie intra-épithéliale prostatique. Après cette période de début, les cellules cancéreuses commencent à se multiplier et à se propager aux tissus environnants et forment ainsi la tumeur. Celle-ci continue à croître jusqu'à atteindre et envahir les organes voisins tels que les vésicules séminales, la vessie ou le rectum. Les cellules tumorales ont alors la capacité de voyager avec le sang ou le système lymphatique et peuvent entraîner des métastases.

Même si c'est actuellement un sujet de controverse, dans les pays occidentaux, pour les personnes de plus de cinquante ans, un dépistage systématique est programmé en utilisant principalement le toucher rectal ou/et la mesure du taux de PSA, l'antigène spécifique de la prostate. Si ces tests présentent quelques soupçons de cancer de la prostate, des examens complémentaires comme les biopsies ou l'imagerie seront effectués pour confirmer ou infirmer les soupçons. Ces examens complémentaires sont également utilisés pour classifier les tumeurs selon leur extension anatomique.

Les techniques d'imagerie de la prostate les plus courantes sont l'échographie et l'IRM.

- L'échographie transrectale (TRUS), fournit des images de la glande de la

prostate et les tissus environnants. Dans l'étape de diagnostic, l'échographie est utilisée pour préparer la biopsie en essayant de définir les zones potentielles des tumeurs. Cependant, les lésions tumorales apparaissent avec une échogénicité variable. Dans la plupart des cas, il reste difficile de différencier les différentes zones de la prostate et des tissus environnants. Son usage en diagnostic est assez restreint, mais comme l'échographie est très répandue, et permet une imagerie en temps réel cette modalité est largement utilisée dans le contexte des thérapies guidées par l'image.

- Parmi les différentes modalités d'imagerie utilisées pour l'exploration des tumeurs de la prostate, seule l'IRM permet de visualiser l'anatomie avec une résolution et un contraste suffisants pour discriminer la tumeur dans le volume de la prostate. De nouveaux protocoles ont été développés en IRM pour la détection des cancers de la prostate (spectrocopy imaging –MRSI–, diffusion weighted imaging – DWI– ou dynamic contrast-enhanced imaging – DCE MIR –) car ils améliorent la précision du diagnostic et l'estimation du stade du cancer.

Si après une surveillance active, une thérapie semble nécessaire, plusieurs approches peuvent être proposées : la prostatectomie radicale, la cryogénie, la radiothérapie, la curiethérapie, la thérapie ultrasonore, … La tendance de ces thérapies est de proposer des gestes de moins en moins invasifs , à accès minimal. Cette tendance a pu se mettre en œuvre par la part de plus en plus importante de l'image et de l'informatique dans la procédure thérapeutique. La finesse de ces dernières thérapies permet maintenant d'envisager des traitements localisés à la tumeur en préservant les structures saines de la prostate et donc en minimisant les effets secondaires liés aux traitements (trouble de l'érection, trouble urinaire, etc.).

Chapitre 2 : traitement par ultrasons focalisés et position du problème de guidage par l'image. Trame et justification des travaux de recherche de la Thèse.

Le travail de Thèse s'est déroulé dans le cadre du projet ANR TECSAN MULTIP (Mari, Bouchoux et al. 2013), en collaboration avec la société IMSONIC, le LabTau INSERM U1032 et la société EDAP. La société EDAP propose un procédé d'ablation de la prostate par ultrasons focalisés à haute intensité (HIFU), l'Ablatherm[1], utilisé en routine clinique. Le principe de l'Ablatherm est d'utiliser un transducteur ultrasonore en forme de cuillère. Ce transducteur émet des ultrasons de hautes intensités qui se concentrent en un point focal. L'énergie ultrasonore déposée en ce point focal est transformée en énergie thermique. L'échauffement du tissu en ce point se traduit ensuite par une nécrose. Le transducteur est en fait composé de différents éléments qui peuvent être pilotés électriquement de manière indépendante. En jouant sur le déphasage des signaux entre les différents éléments et sur la position de la sonde, il est possible de défléchir le point focal sur l'ensemble du volume de la zone à nécroser, la prostate en l'occurrence. Cette thérapie est guidée par l'image. Au centre de la sonde de thérapie, soit une sonde d'imagerie, soit une zone d'éléments dual mode (thérapie et imagerie) permet de prendre une image échographique de la prostate.

Le thérapie se déroule de la manière suivante (Figure 1) : 1) dans un premier temps, la sonde d'imagerie échographique fait l'acquisition du volume de la prostate à traiter et des organes environnants ; 2) sur ce volume d'imagerie l'urologue définit de manière interactive la zone à traiter sous la forme d'une juxtaposition de tâches focales ; 3) l'Ablatherm échauffe ensuite automatiquement la zone définie par l'urologue. Ce traitement peut être effectué en une passe ou en plusieurs passes afin de corriger manuellement la déformation de la prostate due à l'œdème provoqué par l'échauffement.
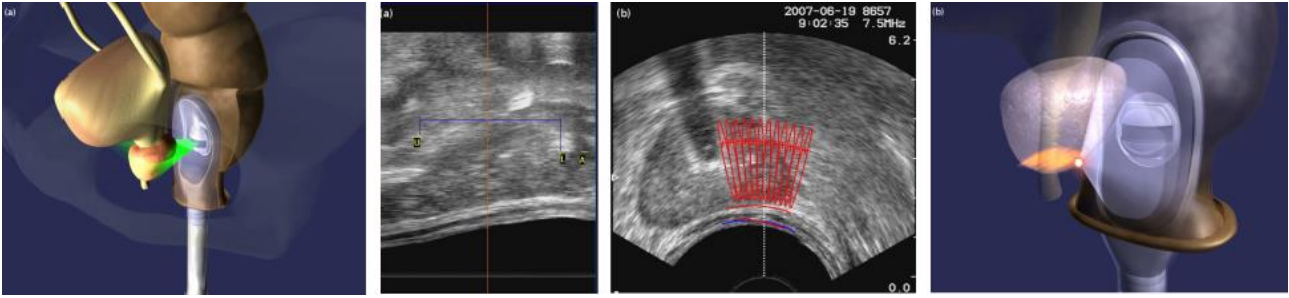
---

1   http://www.edap-tms.com

Figure 1 : Éléments d'une thérapie ultrasonore : acquisition du volume échographique ;
délimitation de la zone de traitement ; planning de traitement sur le volume échographique ;
traitement selon le planning. (Images EDAP .http://www.edap-tms.com).

Les avancées sur cette thérapie, en particulier sur la sonde (sonde sectorielle, sonde dual mode, …), permettent des traitements de plus en plus précis et localisés. Le degré de précision pour un traitement focal de la tumeur est maintenant atteint. Un nouveau protocole de guidage de la thérapie doit donc être envisagé. Ce nouveau protocole est complètement lié aux techniques d'imagerie qui permettent d'acquérir l'information nécessaire. Dans notre cas, deux types d'imagerie seront utilisés :

- L'imagerie ultrasonore. C'est la technique utilisée actuellement lors de l'intervention pour définir le planning et pour piloter la thérapie (Figure 3-droite). Une sonde d'imagerie (ou une partie dual mode de la sonde de thérapie) permet une acquisition du volume de la prostate par voie endorectale. Par contre, les différentes zones de la prostate et la tumeur elle-même ne sont pas (ou peu) discernables sur les images. L'information est généralement donnée par une distribution de speckle. Le contraste entre la prostate et les tissus environnants n'est généralement pas suffisant pour distinguer automatiquement les contours de la prostate. En outre, sur l'image per-opératoire l'échographie est affectée par l'ombre de la sonde urinaire et du ballon qui sont utilisés en thérapie pour protéger l'urètre et la vessie.
- L'imagerie IRM. D'un point de vue clinique, nous avons choisi l'IRM T2 pour la planification pré-opératoire en raison sa bonne résolution et de sa capacité à pouvoir localiser la lésion sur la prostate (Figure 3-gauche). En effet, sur cette séquence, les différentes zones de la prostate sont généralement bien séparables et la tumeur peut apparaître hypointense dans la zone périphérique qui est normalement hyperintense, ou peut apparaître comme homogène et de faible intensité dans la zone de transition qui est normalement hétérogène. L'expert peut alors y localiser et délimiter la tumeur, soit manuellement, soit aidé par des outils de traitements d'images.
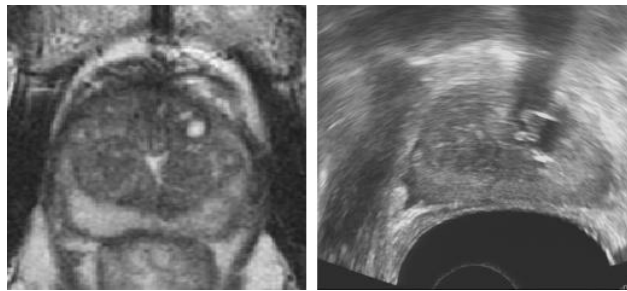
Figure 3 : IRM T2 et image échographique du même patient.

L'idée générale de la Thèse est alors de définir la zone de la tumeur dans un volume IRM T2 pré-opératoire et de reporter cette information dans le volume échographique per-opératoire afin de guider la thérapie. Ceci nécessite une opération de fusion, de recalage des données et de l'information en IRM T2 sur les données échographiques.
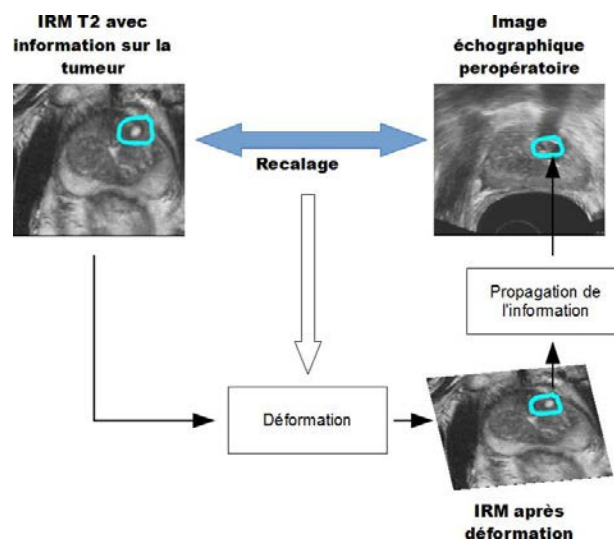
Figure 4 : Cadre général de l'étude. Fusion IRM T2 vers image échographique.

Le cadre générale de la Thèse est résumé dans la Figure 4.
- En images d'entrée, nous avons un volume acquis en IRM T2 et un volume obtenu par une échographie transrectale. Sur le volume IRM T2, nous supposons connaître l'information sur la tumeur obtenue, soit de manière interactive par un urologue, soit de manière automatique par une procédure de traitement d'images[2].
- Dans un premier temps, nous effectuons un recalage élastique 3D entre le volume IRM T2 et le volume ultrasonore. Ce recalage nous permet de définir

---

2   La localisation de la tumeur est hors du cadre de la Thèse.

une transformation élastique entre les deux volumes.

- Nous appliquons alors la déformation ainsi estimée pour déformer le volume IRM T2 vers le référentiel de l'échographie.
- L'information de la tumeur, après déformation est propagée vers le volume échographique.
- Le planning et le guidage de la thérapie peuvent alors être ciblés sur la tumeur dans le volume échographique

La procédure de recalage entre le volume IRM T2 et un volume échographique est le point clé de cette étude. Les méthodes de recalage peuvent être classées en fonction de l'information commune utilisée pour fusionner les volumes. Classiquement, deux types d'information sont utilisés pour le recalage :

- Des statistiques sur la distribution des intensités ou valeurs des voxels des deux volumes. Cette classe de méthodes utilise l'ensemble de l'information contenue dans le volume. De ce fait, elle est réputée être assez robuste. Elle sous-entend toutefois que les intensités sont une mesure caractéristique des objets à recaler.
- Des éléments géométriques (surface, courbes, points) extraits des volumes et permettant de caractériser les objets à recaler. Cette classe de méthodes est directement axée sur les propriétés spatiales des objets à recaler. Toutefois, elle est aussi liée aux procédures d'extraction des éléments géométriques et à leurs degrés de précision.

Le choix entre ces deux classes d'approche est généralement guidé par le contenu des images à recaler.

Dans le cadre de la Thèse nous avons choisi dans un premier temps d'explorer une **méthode basée sur l'intensité**. Le problème est que les différents organes dans l'image ultrasonore sont définis par une distribution spatiale de speckle (une texture) et non par une distribution spatiale d'intensités. Nous nous proposons d'utiliser un descripteur de texture qui pourra être intégré dans la mesure de similarité de la méthode de recalage. En dehors de la distribution spatiale caractéristique des organes, le speckle subit une disposition spatiale liée à l'imageur (disposition en arc de cercle et taille de speckle variant en fonction de la distance à la sonde. Nos travaux nous ont donc amenés à étudier un **descripteur de texture basé sur des moments invariants en rotation et en échelle**. Si ce descripteur donne des résultats intéressants sur l'image échographique, l'hétérogénéité de l'IRM T2 ne nous a pas permis de finaliser la méthode de recalage basée sur l'intensité.

Comme solution de repli, nous avons décidé de rechercher une solution de **recalage basée sur la surface de la prostate**. Cette solution impose d'extraire (de segmenter) la surface de la prostate dans les deux modalités. Une Thèse précédente a proposé de segmenter la surface de la prostate dans les images échographiques à l'aide de contours actifs ou de Définition Optimale de la Surface (OSD) (Garnier, Bellanger et al. 2011). En nous basant sur les conclusions de cette Thèse, nous avons choisi d'adapter **la méthode OSD à la segmentation de la prostate en IRM T2**. Cette méthode a été affinée en proposant une segmentation concurrente de la prostate, de la vessie et du rectum par **OSD multi-objets**. Les surfaces de la prostate extraites du volume échographique et du volume IRM T2, nous ont permis d'envisager une **première tentative de recalage surface/surface** par la méthode des démons.

Partie II : Caractérisation de régions en imagerie échographique

Chapitre 3 : Description de la texture de l'image échographique par moments invariants.

L'objectif de cette étude est de proposer un descripteur de la texture du speckle de l'image ultrasonore. Du fait de la géométrie de la sonde échographique transrectale, le speckle a une disposition spatiale assez particulière (voir Figure 3-droite) : disposition et orientation du speckle en arc de cercle et augmentation de la taille en fonction de la distance à la sonde. Cette variation en orientation et en taille est généralement gênante pour les méthodes de description de texture. Il existe plusieurs classes de descripteurs plus ou moins sensibles aux variations de taille et d'orientation de la texture. Les moments orthogonaux complexes peuvent être utilisés en tant que descripteur et le module de ces moments possède a priori l'avantage d'être invariant à la rotation. Par contre, le module ne génère pas un ensemble d'invariants. En outre, les moments orthogonaux ne sont pas invariants en échelle. Plus récemment, des approches ont été proposées afin d'obtenir un ensemble complet de moments invariants par rapport à la rotation et l'échelle (Chen, Shu et al. 2011) (Zhang, Dong et al. 2010) (Zhang, Shu et al. 2010). Ces moments sont utilisés actuellement pour la reconnaissance de formes.

Dans le cadre de cette Thèse, nous nous proposons d'utiliser 3 types de moments orthogonaux invariants pour décrire la texture du speckle. Les 3 types sont : les moments invariants de Zernike -$ZMI_{p,q}$-, les moments invariants de Pseudo-Zernike -$PZMI_{p,q}$- et les moments invariants orthogonaux de Fourier-Mellin -$OFMMI_{p,q}$-. Dans les 3 cas p indique l'ordre et q la répétition.

Dans un premier temps, l'invariance en rotation et échelle de ces moments par rapport à la version classique a été évaluée sur des images de texture de Brodatz ayant subi des rotations et des changements d'échelle, dans différentes zones d'images échographiques simulées (Figure 5-a) et d'échographies transrectales réelles (Figure 5-b). Dans tous les cas, les moments invariants se sont avérés beaucoup plus stables que les moments classiques par rapport aux transformations géométriques. Contrairement aux moments classiques, les moments invariants ont permis d'obtenir une information relativement homogène dans les zones partageant une même distribution de texture (Figure 6). Les moments invariants peuvent donc servir

d'indicateur de zone de même distribution de speckle et peuvent donc servir dans une mesure de similarité basée intensités. Par contre la différence entre les trois types de moments invariants est marginale.
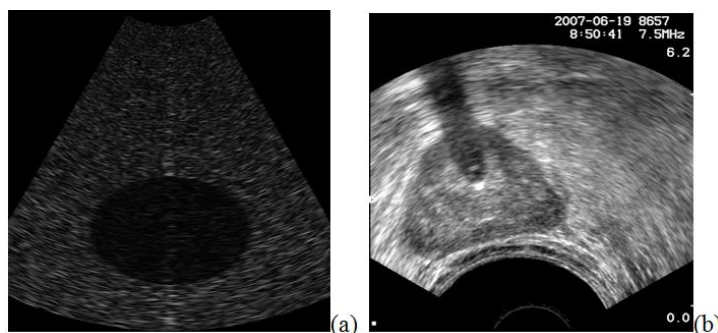
Figure 5 : a) Image échographique simulée ; b) Échographie transrectale réelle.
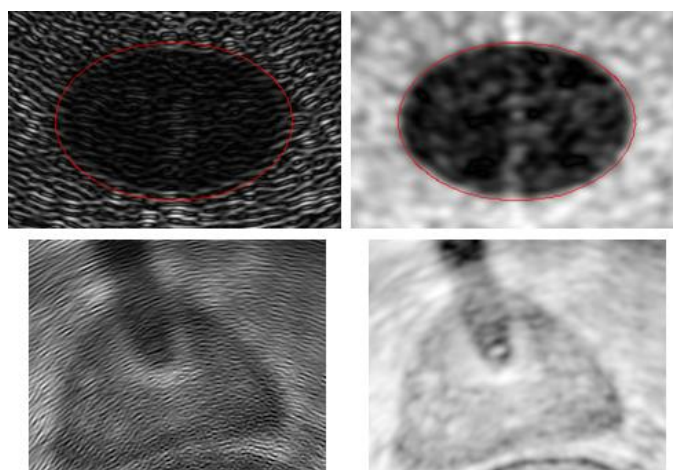
Figure 6 : Comparaison entre moments classiques (col. de gauche) et moments invariants (col de droite) sur l'image échographique simulée et sur l'échographie transrectale réelle.

Dans un second temps, nous avons évalué l'influence de l'ordre p et de la répétition q des moments invariants sur le pouvoir de description de la texture. Si l'ordre p n'a que peu d'influence sur les moments mesurés, la variation de la répétition q a mis en avant des propriétés intéressantes pour notre projet et ceci pour les 3 types de moments invariants : pour $q=0$, les moments sont sensibles à la distribution régionale de l'information de texture (Figure 7-gauche) ; pour $q=1$, les moments sont sensibles à la rupture entre deux textures (Figure 7-centre) et peuvent être assimilés à un "gradient de texture" et pour $q=2$, les moments peuvent être assimilés à un "Laplacien de texture" (Figure 7- droite). Cette caractéristique se retrouve également sur les vraies images échographiques.
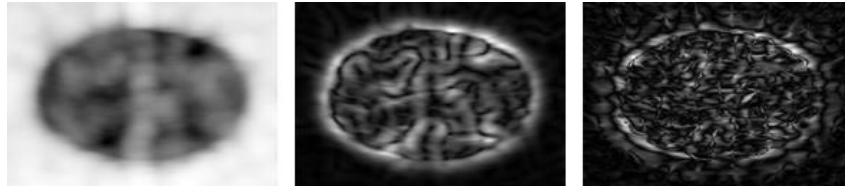
Figure 7 : Images de moments appliqués sur l'échographie simulée. Exemple de l'impact de la variation de la répétition sur les moments invariants de Zernike d'ordre 2 : $q=0$ (gauche), $q=1$ (centre) et $q=2$ (droite)

Cette propriété inattendue, nous ouvre de nouvelles perspectives d'utilisation de descripteurs de texture à l'aide de moments invariants. Dans l'analyse classique d'images par la texture, un ensemble de mesures de texture (statistiques d'ordre 1 ou 2, dimension fractale, moments à différents ordres ou répétitions,..) sont généralement mesurés sur l'image et un procédé de classification est alors effectué afin de caractériser les objets d'intérêt.

Dans notre cas, les moments invariants de répétition $q = 0$ fournissent des informations de région de texture similaire et ceux avec $q = 1$ fournir des informations sur les contours d'une région texturée. L'idée est alors d'utiliser ces deux types complémentaires d'information. De nombreuses techniques de segmentation d'images utilisent l'information de contours, seule ou en combinaison avec l'information sur les régions. C'est le cas par exemple des contours actifs, de modèles déformables, des level sets, etc. Nous pensons que les moments invariants pourraient fournir ce type d'information pour les images échographiques et donc permettraient l'utilisation de ces outils classiques de traitement d'images.

Afin de démontrer cette proposition, nous avons intégré les deux types d'informations (région et contours) donnés par les moments invariants dans une procédure de segmentation par coupe de graphe min-cut/max-flow (min-cut/max-flow graph cut). Dans cette approche, la segmentation agit par minimisation d'une énergie : $E_T = E_{classif} + \lambda\, E_{continuité}$. Dans notre cas, $E_{classif}$ l'énergie liée à l'attache aux données est codée dans le graphe en utilisant un moment de répétition $q=0$ et $E_{continuité}$ l'énergie de régularisation liée au voisinage par un moment de répétition $q=1$ (Figure 8). λ contrôle la part de l'énergie liée aux contours.

X
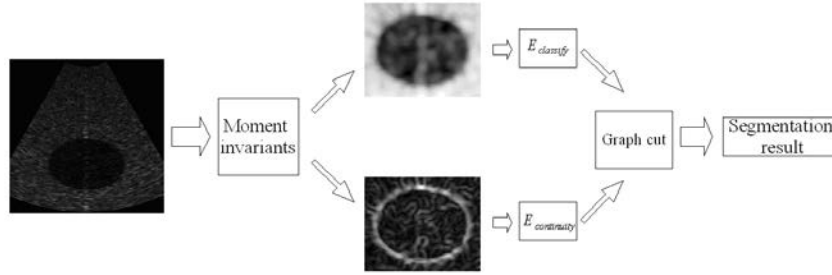
Figure 8 : Données utilisées par l'algorithme graph cut.

Cet algorithme a été appliqué sur les données échographiques de simulation et sur les données réelles. L'influence de l'information de contours permet d'améliorer sensiblement la segmentation (Figure 9).
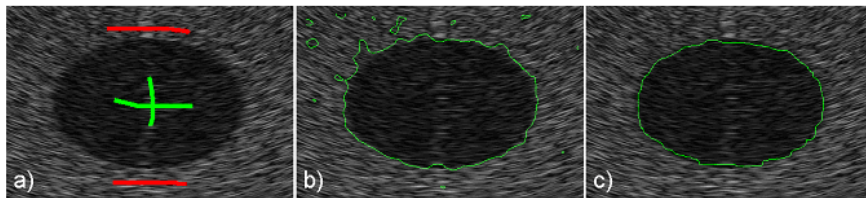
Figure 9 : Segmentation par graph cut. a) points permettant l'apprentissage des classes « objet » (vert) et « fond » (rouge) ; b) résultat de la segmentation avec la seule information de région ($\lambda=0$) ; c) résultat de la segmentation avec l'intégration de l'information de contour de texture ($\lambda=1$).

En conclusion. Nous avons démontré que les moments invariants sont un bon indicateur de zones partageant une même distribution de speckle, ceci quelles que soient l'orientation ou l'échelle de ce speckle. Les moments invariants peuvent donc servir dans une mesure de similarité basée intensités. Nous avons également démontré que si les moments invariants de répétition $q=0$ sont un indicateur de régions de speckle de même distribution, les moments invariants de répétition $q=1$ sont eux sensibles aux ruptures entre régions et fournissent donc une indication sur les contours des objets texturés. Cette caractéristique nous semble très utile pour les méthodes de segmentation intégrant à la fois l'information de contours et l'information de régions (contour actifs, graph cut, etc.).

Concernant maintenant le schéma de recalage basé intensités, les moments invariants appliqués sur l'image échographique peuvent être intégrés directement dans la mesure de similarité (information mutuelle, …). Par contre, l'hétérogénéité des images IRM T2 ne nous a pas permis de finaliser le recalage US/IRM T2.Une approche surface/surface doit alors être envisagée.

Partie III : Éléments d'un recalage basé surfaces

Chapitre 4 : Segmentation de la surface de la prostate en IRM T2 par la Détection Optimale de la Surface (OSD).

Le recalage surface/surface nécessite une description de la surface de l'objet à recaler dans les deux modalités. L'extraction de la surface prostate dans le volume échographique a fait l'objet d'une Thèse précédente (Garnier, Bellanger et al. 2011). Deux méthodes, l'une de contours actifs et l'autre par Détection Optimale de la Surface (OSD) ont été explorées avec un léger avantage pour la seconde méthode en termes de précision et de robustesse. L'idée est alors d'extraire la surface de la prostate dans le volume IRM T2 par cette même méthode. La segmentation de la surface de la prostate en IRM T2 est relativement difficile. Dans cette modalité, la prostate est divisée en une zone périphérique en hypersignal, une zone centrale hétérogène et un stroma antérieur fibromusculaire. Elle est entourée par une bande fibromusculaire, appelée capsule, qui présente un hyposignal difficile à séparer d'organes environnants proches telle la paroi de la vessie. Le volume de la prostate est décrit sur une dizaine de coupes relativement épaisses rendant la surface difficile à discriminer sur les coupes extrêmes du côté de la base ou de l'apex. Or ces zones, par exemple l'apex proche des sphincters, sont très sensibles lors de la thérapie.

L'idée principale de l'OSD est de rechercher la surface au voisinage d'une première approximation par une méthode de graph cut (Li, Wu et al. 2004). Le schéma général de la segmentation est le suivant :

- Une première étape d'initialisation donnant une première approximation de la surface. Cette étape peut être automatique. Par contre, afin de pallier la difficulté de définir la surface au niveau de la base et l'apex, nous avons décidé d'utiliser une initialisation interactive par un expert. Il définit 6 points : base, apex et 4 points dans la coupe centrale. Une surface paramétrique par spline biharmonique ajustée sur ces points sert alors de première approximation.

- Un graphe est construit à partir de l'information au voisinage de cette surface. Les nœuds du graphe sont formés par les voxels se trouvant de part et d'autre de la surface de départ le long de la normale. Certains liens entre nœuds permettent de coder la probabilité qu'un nœud appartient à la surface. La topologie de certains autres liens entre nœuds permet d'imposer des contraintes de lissage de la future surface. Nous avons testé 3 méthodes différentes pour assigner la probabilité qu'un nœud appartient à la surface :

- une méthode basée sur les gradients des intensités des voxels ;
- une méthode basée sur un modèle de probabilité de surface. Ce modèle a été construit à partir de surfaces délinéées par un expert sur 33 différents volumes IRM T2 et alignées les unes par rapport aux autres. Cet alignement permet de définir une surface moyenne et une carte de distribution des surfaces par rapport à la surface moyenne.
- Une méthode basée sur un modèle de profil de gradients autour de la surface. Ce modèle est également construit à partir des surfaces délinéées par un expert sur les 33 volumes et alignés les une par rapport aux autres. En chaque point de ces surfaces, le profil des gradients est mesuré le long de la normale à la surface. Un modèle de profil de gradient est alors estimé à partir des 33 différents profils. Pour une surface inconnue, une mesure de distance de Mahalanobis entre le profil de la surface inconnue et le modèle de profils permet d'estimer une probabilité de surface.
  - Une coupe de graphe permet alors de déterminer la surface optimale.

Afin de mettre au point les paramètres de cette technique et d'évaluer la précision des 3 méthodes d'assignation de probabilité, nous avons utilisé une base de données de 33 volumes IRM T2 cliniques de la prostate provenant de 5 machines différentes, avec des résolutions et des épaisseurs de coupes différentes. Un urologue a contouré la prostate dans toutes les coupes de tous les volumes. Ce contourage manuel a servi de « vérité terrain » pour évaluer la performance de notre segmentation (à l'aide de mesure comme le taux de recouvrement de volumes ou de Dice Score) mais également pour fabriquer les modèles de probabilité de surface ou de profil de gradients.

Dans un premier temps, nous avons ajusté les paramètres un par un, le jeu de paramètre donnant le meilleur résultat (la meilleure moyenne de taux de recouvrement de volumes) pour toutes les bases a été gardé

Nous avons ensuite comparé les 3 méthodes pour assigner la probabilité qu'un nœud appartient à la surface. Si pour certains cas précis, les méthodes basées sur des modèles de surface ou de gradient pouvaient donner de meilleurs résultats que les gradients des intensités, globalement leurs scores obtenus par l'utilisation des modèles étaient inférieurs. Ces modèles n'ont pas été retenus par la suite.

En regardant de plus près les résultats de la segmentation, nous avons constaté que la segmentation par OSD décrivait souvent correctement la surface de la prostate dans la zone médiale. Par contre, elle a plus de problèmes vers les extrêmes, base et apex, du fait que dans ces zones, les coupes épaisses sont tangentes à la surface et que dans

ces zones également, la prostate est en contact avec la vessie ou le rectum. En IRM T2, la paroi de la vessie a des intensités similaires à la capsule de la prostate et que le rectum est totalement inhomogène en forme et intensités en fonctions de contenu. Ces particularités rendent très difficile la délimitation de la surface dans ces zones, or certaines de ces zones sont très sensibles lors de la thérapie (par exemple les sphincters urinaires sont au niveau de la base : de même les positions du rectum et de la prostate doivent être bien définies afin d'éviter des fistules lors de la thérapie). Nous proposons donc une segmentation concurrente entre la vessie, la prostate et le rectum par un algorithme d'OSD multi-objets (Song, Liu et al. 2010). L'idée est que la compétition entre ces organes améliore la segmentation de la surface de la prostate. L'OSD multi-objets nécessite une description initiale des trois organes :

- Prostate. La surface initiale de la prostate est donnée par OSD simple comme il a été décrit précédemment (Figure 10-vert).

- Vessie. La forme de la vessie est très diverse en fonction de son remplissage. En IRM T2, l'urine apparaît en hypersignal mais la paroi est en hyposignal. La description initiale de la vessie sera donc donnée par sa paroi interne recherchée par une surface déformable (Garnier, Ke et al. 2011). Pour cela à partir de la position de la prostate, nous cherchons automatiquement un point germe dans la zone urinaire (recherche d'hypersignal au-dessus de la base de la prostate). À partir de ce point germe, une petite surface ellipsoïdale est définie. Cette surface est mise en expansion jusqu'à ce que les forces d'expansion s'équilibrent avec des forces liées aux données et indiquant la transition urine/vessie (Figure 10-rouge).

- Rectum. Du fait de sa variabilité en forme et intensité, nous avons choisi d'ajuster un modèle géométrique simple de cylindre brisé sur le rectum à partir de 4 points définis de manière interactive (Figure 10-jaune).
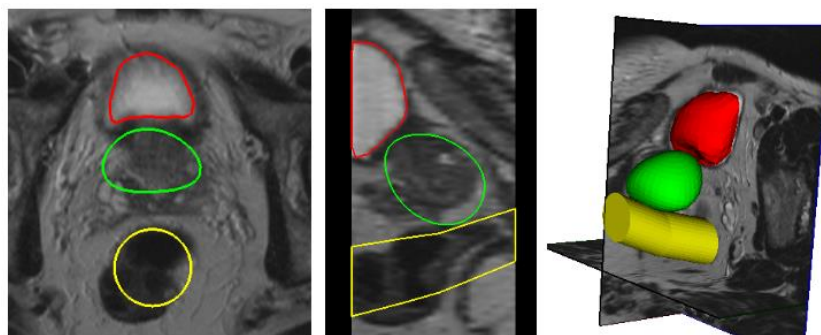

Figure 10 : Description initiale de la vessie (rouge), de la prostate (vert) et du rectum (jaune).

Au final seulement 10 points (6 pour la prostate et 4 pour le rectum) définis de manière interactive sont nécessaires pour initialiser les 3 surfaces. Nous constatons

que dans certaines zones, les maillages initiaux s'interpénètrent ou sont très proches les uns des autres. Ces zones seront appelées zone de conflit. Pour chaque organe nous construisons alors un graphe de la manière décrite pour l'OSD simple. Toutefois, dans les zones de conflit nous rééchantillonnons la position spatiale des nœuds pour que les deux graphes y partagent les mêmes nœuds. En plus des liens décrits utilisés dans l'OSD simple, nous ajoutons de nouveaux liens dans les zones de conflits empêchant deux surfaces à s'interpénétrer. De même, modifions également certaines probabilités d'appartenance afin de prendre en compte certains paramètres anatomiques des organes, par exemple le fait que la paroi de la vessie à une épaisseur de l'ordre de 3 à 5 mm.

L'algorithme du graph cut appliqué sur les trois graphes permet alors de définir respectivement la surface des 3 organes (Figure 11-droite).

Nous avons également utilisé la base de 33 volumes annotés pour ajuster les différents paramètres de la méthode de segmentation.

Par contre, par souci de comparaison, nous avons décidé d'évaluer la performance de notre algorithme de segmentation sur les données fournies par un challenge MICCAI en 2012 sur la segmentation de la prostate en IRM T2 (Challenge PROMISE (MICCAI 2012))[3]). Nous avons comparé les performances de l'OSD simple, de l'OSD multi-objets prostate/vessie et de l'OSD multi-objets prostate/vessie/rectum. L'OSD multi-objets prostate/vessie/rectum donnait les meilleurs résultats. De plus, les performances de nos méthodes étaient du même niveau que la meilleure méthode présentée en 2012 lors du Challenge (Vincent, Guillard et al. 2012).

D'un point de vue qualitatif, nous avons constaté que l'OSD multi-objets empêchait l'extension de la surface de la prostate vers la vessie (Figure 11-gauche) et vers le rectum (Figure 11-centre).

---

3   Nous n'avons en fait utilisé que les 11 volumes des données d'entraînement acquises à l'aide d'une antenne externe. Nous n'avons pas utilisé les volumes acquis à l'aide d'une antenne endorectale car la correction des inhomogénéités d'intensités dûes à ces antennes était hors des propos de cette Thèse.
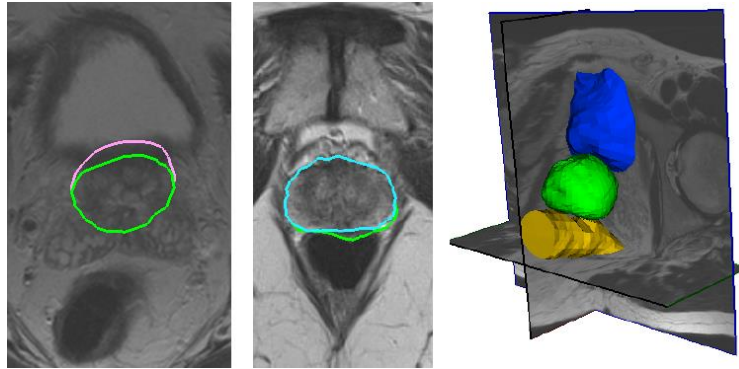
Figure 11 : Comparaison entre la surface de la prostate : à gauche, au niveau de la vessie par OSD simple (mauve) et OSD multi-objets (vert) ; au milieu au niveau du rectum par OSD simple (vert) et OSD multi-objets (bleu clair). À droite, surfaces segmentées des 3 organes : vessie (bleu), prostate (vert) et rectum (orange)

Chapitre 5 : Étude préliminaire d'un recalage surface/surface échographie/IRM T2

Nous disposons de la surface de la prostate dans les deux modalités : extrait du volume échographique grâce à l'OSD (Garnier, Bellanger et al. 2011) et du volume IRM T2 grâce à l'OSD multi-objets. Entre les deux acquisitions, la prostate a subi un déplacement et une déformation, entre autres dûs à la présence de la sonde de thérapie. Un recalage élastique doit donc être envisagé. Il s'effectue en deux étapes :

- un premier recalage rigide pour aligner les deux surfaces. Pour cela nous avons choisi d'utiliser l'algorithme itératif du plus proche voisin (ICP) (Besl and McKay 1992) entre les nœuds des maillages des deux surfaces (Figure 12). La matrice de transformations estimée entre les deux surfaces servira d'initialisation au recalage élastique proprement dit.

Figure 12 : Recalage rigide entre la surface de la prostate en échographie (gauche) et en IRM T2 (centre).

- Un recalage élastique. Nous avons choisi d'utiliser l'algorithme rapide des démons à forces symétriques (Thirion 1998, Vercauteren, Pennec et al. 2009).

Pour cela deux volumes binaires sont construits par remplissage des surfaces des deux organes. Le volume lié à l'échographie est considéré comme image fixe. L'algorithme des démons[4] est utilisé dans un schéma de multi-résolution pour estimer le champ de déformations entre les deux organes. Ce champ est ensuite utilisé pour reporter l'information de l'IRM T2 préopératoire vers le volume échographique peropératoire (Figure 13).
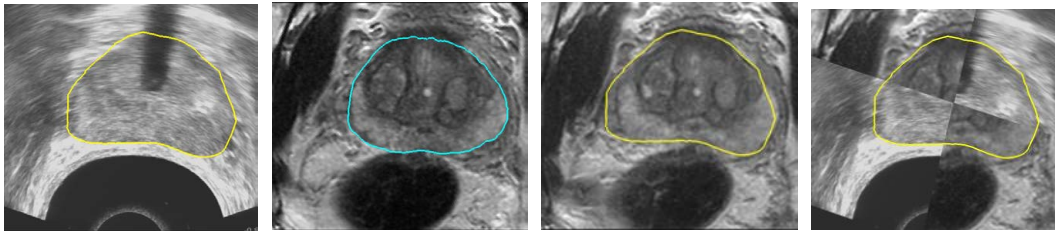
Figure 13 : Étapes du recalage entre le volume IRM T2 préopératoire et le volume échographique peropératoire. De gauche à droite : coupe du volume échographique peropératoire ; recalage rigide ; puis recalage élastique du volume IRM T2 vers l'échographique peropératoire ; superposition des deux informations

Ce schéma a été essayé sur dix paires de volumes de patients traités par l'Ablatherm afin de montrer la faisabilité de l'approche. Une étape de validation, entre autre de la pertinence de la déformation des structures internes de la prostate en IRM T2, en particulier de la tumeur, doit maintenant être menée.

---

4   La classe itkFastSymmetricForcesDemons -RegistrationFilter de la librairie ITK.

Conclusion

Cette Thèse a essayé de proposer, dans le cadre d'un traitement focal de la tumeur de la prostate par HIFU, des méthodes permettant de reporter l'information préopératoire de l'anatomie de la prostate et de la position de la tumeur sur l'image échographique peropératoire. Deux approches ont été explorées :

- Un schéma de recalage basé sur les intensités. Notre contribution a été de proposer une méthode de description de la texture de speckle de l'image échographique par des moments invariants pouvant servir dans les mesures de similarités entre volumes. Du fait de l'inhomogénéité des intensités dans la prostate en IRM T2, nous n'avons pas pu valider l'utilisation de cette méthode de description dans le schéma de recalage basé intensités. Toutefois, cette méthode a montré sa performance à décrire des régions en échographie présentant des distributions similaires de speckle, quelles que soient leurs orientations ou tailles. De plus, certains moments sont sensibles aux contours d'une région texturée. Cette information complémentaire région/contour peut être utilisée dans des algorithmes de segmentation intégrant à la fois l'information de contours et l'information de régions (contours actifs, graph cut, etc.). Nous avons démontré cette possibilité dans un algorithme de segmentation 2D de la prostate en échographie par min-cut/max-flow graph cut.

- Un schéma de recalage basé sur la surface de la prostate. Un travail de thèse précédent à permis d'estimer la surface de la prostate en échographie 3D par contours actifs ou par Détection Optimale de la Surface (OSD. Notre contribution dans le schéma de recalage a consisté à adapter l'algorithme OSD à la segmentation de la surface en IRM T2 et à améliorer cette segmentation dans les zones sensibles (aux voisinages de la vessie ou du rectum) par un OSD multi-objets. Cette méthode a permis d'extraire la surface de la prostate avec une bonne précision, comparativement à d'autres méthodes. À partir des surfaces extraites dans les volumes IRM T2 préopératoire et échographique peropératoire nous avons pu utiliser une méthode de recalage élastique et de fusion d'information entre ces deux volumes. Cette méthode doit être maintenant évaluée dans un cadre clinique.

Références des papiers liés aux travaux de Thèse

Articles publiés dans des journaux

Garnier, C., Bellanger, J.-J., Wu, K., Shu, HZ., Costet, N., Mathieu, R., de Crevoisier, R. and Coatrieux, J.-L. "Prostate Segmentation in HIFU Therapy," *IEEE transactions on Medical Imaging,* (30:3), 2011, pp. 792-803.

Mari, J.-M., Bouchoux, G., Dillenseger, J.-L., Gimonet, S., Birer, A., Garnier, C., Brasset, L., Wu, K., Guey, J.-L., Fleury, G., Chapelon, J.-Y. and Blanc, E. "Study of a dual-mode array integrated in a multi-element transducer for imaging and therapy of prostate cancer," *IRBM* (34:2), 2013, pp. 147-148.

Wu, K., Garnier, C. and Dillenseger, J.-L. "Prostate segmentation on T2 MRI using Optimal Surface Detection," *IRBM* (34:4-5), 2013, pp. 287-290.

Wu, K., Shu, H. and Dillenseger, J.-L. "Region and boundary feature estimation on ultrasound images using moment invariants," *Computers Methods and Programs in Biomedicine* (in press), DOI:10.1016/j.cmpb.2013.10.016, 2014.

Articles publiés dans des conférences avec comité de lecture

Wu, K., Garnier, C., Coatrieux, J.-L. and Shu, H. Z. "A Preliminary Study of Moment-based Texture Analysis for Medical Images", 32th conf. of the IEEE Engineering in Medicine and Biology Society, Buenos Aires, 2010, pp. 5581-5584.

Garnier, C., Wu, K. and Dillenseger, J.-L. "Bladder segmentation in MRI images using active region growing model", 33rd conf. of the IEEE Engineering in Medicine and Biology Society, Boston, 2011, pp. 5702-5705.

Wu, K., Garnier, C. and Dillenseger, J.-L. "Prostate segmentation on T2 MRI using Optimal Surface Detection", RITS 2013, Bordeaux, 2013, 3 pages.

3D Segmentation and Registration for Minimal Invasive Prostate Cancer Therapy

Content

Introduction

Prostate cancer is the second most frequently diagnosed cancer in the world, and also the sixth leading cause of cancer death in males. Many types of treatment, including active surveillance, surgery, radiation therapy, high-intensity focused ultrasound (HIFU), chemotherapy, cryosurgery, hormonal therapy, and sometimes combination of treatments, are used in prostate cancer therapy.

High intensity focused ultrasound (HIFU) technology, which focus ultrasound waves to prostate to locally heat and destroy the target tissue, has been shown to be effective in prostate cancer treatment. In the past few years, HIFU therapy has taken benefit from the development of new technological advances, such as new probe design, new therapeutical planning, imaging guided techniques, which lead to more precise spatial treatment. The current trend in medicine is to perform focal therapy by only treating the tumor area within the organ. So, in the near future, the new HIFU device must be able to locate the tumor area within the prostate and then to focus the ultrasound waves to this specific area.

Our Thesis is part of the ANR TecSan MULTIP project (Matrice de transducteurs Ultrasonores pour La Thérapie et l'Imagerie de la Prostate) which aimed at using up-to-date piezoelectric technologies to design dual-mode ultrasonic probes for cancer-foci treatment and monitoring and also to propose image processing methods permitting the design of the ultrasonic imaging/therapy process. The general goal of the thesis is to propose **image processing techniques for the planning and the guidance of HIFU focal prostate cancer therapy**.

Currently the therapy planning and guidance of the HIFU prostate therapy is performed on a transrectal ultrasound (TRUS) volume acquired by the HIFU device probe. If the quality and resolution of the TRUS images are sufficient enough to allow a therapy planning for the entire prostate, the tumor itself cannot be discriminated within the prostate. On the other hand, we can get high quality information about the prostate anatomy and the prostate tumor on a preoperative T2 MRI. A transfer of this information extracted during the preoperative planning onto the peroperative ultrasound image should allow retrieving the tumor location during the therapy. This transfer requires a phase of **registration or fusion between the 3D MRI volume and the ultrasound images**. Beside other considerations, several registration strategies can be considered according to the common information used for the merging. Two strategies of registration methods will be explored in this Thesis: the intensity-based registration and the feature-based registration.

In intensity-based registration, the main hypothesis is that a tissue is described by

a specific intensity distribution. But in ultrasound images, tissues are characterized by their speckle spatial distribution instead of an intensity distribution. The main idea is to use a texture description method which is able to transpose a specific speckle distribution into a characteristic value distribution. Texture estimation tools had some success in ultrasound image analysis. But, in our case, the circular US probe provides an irregular spatial speckle organization in orientation and scale over the image. A **texture analysis tool invariant to speckle orientation and scale** must be considered to characterize the tissues in the US image.

In feature-based registration, common features (points, lines, surfaces...) are extracted or labeled in both image modalities and are used for the registration. In our specific case, TRUS image and T2 MRI of the prostate share only little common information. However, the prostate surface is visible in both image modalities. A registration framework can so be defined: A) the extraction of the prostate surface on the preoperative T2-MRI volume by segmentation; B) the extraction of the prostate surface on the peroperative TRUS volume by segmentation; C) elastic registration between the 2 surfaces; and D) the deformation field estimated by the registration step is applied to fuse the T2 MRI volume information (prostate structures and tumor) to the peroperative HIFU TRUS volume. The bottlenecks of this framework are the prostate surface segmentation methods. For TRUS images, we will use the work done at our lab by Carole Garnier which proposed active contours or Optimal Surface Detection (OSD) for the extraction of the prostatic surface in 3D ultrasound (Garnier, Bellanger et al. 2011). The segmentation of the prostate surface in T2 MR image is more problematic. The intensity distribution inside the prostate is really inhomogeneous due to its complex structures and the prostate surface itself has a hyposignal with similar level intensities as these of neighbor organs tissues as the bladder wall or the rectum. A **T2 MRI segmentation method** dealing with these difficulties must be developed in order to extract the prostate surface alone or in a **multi-objects competition scheme**. The next issue is then to perform an **elastic registration scheme** which can not only align together the two surfaces but also can estimate a 3D deformation field between the preoperative and the peroperative volumes.

These several questions will give the structure of the Thesis. It is composed by 3 main parts:

Part I gives the context of the study and justifies the several approaches proposed in the Thesis. In chapter 1, we introduce the medical application background of the Thesis: the prostate cancer and its treatment. This part will show the importance of the problem we are dealing with. Chapter 2 is focused on our specific problem. We first describe the actual principle and workflow of the HIFU treatment. The importance of

the registration problem in image guide therapies will be highlighted. After a brief description of the image properties of the preoperative T2 MRI and the peroperative TRUS and also of the characteristic of registration and segmentation methods, we will justify the choice of the proposed methods used for the intensity-based registration and the feature-based registration.

Part II presents our contribution in intensity-based registration methods. In chapter 3, a moment invariants based texture descriptor is introduced to convert speckle distribution of the ultrasound image to intensity distribution. This work should be a preparation of an intensity-based registration, but we did not fulfill it because of its disadvantage on T2 MRI.

Part III presents our contribution in surface-based registration methods. In chapter 4, we introduce an OSD based multi-objects segmentation method on T2 MRI. The segmented surfaces will be used as prostate feature in the registration process. In chapter 5, we apply the surface based registration on MRI/TRUS volumes. We give some preliminary results from 10 cases of MRI/TRUS data, and make a discussion.

Finally in chapter 6, we conclude the work and contribution of this thesis, and give the possible future works.

Part I:

Image Guided HIFU Therapy for Prostate Cancer
General Framework of the Thesis

Chapter 1: Prostate cancer treatment

1.1 Prostate cancer

Prostate cancer is the second most frequently diagnosed cancer in the world accounting for 14% (903,500) of the total new cancer cases in 2008. It is also the sixth leading cause of cancer death in males. In 2008, about 258,400 males died because of prostate cancer, which is the 6% of the total cancer deaths (Jemal, Bray et al. 2011).

In recent years, the incidence rates of prostate cancer vary by more than 25-fold worldwide. It is the highest rates recorded primarily in the developed countries of Oceania, Europe, and North America. It is in part because of the wide utilization of prostate specific antigen (PSA) testing which detects clinically important tumors in prostate.

The incidence rates in countries with higher uptake of PSA testing such as the United States, Australia, Canada, and the Nordic countries rose rapidly in the early 1990s, soon after the introduction of PSA testing, then followed by a sharp decline due to a smaller pool of prevalent cases (Kvåle, Auvinen et al. 2007, Baade, Youlden et al. 2009). In other high-income countries with a low and gradual increase in the prevalence of PSA testing, such as Japan and the United Kingdom, rates continue to increase slightly (Baade, Youlden et al. 2009).

In many developed countries, death rates for prostate cancer have been decreasing, including Australia, Canada, the United Kingdom, the United States, Italy, and Norway in part because of the improved treatment with curative intent. In contrast to the trends in Western countries, incidence and mortality rates are rising in Central and Eastern European and several Asian countries, such as Japan (Baade, Youlden et al. 2009, Bray, Lortet-Tieulent et al. 2010).

About one third of patients diagnosed as prostate cancer have one or more symptom, such as frequent urination, nocturia (increased urination at night), difficulty starting and maintaining a steady stream of urine, hematuria (blood in the urine), and dysuria (painful urination), which are similar to symptom of other prostate diseases such as benign prostatic hyperplasia. It is because the prostate gland surrounds the prostatic urethra. Changes within the gland will directly affect the urinary function (Miller, Hafez et al. 2003).

Prostate cancer may also cause problems with sexual function and performance, such as difficulty achieving erection or painful ejaculation. It is because the vas

deferens deposits seminal fluid into the prostatic urethra, and secretions from the prostate gland itself are included in semen content (Miller, Hafez et al. 2003).

Advanced prostate cancer can spread to other part of body and will cause additional symptoms. When cancer spread into vertebrae (bones of the spine), pelvis, or ribs, it may cause bone pain. Prostate cancer spreading in the spine can also compress the spinal cord, causing leg weakness and urinary and fecal incontinence (van der CRUIJSEN-KOETER, Vis et al. 2005).

There are so many risk factors for prostate cancer, that a complete understanding of these causes remains elusive. Many researchers try to figure out the risk factors associated with prostate cancer, and get some preliminary conclusions:

- Age is one of the primary factors for prostate cancer. Prostate cancers are rarely diagnosed for men younger than 45, but becomes more and more common with growing age. The average age at the time of diagnosis is 70 (Hankey, Feuer et al. 1999). However, in many cases, prostate cancer may never been diagnosed before patient's deadth. Autopsy studies of Chinese, German, Israeli, Jamaican, Swedish, and Ugandan men who died by other causes showed that prostate cancer was found in 30% of men in their fifties, and found in 80% of men in their seventies (Breslow, Chan et al. 1977).

- The genetic background may also contribute to prostate cancer risk. Comparing with men without prostate cancer in the family, men who have first-degree family members with prostate cancer appear to have double risk of getting the disease (Zeegers, Jellema et al. 2003). A study showed that the probability for men with an affected brother is greater than the probability for men with an affected father. In the United States, prostate cancer affects more commonly black men than white or Hispanic men, and caused higher mortality rate for black men (Gallagher and Fleshner 1998, Hoffman, Gilliland et al. 2001). In contrast, the incidence and mortality rates for Hispanic men are one third lower than for non-Hispanic white men. Studies of twins in Northern Europe find that forty percent of prostate cancer risk can be explained by inherited factors (Lichtenstein, Holm et al. 2000).

- The evidence about some dietary factors associate with prostate cancer is still tentative (Venkateswaran and Klotz 2010). For now, some evidence show us that fruits and vegetables play little role in prostate cancer (Key 2010). No evidence can be proved that red or processed meats will increase the prostate

cancer probability (Alexander, Mink et al. 2010). However, higher meat consumption has been associated with a higher risk in some studies. A low vitamin D level or an excessive multivitamins ingestion have been shown to increase the risk of developing the disease (Lawson, Wright et al. 2007, Wigle, Turner et al. 2008).

- Some other factors may also be related to the risk of prostate cancer. E.g. men with high blood pressure are more likely to develop prostate cancer (Martin, Vatten et al. 2010). There is also a small increased risk of prostate cancer associated with the lack of exercise (Friedenreich, Neilson et al. 2010), etc.

1.2 Anatomy of the prostate and pathology

The mean weight of a healthy adult male's prostate is about 11 grams, usually ranging between 7 and 16 grams. It is classically said to be slightly larger than a walnut (Leissner and Tisell 1979). The prostate is located in the pelvis, under the urinary bladder and in front of the rectum (Fig 1.1). It is the only exocrine organ located in the midline of the human bodies. It is close to the rectum and can be felt during a rectal exam. Prostate surrounds the urethra coming from the bladder. This part is called the prostatic urethra and merges with the two ejaculatory ducts. The sphincter urethrea muscle is just appended at the exit of the urethra from the prostate. Prostate is enveloped by a so-called capsule, in reality, an integral fibromuscular band which surrounds the organ (Ayala, Ro et al. 1989). It is bounded by the muscles of the pelvic floor (Raychaudhuri and Cahill 2008). Along the posterior part of the prostate are two collections of vessels and neural structures called neurovascular bundles.
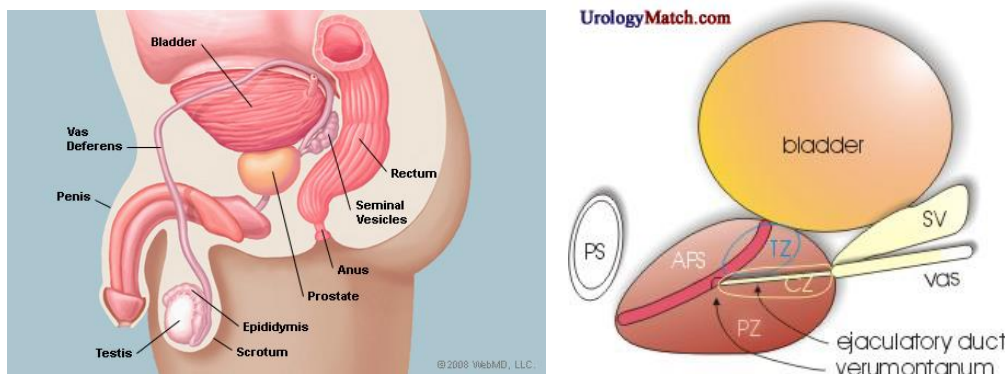
Fig 1.1: The structure of prostate gland and surrounding organs

McNeal models the prostate gland into four distinct glandular regions, defined according to the different segments of the prostatic urethra (McNeal 1968)(Fig 1.1):

- Peripheral zone (PZ): It is the sub-capsular portion of the posterior part of the prostate gland that surrounds the distal urethra. The peripheral zone represents up to 70% of the prostate volume by young men. 70-80% of the prostate cancers originate in the peripheral zone.
- Central zone (CZ): This zone surrounds the ejaculatory ducts. It is approximately 25% of normal gland volume. The central zone accounts for roughly 2.5% of the prostate cancers. But these cancers tend to be more aggressive and have higher risk to invade the seminal vesicles.
- Transition zone (TZ): It is only 5% of the gland volume at puberty. It surrounds the proximal urethra and is the region of the prostate gland that grows throughout life. It is responsible for the disease of benign prostate enlargement. About 10-20% of the prostate cancers originate in this zone.
- Anterior fibro-muscular zone (AFZ): This zone is approximately 5% of the prostate. It is usually devoid of glandular components but composed only of muscle and fibrous tissues.

The main function of the prostate is to secrete and store the seminal fluid. In the prostate, small glands secrete about 20% of the fluid constituting the semen. The prostate surrounds part of the urethra, the tube that carries urine from the bladder during urination and semen during ejaculation (Moore 2013). Because of its position, prostate diseases often affect urination, ejaculation, and rarely defecation.

The prostate accumulates zinc and product citrate. Zinc is transported into prostate cells by the protein ZIP1. It is used to change the metabolism of the cell to produce citrate which is an important component of semen. All these processes (including zinc accumulation, alteration of the metabolism and the citrate production) will need enormous amounts of energy (ATP). Protein ZIP1 is the product of gene SLC39A1 which is called tumor suppressor gene. The absence of zinc is thought to occur via a silencing of gene SLC39A1 and lack of transporter protein ZIP1. When prostate cancer cells are lack of zinc, the citrate production is interrupt. The excess energy will be used to grow and spread cancer cells.

Prostate cancer begins when normal semen-secreting prostate gland cells mutate into cancer cells. The adenocarcinoma region of prostate gland is most common in the peripheral zone. At first, these cancer cells are limited by other normal prostate glands. This is the condition known as carcinoma in situ or prostatic intraepithelial neoplasia (PIN). Although PIN is not a cancer precursor according to the state of research, it is only closely associated with cancer. After this first period, the cancer cells start to

multiply and spread to the surrounding tissues (the stroma), this forming the tumor. The tumor will continuously grow until it is large enough to invade the nearby organs, such as the seminal vesicles, the rectum, the bladder or the lower ureters. In some worse situation, the tumor cells may develop an ability to travel trough the bloodstream or lymphatic system. A mass of cells that can invade other parts of the body when the prostate cancer is consider as a malignant tumor. The invasion of other organs is called metastasis. The organs which are usually affected by prostate cancer metastasis are the bones or the lymph nodes.

1.3 Diagnose

Prostate cancer can be diagnosed during systematic screening or in cases of specific symptoms. Systematic screening is for the moment controversial. So far, research has not yet proved that the potential benefits of testing outweigh the harms of testing and treatment. The American Cancer Society suggests that men should not be tested without learning about what we know and don't know about the risks and possible benefits of testing and treatment. People who is more than 50 years old are recommend to talk to the doctor about the pro and cons of testing before making a decision (Smith, Cokkinides et al. 2002). However, in the western countries people over fifty are screened systematically, mostly using digital rectal examination (DRE) or prostate specific antigen (PSA) tests. If these tests present some prostate cancer suspicions, complementary examinations, like imaging and biopsies will be performed to confirm or infirm the suspicions. These complementary examinations will also have the purpose to diagnose how far the cancer has spread within or outside the prostate. This process is called the staging of the prostate cancer, and will help to evaluate the prognosis and to select the most appropriate therapy. The PSA rate is one of the element of the staging. The result of the biopsy known as Gleason Score is another element. Another element is the four-stage TNM system (Tumor/Nodes/Metastases), which evaluates by DRE and imaging the extent of the primary tumor, the number of involved lymph nodes, and the presence of any other Metastases (Sobin and Fleming 1997). The T stage is important because it allows to separate cancers which are confined within the prostate (stage T1 and T2) to cancer which are spread to neighbor organs (stage T3 and T4). The TNM information combined with the Gleason Score and PSA, helps determining the treatment options and prognosis (Partin, Yoo et al. 1993).

- PSA

Prostate-specific antigen, or PSA, is a protein produced by cells of the prostate gland. If PSA is overexpressed, it is high probability to suspect prostate cancer. The PSA test was approved by the FDA in 1986 to monitor the progression of prostate cancer in men who had already been diagnosed with the disease. In this test, the blood sample is sent to the doctor for analysis, and the results are reported as nanograms of PSA per milliliter (ng/mL) of blood.

A man's PSA level can also rise in a number of benign conditions. Statical data shows that prostatitis (inflammation of the prostate) and benign prostatic hyperplasia (BPH) (enlargement of the prostate) are the most frequent benign prostate conditions that cause an elevation in PSA level. For now, there is no evidence that prostatitis or BPH leads to prostate cancer. It is possible for a man to have one or both of these conditions and to develop prostate cancer as well.

Because of overdiagnosis exists in PSA testing, an overtreatment may be applied to benign and none threatening tumors. Overtreatments for early prostate cancer, as surgery or radiation therapy, can expose the patient unnecessarily to potential complications or harmful side effects. The side effects of these treatments include urinary incontinence (inability to control urine flow), problems with bowel function, erectile dysfunction (loss of erections, or having erections that are inadequate for sexual intercourse), and infection.

There is also possibility to have false-positive or false-negative results in PSA testing. The false-positive test results may create anxiety for a man and his family and lead to additional medical procedures. And false-negative test results may give a man, his family, and his doctor the false assurance that he does not have cancer, when he may in fact have a cancer that requires treatment.

Study shows that it is hard to quantify the role of PSA testing in the reduction of the prostate cancer mortality rates at the population level. A large US-based randomized trial on the efficacy of PSA testing in reducing mortality from prostate cancer found no benefit (Andriole, Crawford et al. 2009), while another similar European-based trial found a modest benefit (Schröder, Hugosson et al. 2009). However, this test is still one of the first diagnosis step in the systematic prostate cancer screening.

- Biopsy

Despite its invasiveness, biopsy is the only test that can fully confirm the diagnosis of prostate cancer. In a biopsy, the doctor will pick small pieces of the prostate for microscopic examination.

Normally, biopsy is only offered when prostate cancer is suspected. During a biopsy, the urologist obtains small tissue samples from the prostate via the rectum. The biopsy gun with special hollow-core needles is inserted and removed in less than a

second. In this process, usually three to six tissues on each side of the prostate are taken away. The prostate biopsy process rarely requires hospitalization. But reports show that more of 50 percent of men feel uncomfortable during prostate biopsy (Essink-Bot, Nijs et al. 1998).

After taking tissue samples, the doctors will exam these samples by using a microscope. They will evaluate the microscopic features and determine whether cancer cells are present or not in tissues. If the cancer is detected, the doctors will grade the tumor by using Gleason Score. Cancers with a higher Gleason Score are more aggressive and have a worse prognosis (Gleason and Mellinger 1974).

- Imaging

The two most main imaging methods used for prostate cancer detection and diagnose are the Ultrasound (US) and Magnetic Resonance Imaging (MRI).

Prostate ultrasound, also called transrectal ultrasonography (TRUS), provides images of a man's prostate gland and surrounding tissues. The transducers are usually composed by a circular 7.5 MHz imaging probe. In the diagnose stage, ultrasound is used to prepare the biopsy in defining the potential prostate areas suspected to be tumors. However, tumor lesions appear with variable echogenicity. On the US images, the lesions are most often hypoechoic but sometimes hyperechoic. In most of the cases, they are difficult to differentiate from the surrounding prostate tissues. Abnormal contours are also difficult to distinguish in the US images. At least, the poor tissue resolution of this imaging modality is a limitation to its usage as diagnostic tool. But because it is wide spread and it has real-time facility, this modality is widely used in an image guide therapy context.

MRI is for the moment the only imaging device which has enough spatial resolution and tissue discrimination possibilities to locate and characterize prostate cancer. The prostate can be examined by several MRI sequences which constitute the multi-parametric prostate MRI (Gupta, Kauffman et al. 2013) (Fig 1.2):

- T2 weighted imaging usually has a high resolution in the images but with a slice thickness of around 3-4 mm. It provides the best assessment of the prostate's morphology, margins, and internal structures. It allows to make the distinction between the peripheral zone and the central gland. Usually the tumors appears as an hyposignal.
- Diffusion Weighted imaging (DWI) provides functional information about tissue microstructures. This imaging technique is sensitive to the motion of water proton within the tissues. Because many prostate tumors present higher cellular density with more complex intracellular microstructure, the diffusion of water is restricted, which is detectable on DWI images. Even

more, the apparent diffusion coefficient map produce from DWIs at several scales can be directly used to locate and grade the tumors.

- Dynamic contrast-enhanced imaging (DCE-MRI) is build from a set of fast acquisitions during the diffusion of a contrast medium bolus. The tumors can be detected because their angiogenesis produces a different microvascular density, and so a different blood flow. The diffusion of the contrast medium within the tumors is different compared with the surrounding organs.

- MR spectroscopic imaging (MRSI) provides information about relative concentrations of various metabolites in tissues. If this imaging technique brings good information about the metabolites that are present in higher concentrations in prostate cancers compared with normal tissue, its main drawback relies in the low spacial resolution. Moreover, prostate MRSI is technically challenging and time-consuming, and many centers do not include MRSI in their protocols.

The combination of fusion of these multi-parametric images for prostate cancer diagnosis and localization is still an open research topic (Haider, van der Kwast et al. 2007).
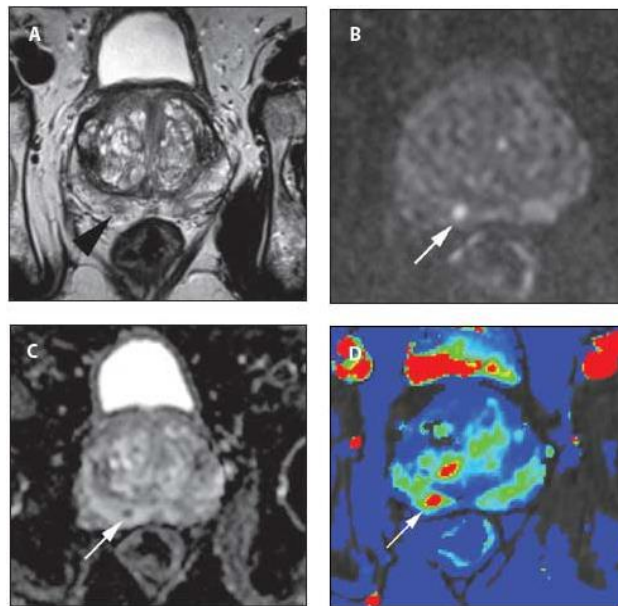
Fig 1.2: A 65-year-old male with prostate-specific antigen (PSA) level of 5.1 ng/ml and prior negative transrectal ultrasound (TRUS)-guided biopsy was referred for multi-parametric prostate MRI: (A) T2-weighted MRI; (B) Diffusion weighted MRI; (C) Apparent diffusion coefficient MRI and (D) Dynamic contrast-enhanced (Gupta, Kauffman et al. 2013)

Like ultrasound imaging, MRI is sometimes used to identify targets for prostate biopsy. In some cases, the urologists target prostate cancer by using the fusion of MRI and ultrasound (US) (Singh, Kruecker et al. 2008). Research shows that fusion MR/US guided prostate biopsy detected 33% of cancers compared to 7% with standard ultrasound guided biopsy (Natarajan, Marks et al. 2011).

However, MRI is mostly used in the diagnoses for the staging. As it is fast and relatively reliable, MRI is used to locate the tumor and define the uni-or bilateral lesions. It helps to access the tumor volume. It can detect as best an extracapsular extension (Cornud, Bellin et al. 2006). It helps also to find an affected lymph node if the presumption is high.

The lymph node metastases can be identified by on not only MRI but also on other imaging method, like CT or PET (Hall, Kwon et al. 2012). If the results of the different tests lead to an intermediate risk, a bone scan should be performed to detect possible metastases finally.

1.4 Treatment

There are many kinds of treatments for prostate cancer including active surveillance, surgery, radiation therapy, High-Intensity Focused Ultrasound (HIFU), chemotherapy, cryosurgery, hormonal therapy, and sometimes combination of treatments. Because the treatments of prostate cancer can have significant side effects, such as erectile dysfunction and all urinary incontinence, the choice of a treatment needs to balance the benefits of the therapy with the risks of lifestyle alterations. It usually depends on the stage of the cancer, the Gleason score, and the PSA level, and also related to patient's age, general health, feelings about potential treatments and possible side effects of treatment.

- Active surveillance
In early stage when slow-growing prostate cancer is suspected, the doctor will suggest to take active surveillance which means observation and regular monitoring without invasive treatment. Active surveillance is kept till the risks of surgery, radiation therapy, or hormonal therapy outweigh the possible benefits. When there are signs that the cancer expansion is accelerating or if new symptoms are developed, other treatments can be considered. Approximately one-third of men choose active surveillance for early stage tumors when they have signs of tumor progression, and many of them may need to begin treatment within three years (Wu, Sun et al. 2004). But generally, the increasing of the disease progression risk or the appearance of

metastasis is small if the program of surveillance is followed closely. Study results in 2011 suggest that active surveillance is the best choice for older 'low-risk' patients. It should be noticed that active surveillance may not mean avoiding treatments, but may reasonably allow a delay of a few years or more, during which time the quality of life impact by active treatment can be avoided.

- Hormonal therapy

Dihydrotestosterone (DHT) is a hormone produced in the prostate and it is required for the growth and spread of most prostate cancer cells. A feedback loop of DHT involving the testicles, the hypothalamus, and the pituitary, adrenal, and prostate glands controls the blood levels of DHT. Low blood levels of DHT stimulate the hypothalamus to produce gonadotropin-releasing hormone (GnRH). Then, GnRH stimulates the pituitary gland to produce luteinizing hormone (LH), and LH stimulates the testicles to produce testosterone. At last, testosterone from the testicles and dehydroepiandrosterone from the adrenal glands stimulate the prostate to produce more DHT. Hormonal therapies target the pathways used to produce DHT. Medications or surgery can be used to block prostate cancer cells from getting DHT, and usually they stop the growing and even make shrink the prostate cancer. There are several forms of hormonal therapies, such as orchiectomy, antiandrogens, total androgen blockade (TAB), GnRH antagonists or agonists and abiraterone acetate. They interrupt the DHT producing pathway at different point. Orchiectomy and GnRH agonists are considered as the most successful hormonal treatments, but they also have some disadvantages. The psychological impact of removing the testicles in orchiectomy can be significant, and sterility is certain. GnRH agonists eventually cause the same side effects as orchiectomy but may cause worse symptoms. It should be noticed that prostate cancer is rarely cured by hormonal therapy, and the cancer cells will become resistant after one or two years.

- Surgery

Radical prostatectomy is proved to be effective when tumor have not spread beyond the prostate boundary (Bill-Axelson, Holmberg et al. 2005). The surgery is traditionally used alone when the location of cancer is detected within the prostate. It is a common treatment as a first intention or when other therapies failed. However, in this latter case, because other therapies can cause tissue changes, radical prostatectomy has higher risks of complications and side effects. There are several types of radical prostatectomy. The radical retropubic prostatectomy, in which the surgeon removes the prostate through an abdominal incision, is the most common type of prostatectomy. In radical perineal prostatectomy, the surgeon removes the prostate through an incision in the perineum, the skin between the scrotum and anus. In contrast with the open surgical

form, laparoscopic radical prostatectomy is made through a series of small (1 cm) incisions in the abdomen. The surgery can also be performed with robotic technology. When compared to radical retropubic prostatectomy, robotic-assisted laparoscopic prostatectomy ensures a higher precisions in the gesture, a better sight of the scene (scene magnification or 3D view) and some movements not available in the classical laparoscopy (Smith Jr, Chan et al. 2007). The cure rate of prostatectomy depends directly on the risk factors (PSA level, Gleason grade, etc). However, radical prostatectomy may cause erection problems (impotence) in up to 70% of men and 20% will have minor problems with urinary incontinence.

- Cryosurgery

Cryosurgery is a prostate cancer therapy in which the surgeon exposes the prostate to freezing temperatures. In this surgery, the doctor will insert metal rods under ultrasound guidance, through the skin of the perineum into the prostate. These rods are cooled by highly purified argon gas, and freeze the surrounding tissues at $-186°C$. The cells of the prostate will die because of the freezing. During the therapy, the urethra is protected from freezing by a catheter filled with warm liquid.

Compared with other treatments, cryosurgery may decrease the risk of urinary control problem, but it will cause impotence up to 90% of the time. Some research showed that cryosurgery has a 10-year biochemical disease-free rate superior to all other treatments including radical prostatectomy or any form of radiation. (Bahn, Lee et al. 2002) It is demonstrated to be superior to radical prostatectomy for a recurrent cancer following a radiation therapy.

- Radiation therapy

Normal cells are able to repair themselves from radiation damage, while cancer cells are not. Radiation therapy exploits this fact to treat prostate cancer. Normally, radiation therapy uses ionizing radiation such as gamma and x-rays to kill prostate cancer cells. When radiation is absorbed in tissue, it damages the DNA of cancer cells, which lead to apoptosis (cell death). It can be used to treat all stages of prostate cancer. It is also used after an unsuccessful surgery. There are two kinds of radiation therapy in prostate cancer treatment: external beam radiation therapy and brachytherapy.

External beam radiation therapy uses directed high-energy x-rays beam produced by a linear accelerator towards to the prostate. The Intensity Modulated Radiation Therapy (IMRT) is used to adjust the radiation beam according to the shape of the tumor. High doses will be focused on the prostate and seminal vesicles, and low doses on the bladder and rectum to avoid damage. This therapy is given in radiation therapy centers for several weeks. The IMRT system provides fewer side effect than traditional surgery (Zelefsky, Fuks et al. 2002). The stereotactic body radiation therapy (SBRT)

technology is also used to treat prostate cancer. The new trends of this therapy concerns image-guided radiation therapy (IGRT) that includes imaging to increase the accuracy and precision of target localization, and the following of the dose over the treatment period (de Crevoisier, Louvel et al. 2009).

Brachytherapy is another treatment choice for patients with low intermediate risk features. It consists in implanting small "seeds" containing radioactive material into the tumor. While patients are under epidural or general anesthesia, the doctor implants under US guidance about 100 short-range radiation-sources seeds with a needle through the perineum directly into the prostate. After the radiation period, the seeds become inert and remain in the prostate permanently. Generally, the risk that men with implanted seeds will expose other people to radiation is accepted to be insignificant (Perez, Hanks et al. 1993). It is associated with good 10-year outcomes with relatively low morbidity (Nag, Beyer et al. 1999). The survival rate is similar to that found with EBRT or surgery (radical prostatectomy), but with fewer side effects such as impotence and incontinence (Frank, Pisters et al. 2007).

Both types of radiation therapy may cause side effects, including diarrhea and mild rectal bleeding due to radiation proctitis, as well as potential urinary incontinence and impotence. Most symptoms tend to disappear after a period, except erections which will be worse as time progresses. In some surgery, the doctor will place an absorbable spacer between the prostate and rectum to reduce rectal radiation injury.

- High intensity focused ultrasound

High intensity focused ultrasound (HIFU) technology has been shown to be effective in prostate cancer treatment. The HIFU device focus ultrasound waves to the tissues to be ablate or destroyed. The acoustic waves absorbed by the tissues are converted into heat increasing the local temperature until the tissue necroses. The ultrasonic waves focus point can be displaced over the volume to be destroyed (the all prostatic volume or some specifically areas). The spacial containment of the focus points lower the risks of affecting other tissue or organs, and so lower sthe risk of both incontinence and impotence (0.6% and 0-20%, respectively) (Uchida, Ohkusa et al. 2006). According to international studies, HIFU treatment has a high success rate with a reduced risk of side effects. Studies using HIFU have shown that 94% of patients with a pretreatment PSA of less than 10 ng/mL were cancer-free after three years (Uchida, Ohkusa et al. 2006).

- Palliative care and alternative therapies

When cancer cells spread to neighbor area of the prostate or produce metastasis, the disease goes to advanced-stage. Palliative care is usually used to extend life and relieve the symptoms of metastatic diseases. Abiraterone Acetate treatment causes a

dramatic reduction in PSA levels and tumor size in aggressive advanced-stage prostate cancer for 70% of patients. Chemotherapy is also used when prostate cancer goes to advanced-stage. It may be offered to slow the disease progression and postpone the symptoms. For example, a study showed that the median survival was 16.5 months in the mitoxantrone group, 18.9 months in the group given docetaxel every 3 weeks, and 17.4 months in the group given weekly docetaxel (Tannock, de Wit et al. 2004). Bisphosphonates, for example zoledronic acid, have been proved to delay skeletal complications, including fractures. For patients with hormone-refractory metastatic prostate cancer, bisphosphonates will also be used to satisfy the need for radiation therapy (Saad, Gleason et al. 2002). Metastatic disease may cause bone pain in some cases. Opioid pain relievers such as morphine and oxycodone are used to relieve pain. Injections of radioisotopes, such as strontium-89, phosphorus-32, or samarium-153, also target bone metastases and may be helpful in pain relief.

Other therapies are also consider for prostate cancer as alternative to active surveillance or definitive treatments. A vegan diet (fish allowed), regular exercise, and stress reduction have been shown effective to lower PSA level in men with apparent localized prostate cancer (Ornish, Weidner et al. 2005). These research have proved to be durable after two-years' treatment so far. Phytochemicals in plants may also have cancer benefits. For example pomegranate juice seems to reduce the PSA growing on patients which had a first therapy (Pantuck, Leppert et al. 2006).

1.5 Imaging guided therapies

The trend in surgery and even for other therapies is to propose less and less invasive interventions. Since 20 years, the scientific progress in computer science and medical imaging, but also by the definition of new therapies, led to the development of computer-guided therapies. A definition of computer-guided therapies has been given in (Lavallée, Cinquin et al. 1997): "Methods and systems which assists the physician in the efficient and quantitative use of data coming from several modalities (often imaging systems), with the aim of planning but also achieving a medical intervention".

The first attempts of surgical gestures assistance were involved in stereotactic approaches (Spiegel, Wycis et al. 1947, Galloway and Maciunas 1990). In these approaches, a frame fixed physically on the patient allows to locate the tools relatively to the anatomy, this despite the limited available imaging (X-ray radiography). From this starting point, therapies have been improved by new imaging techniques, new navigation systems, robotics and new therapeutic practices. In her review, J. Troccaz (Troccaz 2009) described three main evolution periods: (i) the realization of positioning tasks, with mainly applications built on simple paths and rigid structures,

such as neurosurgery and orthopedics (1985-1995), (ii) the definition of interactive procedures for more complex gestures, such as endoscopic surgery on deformable structures (1990-2005) and (iii) robots that perceive, communicate and act within the human body (since 2000).

The main clinical expected benefits of computer-assisted therapies are:

- the reduction of the invasiveness of the therapy;
- the improvement of the surgical accuracy by the definition of an optimal planning and a strict application of this planning;
- to secure the gesture;
- the reduction of post-treatment complications risks;
- the reduction of the intervention duration and costs;
- the reduction of radiation exposure for the patient and the medical staff;
- the design and performance of new difficult procedures;
- the integration of previous results in the surgical planning;
- the basis for surgical gestures training simulators;...

In prostate cancer treatment, image guided therapies also gained importance with minimal invasive prostatectomy (laparoscopic or with a robotic surgical system (Abbou, HOZNEK et al. 2001)), prostate brachytherapy (Wei, Wan et al. 2004), image guided radiotherapies (Otto 2008), HIFU...

More generally spoken, image guided therapies can be seen as a process of Perception - Decision - Action (Cinquin, Bainville et al. 1995). The Perception is performed through the direct visual perception of the physician but also through the several imaging devices or the several multidimensionnal sensors available on the several stages of the therapy. This information is fused to form a generic or patient specific intervention model in which the planning and the gesture will be performed. The Decision occurs during the development of an operational strategy and in the achievement of the gesture. The decision is performed on the model defined by the perception. The Action is then performed by the practician assisted by a navigation or a robotic system. However, this global framework is not so linear in the sense that the action can modify the perception and the decision in a loop (or collaboration) between the real world and the patient specific model (Haigron, Luo et al. 2009).

The applicability and the success of image guided minimally invasive therapies depend on some specific technological key elements like image segmentation, image modality registration, visualization tools, motion or gesture tracking, real-time capabilities... These key elements will occur on all the several stages of the procedure workflow and will have a direct impact on its success.

In the next chapter, we will describe a specific prostate cancer therapy, the HIFU

ablation. The several perception tools, the patient specific therapy planning strategy and the therapy itself will be described and discussed.

Chapter 2: HIFU therapy and registration problem

The work of this thesis has been performed in the context of the ANR TecSan MULTIP project dealing with HIFU therapy. In this chapter, we will extend the analysis of prostate cancer HIFU treatment after the brief description done in chapter 1. We will introduce not only the principle and workflow of the HIFU treatment, but also the components of a specific HIFU device. These details could help us to understand the role and importance of the problems that we are facing in this work. It's obvious that most of these problems are general in nature and may affect other medical applications (hepatocellular carcinoma treatment, thyroid tumors, etc.). But being restricted to prostate can better target our purpose.

2.1 HIFU therapy

2.1.1 Principle of HIFU thermotherapy

The idea of using ultrasound as a tool for non-invasive surgery appeared very early after the discovery of the biological effects of ultrasound waves. In the 50s, the Fry brothers effectuate work on the external treatment for neurological disorders. Directing the ultrasound on the treatment area, they noticed the occurrence of tiny lesions. However, the development of this type of therapy has been interrupted because of the absence of a sufficiently powerful and accurate visualization device. In the 80s, Lizzi, created a device for the treatment of glaucoma and intraocular tumors with more advanced technology. Extracorporeal shock wave lithotripsy is another high-energy ultrasound technology for the treatment of kidney stones which has been applied for the first time on humans in 1980. From the 90s to now, therapeutical ultrasound applications had a rapid growth. The ultrasound is considered as a mean of generating heat in a non-destructive way. Alone or in combination with other therapies, ultrasound generates high energy beam for the ablation of tumoral tissues or for occlusion of vessels. There are many studies in this area, specifically for the treatment of liver tissue, the kidney tissue removal or the tissue destruction in the spleen and breast. Some research is also done to coagulate the vessels to stop bleeding or for the myocardial revascularization of heart muscle. Ultrasound is especially interesting in a therapeutical context due to its minimally invasiveness and

selectiveness e.g. intracavitary approaches, with laparoscopic, endoscopic or external and focus probes.

Urology and moreover the treatment of prostate cancer is probably the medical application field where the clinical use of HIFU is the most advanced. This application tries to destroy the prostate cells by heating. The principle of ultrasound thermotherapy is the following. The transducer sends continuous ultrasound waves to the tissues to be destroyed. The sound pressure variations produced by the transducer generate local tissue motion (expansion and contraction) whose amplitude is proportional to the pressure level. But the tissue response is not perfectly elastic. During its propagation in the environment, the acoustic wave amplitude decreases, in particular because of absorption. The energy loss of the pressure is then transformed locally as heat which increases the tissues temperature. In the case of a focused transducer, the concentration of the ultrasound beam produces a maximum pressure variation at the focal point. The intense absorption of ultrasonic pressure leads to a sudden and fast rise in temperature, destroying the cells located in the treated area by coagulation which induces the necrosis. The temperature rise occurred around the focal point, propagates also to the neighbor area by heat diffusion. This diffusion depends not only on the ultrasound pressure deposit but also on the duration of the exposure.

Due to its minimal invasive and no radiation property, HIFU technology plays an important role in prostate cancer treatment. Today, prostate therapies are the main clinical commercial application for HIFU, thanks to some new technological progress (piezoelectric technology, image processing, medical treatment method, etc.). Some of these improvements are particularly noteworthy:

- Image guided therapy

In past few years, HIFU therapy has taken benefit from the development of imaging technique. The medical images from different imaging modalities not only offer high resolution anatomical information for pre-operative planning, but also make it possible to obtain real-time image to guide the therapy during the intervention.

High resolution images, such as computed tomography (CT), magnetic resonance image (MRI) and transrectal ultrasound (TRUS) images, may provide spatially localized information to support the surgical planning.

Meanwhile, real-time imaging techniques like US make it possible to scan the organ during the intervention. The real-time imaging can display the surgery target (tumors, etc.) and the intervention tools (probe, etc.). It helps surgeons to guide the therapy on lesion area, to make some adjustments when the organ deforms, and to

control the therapy by temperature measurements. Usually, TRUS, fluoroscopy and MRI are used to estimate the prostate volume for surgery guidance.

- Pre-operative planning

With some high resolution imaging technique, the surgeon can now establish the specific anatomical model of a patient. According to the anatomy information, the surgeon will define the target to be treated and the zone which should be avoided. Usually, the organ will be divided into a series of blocks, and dose of each block could be decided by simulation. This step will establish the closets patient specific planning just before the intervention. In section 2.2, we will give a specific example of a pre-operative planning before HIFU treatment.

- The evolution towards partial treatment or targeted tumors

The strategy of HIFU treatment today is totally devoted on the destruction of the whole prostate to prevent the recurrence of cancer, and on avoiding the surrounding tissues. This strategy is characterized by the complete loss of the organ's physiological functions with some high risks of side effects (blood in urine, difficulty passing urine, etc.). As mentioned before, high resolution imaging technique and image guide therapy process allow the surgeons to delineate more and more precisely the tumor within the prostate. The focused treatment, which is not applied to the whole prostate but only focused on the tumor area, can be now considered. The prostate sparing treatment could destroy only the tumor and so minor the side effects.

2.2 Ablatherm device and MULTIP project

2.2.1 Ablatherm device and HIFU therapy

Several manufacturers are positioned in this technology area about HIFU prostate surgery, such as EDAP Technomed, Insightec, etc. EDAP is actually the market leader. Ablatherm, the clinical products of EDAP designed in collaboration with INSERM 556 Lyon in the early 90s, is currently used for the treatment of prostate cancer by HIFU in Europe, Canada, Russia, Australia and South Korea. Since the first patient in 1993, the number of treatments has been increasing (Fig 2.1). We will give a description of the Ablatherm and the associated therapy guidance based on the product sold today. It is obvious that it will continue to evolve in the coming years, significantly in the transducer part with the arrival of potentially CMUT (Capacitive Micromachined Ultrasound Transducers) technology, different transducer geometries, phased array transducers, more sophisticated data processing ... This presentation can

therefore quickly become obsolete.
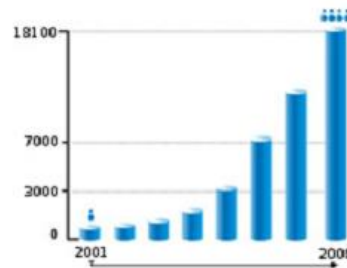
Fig 2.1 Evolution of the number of HIFU treatments since 2001
(http ://www.edap-tms.com)

The present device (Fig 2.2) is composed by a table on which the patient is positioned. This table supports the therapeutic and imaging endorectal probe. This equipment is completed by a control module which enables the surgeon to plan and check the treatment via a computerized system which guides the robotic endorectal probe. Figure 2.2 illustrates the endorectal probe used during the therapy. The therapeutical ultrasound piezoelectric transducers have the form of a spoon. In the center of the transducer is the ultrasound imaging part used for the therapy planning. This imaging tranducer has a central frequency of 7.5 MHz, while the therapeutical transducer generates ultrasonic waves with a frequency of 3 MHz. During the therapy, this probe will be covered by a degassed balloon filled by water which serves for the ultrasound coupling to the patient tissues. This liquid is set in a continuous flow in order to cool the probe and to preserve the patient's rectal wall.

Fig 2.2 Ablatherm device and probe for imaging and therapy
(http://www.edap-tms.com).

During the therapy, the heat produced by the high intensity ultrasound usually causes the swelling of the prostate. A urethra resection is performed to prevent the compression by this swelling, and a catheter is introduced to ensure the urine flow.

Once the patient is installed on the bed, the endorectal probe is inserted within the rectum and positioned in front of the prostate. The treatment is divided into two steps: The lesion planning on an US volume (Fig 2.3 a) and the treatment by HIFU (Fig 2.3 b).
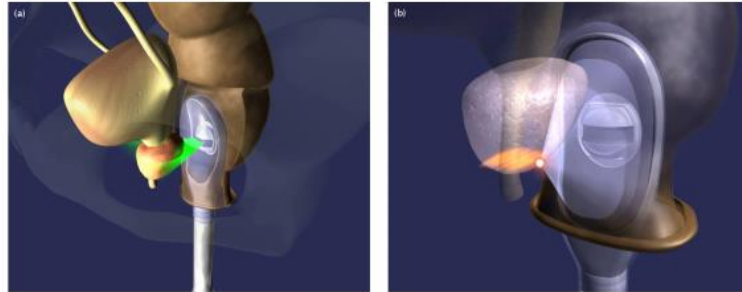
Fig 2.3 (a) Acquisition of ultrasound prostate (b) Treatment with HIFU (http://www.edap-tms.com).

The planning step begins with a first acquisition of the prostate volume by an ultrasound scan. The ultrasound imaging device produces a set of equidistant and parallel slices (Fig 2.4 a) with a transverse resolution of 0.154 mm/pixel and a size of 500×490. The ultrasound slices are then interpolated in the 3rd dimension to make an isotropic volume. It can be then displayed on the screen as an axial or a transverse plane. In the transverse plane (Fig 2.4 a), the operator annotates then manually the base and the apex. These annotations allow defining the treatment zone and moreover the safety distances in relation to the sensitive areas. Especially in order to preserve the sphincter at the apex to ensure continence, the treatment will not be applied to the area less than 6 mm from the apex. At the other side, the seminal vesicles at the front of the prostate (pubic symphysis side) do not present a risk, and no sequels have ever occurred in the bladder. The prostate is then divided into a series of blocks. On these blocks, the software proposes then a set of axial slices on which the operator annotates the rectal wall (Fig 2.4 b). Because the rectal wall is sensitive to temperature, a security distance of 3 to 8 mm to the wall is set to limit the lesions and avoid a fistula. For each defined area, the software will calculate the appropriate number of lesions.
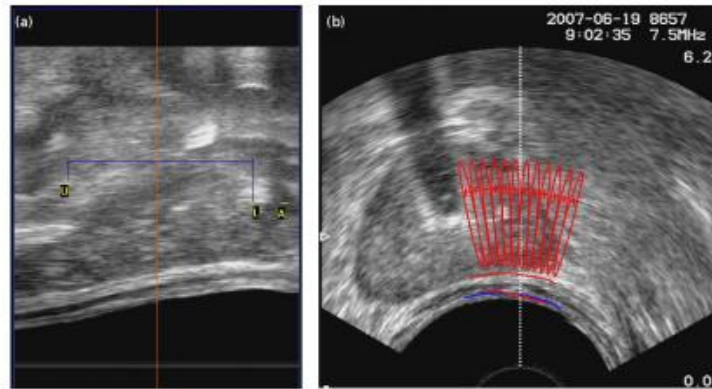
Fig 2.4 Planning (a) Annotation of the base (U), the apex (A)
and a margin of safety (L) on the transverse slice, (b) Definition of
the rectal wall and a variety of lesions in the left lobe on an axial
slice

Once the treatment has been planned, the shooting phase can automatically begin. The planned area is covered by a set of 6 seconds long shots, interrupted by a waiting time of 4 seconds. The geometrical shape and the phased array of the therapy probe helps to focus the ultrasound beam to the previously defined points. The temperature reaches 85 to 100°C at the focal points. The lesion height range from 19 to 26 mm (anterior-posterior distance) enables the prostate height to be treated in a single pass. Between 400 and 800 adjacent elementary lesions are required to cover the whole prostate volume. The image of the processed slice is displayed in real time. A motion sensor keeps the distance between the lesion and the rectal wall. The cooling water temperature control ensures the patient safety. In case of some therapy failure or patient movement, the treatment will be paused with an alert message to the surgeon.
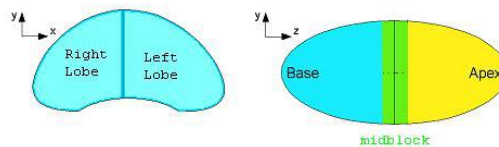
Fig 2.5 Division of the prostate for a block processing.

If the prostrate is big, the treatment must be performed in several blocks (Fig 2.5) because the prostate shape can deform during therapy (edema, etc.). In this case, a new sequence composed of ultrasound acquisition, pre-operative planning and heating is performed for each block. The treatment time is between 1.5 and 2.5 hours, depending on the volume of the prostate.

The advantage of this technique is that it is precise and easy to control. It enables the surgeon to choose different treatment options, such as a complete treatment or

partial and nerve-sparing treatment. The HIFU therapy can be not only applied as a first intention treatment, but also employed in failure of a previous therapy (radiotherapy, brachytherapy, or a first HIFU treatment). According to these different situations, the treatment protocol will be adapted to avoid the risk of overheating, for example, already treated prostate should be less perfused and so will cool more slowly than normal tissues.

In some cases, a tumor recurrence after HIFU treatment remains. It is mainly due to the margins taken at the apex to avoid the urethral sphincter damage. Because this area is only treated by heat diffusion, the tissue necrosis depends mainly on the patient's tissue characteristics.

2.2.2 MULTIP project and problem statement

More and more research showed that radical prostatectomy surgery or radiotherapy often lead to side-effects (urinary incontinence, erectile dysfunction, bowel toxicity, for example) (Ahmed, Hindley et al. 2012). Because the diagnoses imaging (i.e. multi-parametric prostate MRI) will allow to discriminate the tumor more and more precisely in an early stage, the current trend is to perform focal therapy by only treating the tumor area within the organ (Eggener, Scardino et al. 2007, Lazzeri and Guazzoni 2010, Rouvière, Gelet et al. 2012). A large volume treatment and time consuming procedure could so be avoided. In the future, the new HIFU device must be able to locate the tumor area and then to focus the ultrasound waves to this specific lesion area.

The aim of the MULTIP project (Matrice de transducteurs Ultrasonores pour La Thérapie et l'Imagerie de la Prostate) is to improve the current device by using up-to-date piezoelectric technologies and image processing methods (Mari, Bouchoux et al. 2013). This new device must be more efficient in focal treatment of prostate cancer tumors. For this, the future device should comply the following requirement of clinical applications: 1) being small in size to be inserted into the rectum; 2) embed a guiding device such as an ultrasound imaging transducer; 3) enable a precise treatment of locate tumors while maintaining the global prostate treatment ability; 4) being used in the operating room by an urologist or radiologist.

As a result of this project, some protototypes of a dual mode ultrasonic probe have been developed. The main ideas were to propose a new geometry of a multi-element therapy probe in order to deflect electronically the position of the US focus and to integrate in the middle of this probe a dual-mode (therapy and imaging) array. This imaging section will be used, as for the previous Ablateherm procedure, to plan and guide the treatment in the operating room.

Because the aim of the new probe is to allow a focal tumor treatment, the treatment planning and image guidance have to be modified according to the imaging capabilities. An US imaging system (embedded in the therapeutical probe or an even more dedicated TRUS with better resolution and post-treatments) is not able to locate the tumor within the prostate. So at contrary to the whole prostate treatment, the focal tumor therapy under US imaging guidance is not directly possible. For the moment, only MRI can be used to describe the prostate, its different zone and the tumor with sufficient contrast and resolution. The main idea for the therapy guidance in the MULTIP project is to use a clinical pre-operative T2 MRI volume to locate the tumor within the prostate and then to use this information within the US guided therapy. This fusion of information can be performed by registering the pre-operative T2 MRI volume to the pre-operative ultrasound images.

The MRI prostate zonal segmentation and tumor delineation is a problem at itself and many research works are still devoted to this purpose (Ghose, Oliver et al. 2012). Some solutions exists, the simplest one is the delineation of the tumor by a radiologist or an urologist. Because the aim of this thesis is to propose a guidance strategy, we choose to consider the tumor delineation problem as solved, and we focus our work on the fusion of the preoperative MRI extracted information into the peroperative US volume.

A MRI/US registration, which aligns the prostate in MRI volume to prostate in US volume, is necessary in HIFU focal prostate tumor treatment. The aim of this registration is to map the information about the tumor location from MRI to the preoperative US image used to plan and guide the process. In the following section, we will introduce the framework of MRI/US registration research.

2.3 MRI/US registration problem - presentation of the research framework

2.3.1 MRI for pre-operative imaging

As we mentioned in the previous section, a pre-operative planning is necessary before the prostate cancer therapy. In this planning the target and the several operative steps of the intervention are defined. Usually, the surgical decision about the future intervention is based on some clinical information which is not necessary based on spatial or anatomically information. However, in the case of prostate focal intervention, MRI techniques may offer some advantages, specifically because they provide spatially localized information to help the planning, particularly for robotic or

image guided therapies.

MRI offers a suite of sequences to enable the prostate cancer detection, grading, spatial localization, etc. For surgical planning, a MRI is typically performed 6–8 weeks after a prostate biopsy to avoid the effect of hemorrhage artifact. Usually endorectal MRI is used because it provides better spatial resolution than transabdominal MRI. The aim of the conventional MRI includes providing the entire prostate size, distinguishing the zonal anatomy, the seminal vesicles and the rectum, detecting the enlargement of local lymph nodes, etc. Several MR sequences are available for this purpose. On T1 weighted sequences, the bladder and seminal vesicles are homogeneously gray, the fat surrounding the organ has hypersignal, and the bladder which is filled with urin is in hyposignal. On T2 weighted images, the prostate is divided to bright peripheral gland, heterogeneously bright central gland and anterior fibromuscular stroma. Therefore, the T2 MRI could be used to identify the prostate zonal anatomy and the extracapsular integrity. On T2 MRI image, the lesions of prostate are typically hypointense in the peripheral zone which is normally hyperintense, or may appear as homogenous and with low signal intensity in the transition zone which is normally heterogeneous. In our case, we chose T2 weighted MRI for the pre-operative planning because of its ability of locating the lesion in the prostate (Fig 2.6).

(a)   (b)
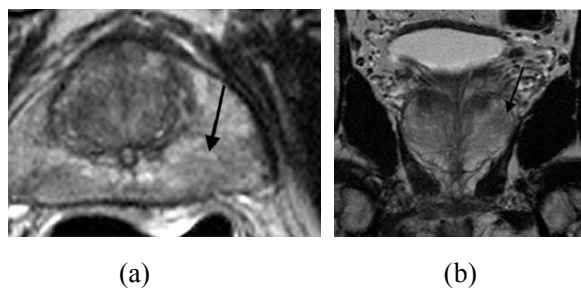
Fig 2.6 Axial (a) and coronal (b) T2 MRI of the prostate of a
65-year-old man with a cancer in the left peripheral zone (Tan,
Margolis et al. 2012), and a Gleason Score of 3

It should be notice that the MR imaging techniques to locate the tumor are still in development. Some functional imaging techniques such as diffusion weighted imaging, dynamic contrast imaging, diffusion tensor imaging, and MR spectroscopy could be complementary techniques to conventional MRI, especially to locate the tumor (Alonzi, Padhani et al. 2007) (Aigner, Pallwein et al. 2007) (Beyersdorff, Taymoorian et al. 2005) (Gerst, Touijer et al. 2005) (Sciarra, Barentsz et al. 2011) (Langer, van der Kwast et al. 2009). Although our work is based on T2 weighted MR image, it could be adapted to other functional MR images.

2.3.2 Ultrasound for inter-operative imaging

Transrectal ultrasound (TRUS) can be used before the intervention for biopsy guidance. But as mentioned in the Ablatherm procedure, in our case, TRUS is used in the intervention as the image to estimate the prostate volume and plan the location of the future HIFU spots.

The imaging transducers are part of the therapeutic probe. The probe is inserted within the rectum and positioned in the front of the prostate. The image transducers have a central frequency of 7.5 MHz and can acquire an axial circular section. A translational movement of the probe allows to scan the prostate as a peroperative TRUS volume. Although TRUS is able to image the whole prostate gland in real-time, it still has limitations to discriminate the several prostate zone and the tumor because of its low sensitivity. In our case, the quality and resolution of the acquired TRUS volume are even lower that actual TRUS, because the dual mode transducers have to make a compromise between the imaging capabilities and the therapeutical efficiency.

In an US image, the tissues are characterized by speckle. Speckle arises from the signal interference caused by tissue micro-inhomogeneities (tissue cells, capillaries, blood cells, etc). This coherent summation of backscattered signals forms a spatial distribution of speckle that is specific to the density and distribution of the scatterers and thus to the nature of the tissue. The contrast itself between the prostate and surrounding organs is usually not high enough to well distinguish the tissues boundaries. Moreover, the inter-operative TRUS image is affected by the shadow of the urethral catheter used to protect the urinary outflow during the therapy.

Although the TRUS is the most convenient way to image prostate, it can not offer enough information for a focal prostate cancer HIFU therapy. The important information, such as the prostatic structures and the tumor itself are not visible. This information should be acquired by another imaging method, and mapped to the peroperative TRUS image by registration.

2.3.3 MR-US image registration

We already notice that a precise pre-operative planning and an image driven guidance during the intervention are needed in a minimally invasive therapy. Although the probe of the HIFU device offer real-time ultrasound image of the inter-operative processing, the ultrasound images could not offer enough information about the lesion detection because of its low resolution and speckle distribution. On the other hand, we can get high quality information about the prostate anatomy and the prostate tumor on a preoperative T2 MRI. An obvious solution is to register the

pre-operative information from MRI onto the peroperative ultrasound images to improve the precision of the therapy. To solve this problem, we need to develop an algorithm to make the registration between 3D MRI and 3D ultrasound images. The estimated transformation is then used to propagate the information of the tumor area, which could be detected on MRI, to the ultrasound image in order to label the tumor area during the therapy (Fig 2.7).
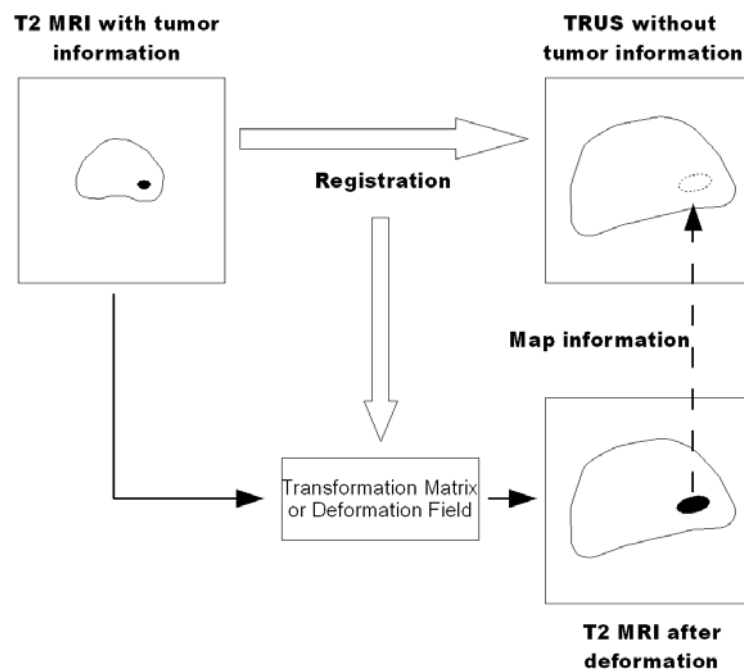
Fig 2.7 TRUS-MR registration. The information of tumor position
can be mapped from MRI to TRUS image.

Image or volume registration is one of the key steps of several image processings. It helps overlaying images of the same scene obtained from different imaging conditions (different time, viewpoints or sensors), and align these images geometrically into a common referential. Usually one image is considered as the reference image, the other image, called the moving image, will be geometrically transformed in order to match as close as possible to the reference image. In the past decades, several types of methods have been introduced for the image registration. See (Maintz and Viergever 1998) (Pluim and Fitzpatrick 2003) (Zitova and Flusser 2003) for some surveys.

Generally, most of the registration methods have a similar workflow:
- Define a similarity measure between the reference and the moving images.
- Apply some geometrical transformations (global or local) to the moving image.
- Apply an optimization method which allows finding the geometrical

transformation parameters that maximize the similarity measure between the two images.

2.3.3.1 Geometrical transformations

According to the geometrical transformations used for the registration, the several methods found in the literature can be classified as global (sometimes called rigid) or elastic registration.

- Global registration transformations are characterized by the fact that only a global geometrical transformation is performed on the moving image. This transformation can be the combination of rigid transforms (translation and rotation) and/or global non-rigid transforms, such as scaling and/or affine transform.

- Elastic transforms are related to the elasticity theory and they describe local deformations. The image content is considered as continuous bodies and different local deformations are applied on its different part. Several model of the deformation field are proposed in the literature going from the simplest (and fast) basis function extension (spline, etc.) to physical models (fluid flow, etc.). A non exhaustive survey can be found in (Holden 2008).

In our specific problem, the MRI-US registration, the deformation of the prostate is a problem which cannot be ignored in the registration framework. In fact, unlike as in the pre-operative situation in MRI, the prostate gland and its surrounding organs are deformed during the HIFU therapy because of the probe size, the balloon or even by the therapy itself. After a short term of the therapy, the focal ultrasound heating the gland will lead to an edema within the prostate, and deform it. This situation leads us to consider an elastic registration scheme.

2.3.3.2 Similarity measure

The similarity measure is the other key point of the several registration methods. Generally, two kind of information could be important in image registration: the voxels intensities and/or some image features. On one hand, all the image information is available in the distribution of its values. Some global intensity-based statistics analysis can then be used to estimate and maximize the similarity of the moving and the reference images. On the other hand the content of an image can offer some features that could be easily detected on both images by an image analysis method. These features are then used in a feature-based registration scheme. In more details:

- Intensity-based registration estimates the transformation by optimizing the measures calculated directly from the voxel values. This set of voxel similarity measures includes the sum of squared differences (SSD) (Hajnal, Saeed et al. 1995) (Hajnal, Saeed et al. 1995), correlation coefficient (CC), ratio image uniformity (RIU) (Woods, Cherry et al. 1992, Woods, Grafton et al. 1998) and partitioned intensity uniformity (PIU) (Woods, Mazziotta et al. 1993). Some information theory techniques consider the registration as trying to maximize the shared information between the moving image and fixed image. These information based measure class, includes joint entropy (Maes, Collignon et al. 1997), entropy correlation coefficient (Maes, Collignon et al. 1997), mutual information (MI) (Maes, Collignon et al. 1997), normalized mutual information (Studholme, Hill et al. 1999), point similarity measure based on MI (Rogelj, Kovačič et al. 2003), histogram energy (Bro-Nielsen 1997), correlation ratio (Roche, Malandain et al. 1998) and Woods criterion (Woods, Mazziotta et al. 1993). They are widely used in medical image registration, especially for inter-modality images registration.

- In feature-based registration, the measures to be optimized are not provides by the voxel intensities but the by the structure features in images. In medical image registration, the simplest features are the manual fiducial marks. In this case, special fiducial points are labeled on some special positions in both moving and reference image sets, and these image sets are aligned by the determination of transformation (rigid or elastic) that minimizes the distance between these fiducial points (Kaplan, Oldenburg et al. 2002) (Cool, Bax et al. 2011) (Natarajan, Marks et al. 2011). Other structure information, such as contour and surface, are also important features which can be used as registration measures. In (Narayanan, Kurhanewicz et al. 2009), the prostate surfaces are extracted from both 3D TRUS and MR images, and then a deformable surface registration is performed by using an adaptive focus deformable model (AFDM). In (Reynier, Troccaz et al. 2004), the rigid and elastic registrations are applied by aligning 3D point clouds constructed by segmenting prostate contours on TRUS and MR images.

In our specific case, both approaches are problematic and have some specific difficulties. We chose to explore an intensity-based and a feature-based registration approach. In the following part we will analyze the difficulties of these both approaches and give a brief description of our solutions.

2.3.4 Intensity-based registration

The most obvious solution to register the prostate from different imaging modalities is to use the intensity information contained in both images. This class of method is often used in medical imaging problems because no previous feature extraction is necessary, it can handle the registration of different modalities and its relative robustness (no influence of a feature extraction error, high number of information taken into account during the similarity measure estimation, etc.).

The difficulty in our case is that in ultrasound images the information about the several organs consists of a spatial speckle distribution and not on a specific gray level distribution. Some work has been done in cardiac ultrasound imaging to use intensity based matrix for US/CT registration (Huang, Moore et al. 2009) (Huang, Hill et al. 2006) (Sandoval and Dillenseger 2013) (Sandoval Z 2013). But in this ultrasound cardiac registration framework, only 2 structures have to be registered with to extreme speckle density cases: mainly the myocardium (speckle) and the heart chambers or main vessels (no speckle).

In our work, we will consider the speckle distribution in the ultrasound image as a texture characteristic for each structure. We will introduce a texture descriptor which could convert the speckle information to an intensity information. Some of the prostatic US image characteristics have to be taken into account for the choice of a tissue descriptor. The size (or scale) of speckle increases according to the distance from ultrasound probe, because of ultrasound beam form. Moreover, for circular probes, the ultrasound beam directions radiate from the probe center due to its geometry. The speckle orientations are so different, depending on its position across the image. This situation indicates that the texture descriptor should at least have rotation and scaling invariant properties. In Chapter 3, we will introduce such a texture descriptor based on moment invariants on rotation and scaling.

Although moment invariants based texture descriptor could extract regional information, and be applied to some TRUS image registration. But in the case of TRUS-MR registration, there is no such a texture distribution in T2 MR image. The prostate intensity distribution in MR image is much more inhomogeneous: the intensity of center gland is much lower than apex area, and the prostate boundary area has the similar intensity as the surrounding organs. So we did not continue intensity-based registration in our work.

2.3.5 Feature-based registration

The necessary condition of a feature-based registration method is that common information is available on both imageries. In medical images, these features usually are related to the position of bones or on other organ surfaces or on some other spatial anatomical structures, even on external implanted landmarks. If we can easily detect them on both moving and reference images, and simplify them to geometric features such as points, lines or surfaces, a geometrical transform could be estimated based on the corresponding relationship of these features.

But in our case, the registration between MRI and ultrasound images for prostate cancer surgery, the problem is more complicated. Since the moving and reference images are from different imaging modalities, they share little common information. For example, because of the speckle distribution and low resolution of ultrasound image, there are no much information on the prostate structures except the external surface and partially the urethra. On the other hand, T2 MRI has a good quality and a higher resolution especially in the image plane. It is very rich in features like the several prostate zone, the tumor if any, etc. However, when dealing with common information with US, it is mainly the prostate surface which can be used as a common feature. We propose to segment the prostatic surface both in US and MRI and then perform an elastic registration of this common information. Some method has been proposed to extract the surface of prostate in US (Ladak, Mao et al. 2000) (Gong, Pathak et al. 2004) (Shen, Zhan et al. 2003) (Zhan and Shen 2006) (Garnier, Bellanger et al. 2011). But in MRI, the surface of prostate is in hypo-signals and also share similar values with neighbor organs, such as bladder wall and the rectum. Moreover, MRI has no homogeneous intensity within prostate gland. It is not easy to extract some common features directly from the ultrasound image and the MRI. The feature based registration problem will then be a segmentation problem (for a review of the segmentation method in prostate MRI and a justification of the proposed method, see section 2.4).

The registration framework we will propose in chapter 5 is based on the following framework (Fig 2.8):

- Extract the surface prostate surface information from ultrasound images. For this we will use the work done at our lab by Carole Garnier which proposed active contours and Optimal Surface de Detection (OSD) for the extraction of the prostatic surface in MRI 3D ultrasound image (Garnier, Bellanger et al. 2011).

- Extract the surface in MRI. This part represents one of the contributions of this PhD Thesis. We adapted the OSD method to a multi-objects (prostate, bladder and rectum) surface detection in T2 MRI (see chapter 4).
- Perform the 3D elastic registration between both extracted surfaces (TRUS and T2 MRI).
- The 3D deformation field estimated from this surface-to-surface elastic registration will be used for the fusion of the tumor location information into the inter-operative US volume (see chapter 5).
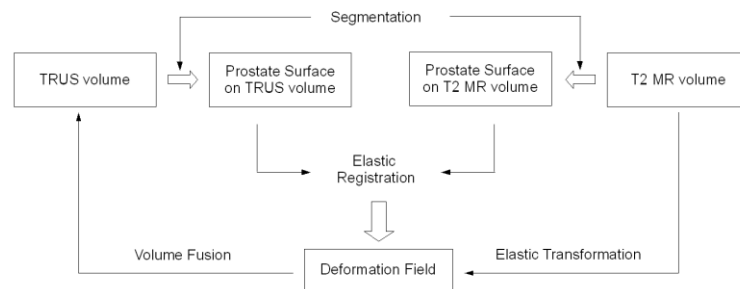
Fig 2.8 surface-to-surface registration framework

2.4 The segmentation

Prostate surface is an important measure for registration, but the surface segmentation itself is a challenging problem in medical image processing area. The manual segmentation by surgeon is time consuming and its accuracy depends on the specific surgeon. Moreover, the manual segmentation only offers contours on 2D slices, but not a 3D surface which is necessary in our registration. In the past few years, several prostate segmentation methods have been developed for different medical images (CT, MRI, TRUS) (Ghose, Oliver et al. 2012). Our work will only be focused on prostate segmentation on TRUS and T2 MR images. In this section, we will show the characteristic of TRUS and T2 MR images and the difficulties of their respective segmentation. After the review of some solutions given in the literature, we will make a brief description and justification of our work on prostate segmentation.

2.4.1 Ultrasound image segmentation

Even with a relative good 3D spatial resolution, TRUS image segmentation is a difficult task, due to its low contrast, speckle distribution and imaging artifacts. To improve the performance of segmentation, two kinds of prior knowledge are considered to be used: the shape and contour information of the prostate, and the

speckle distribution of TRUS image. Because of the low contrast and imaging artifacts, the prostate boundary may be not clearly defined in some special position near the bladder and rectum. Some prior knowledge can be given to initialize the contours and build a shape or contour based model. Ladak et al. (Ladak, Mao et al. 2000) interpolate four manual defined points on the prostate boundary to generate a discrete dynamic contour (DDC) (Lobregt and Viergever 1995), and segment prostate of 2D ultrasound images. In (Ding, Chen et al. 2003), the DDC is used in prostate segmentation in 3D ultrasound image, and the final contour on one slice is used to initialize the contours on neighbor slices. Hodge et al. (Hodge, Fenster et al. 2006) construct an active shape model (ASM) (Cootes, Hill et al. 1994) based on manual segmented contours. They divide the prostate mid gland images intro three regions and generate three shapes from each of them. Hu et al. (Hu, Downey et al. 2002) initialize an ellipsoid with manual defined axes, then they warp the ellipsoid to cross six manual marked points, and at last they deform the ellipsoid by internal and external forces to make the segmentation. Several other methods (Ding, Wei et al. 2006) (Badiei, Salcudean et al. 2006) (Saroul, Bernard et al. 2008) (Sara Mahdavi, Chng et al. 2011) are proposed to segment prostate by fitting curves (usually ellipsoid curves). Betrouni et al.(Betrouni, Vermandel et al. 2005) combine adaptive morphological filtering and median filtering to enhance the prostate contours, then they use a heuristic optimization algorithm on the contour initialized from a prostate model. In the work made in our group by Garnier (Garnier, Bellanger et al. 2011), a prostate surface mesh is initialized with eight manual marked points, then two kinds of algorithms have been explored for the prostate segmentation: the first algorithm, a DDC method, used internal forces, external forces and damping forces to push the initial mesh nodes to the prostate surface; the second algorithm, optimal surface detection (OSD) method, construct a graph by adding nodes and arcs based on the initial mesh, and apply a graph cut algorithm to segment prostate. According to the results in (Garnier, Bellanger et al. 2011), OSD based segmentation show higher accuracy. DDC based segmentation accuracy is a bit lower because it is sensitive to initial contour position, meanwhile it could be applied to OSD based segmentation results to improve final segmentation performance. The OSD based TRUS segmentation framework will be used in our work to obtain the prostate surface from TRUS image for the surface based registration scheme.

As we mentioned earlier, the TRUS image is composed by speckle. A specific tissue is so characterized by a specific speckle spatial distribution, but each speckle can have its own scale and orientation. One solution could be considering these speckles as a kind of texture distribution, and extract useful information with texture analysis. Zaim et al. (Zaim 2005) describe the ultrasound image by using texture

features, spatial information and gray-level values, and then use a self organizing neural network to segment the prostate. Richard et al. (Richard and Keen 1996) extract the texture features from ultrasound image, and use the mean shift algorithm to cluster these features and segment the prostate. Zhan et al. (Zhan and Shen 2003) use a Gabor filter to capture texture features of ultrasound image, and classify these features by SVM. These classified texture feature space are used as external force in a deformation model to segment the prostate. In (Zhan and Shen 2003), the same group proposes a method to combine texture and edge information to improve the performance of segmentation. On our work about the intensity based registration with the moment invariants texture description, we noticed that moment invariants with special order and repetition can give both regional and boundary information. Moment invariants can so be used to adapt to ultrasound the segmentation techniques where boundary information alone or in combination with regional information is needed, i.e. active contours, deformable models, level sets, etc. In chapter 3, we tried to prove the previous assessment, without loss of generality, by using the two kinds of moment-invariant features in a min-cut/max-flow graph cut algorithm. The preliminary segmentations results on simulated and real ultrasound images will demonstrate the benefits of the joint region- and boundary-sensitive moment-invariant texture features. Moment invariants are so eligible to be used to adapt techniques based on the combination on regional and boundary information to the segmentation of ultrasound images.

2.4.2 T2 MRI segmentation

T2 MR image of the prostate has a high resolution in the image but a low resolution in the third direction. As we noticed before, the intensity distribution inside the organ is inhomogeneous due to its complex structures and the prostate surface has a hyposignal. A traditional edge detector operator can detect many false boundaries on T2 MRI. Some model based segmentation methods, such as active contour model, active shape appearance model, are introduced to solve the problem. For example, Samie et al. (Samiee, Thomas et al. 2006) estimate the average gradient values based on prior shape information, and this information is used to trace the boundary of the prostate. Flores-Tapia et al. (Flores-Tapia, Thomas et al. 2008) construct a feature space from Haar wavelet coefficients in a multi-resolution framework, and use some prior shape information to trace prostate boundary in this feature space. Cootes et al. (Cootes and Taylor 2001) propose the active shape model (ASM) framework, and give a prostate segmentation as application of this model. Zhu et al. (Zhu, Williams et al. 2007) segment the prostate on MRI with a hybrid model of 2D and 3D ASMs.

Vikal et al. (Vikal, Haker et al. 2009) build an average shape model from manual contours, and segment the prostate based on this model. Tsai et al. (Tsai, Yezzi Jr et al. 2003) merge texture and shape into a level-set framework to segment prostate. Makni et al. (Makni, Puech et al. 2009) use a deformation model in a probabilistic framework initialized by a statistical shape model. Using our experience with the TRUS segmentation, in chapter 4 we will try to apply the OSD based segmentation on T2 MRI. In this approach we will introduce some shape prior information in this approach.

The other difficulty of the T2 MRI prostate segmentation comes from its surrounding organs. The capsule of prostate, which is a hyposignal in T2 MRI, has the same level intensity as outer and inner structures. In some slices around prostate to the apex and base, the segmentation accuracy is affected by the bladder and the rectum. Song et al. (Song, Liu et al. 2010) has proposed a multiple objects OSD framework to segment prostate and bladder in CT volumes. Inspired by Song's work, we propose a multiple OSD segmentation framework, which contains the information from bladder and rectum boundaries. Some prior knowledge, such as the thickness of the bladder wall, are introduced into this framework to improve our segmentation.

2.5 Summary: the contribution of thesis

In this chapter, we reviewed the HIFU prostate therapy process, and introduced the MULTIP project. This information is helpful to understand the role of TRUS-MR registration in a HIFU focal prostate cancer therapy.

Our first contribution of this thesis is to propose a moment invariants based texture descriptor for TRUS image. This texture descriptor is invariant to speckle rotation and scaling in the ultrasound image. It can be used to generate region information for intensity based registration. As we explored this descriptor, we found that the invariant values with special orders and repetitions can not only characterize the regional information of textures but also can show the boundary between different textures. In order to prove this ability of moment invariants, we encode both regional and boundary information into a graph cut segmentation framework, and give primary segmentation results on simulated and real ultrasound images. This part of work is already published in (Wu, Garnier et al. 2010) (Wu, Shu et al. 2013).

Another part of work made in this thesis is about prostate segmentation on T2 MRI. We adapt the work in (Garnier, Bellanger et al. 2011) for US data to build an OSD based segmentation framework on T2 MRI. After the initialization of a prostate surface mesh and the construction of a graph, three kinds of weights are introduced to assign shape/boundary information to the graph. At last, the energy of graph is

minimized by graph cut algorithm. We have published this work in (Wu, Garnier et al. 2013). In order to improve the segmentation performance, we also build graphs on the bladder and the rectum, and segment them together. The prior information and constraints are encoded into the graphs in order to avoid the prostate surface leakage to the surrounding organ area.

The third part of our work is about TRUS-MR registration. We segment the prostate surface on TRUS and MR images based on our previous work. After a rigid registration to align prostate surfaces from TRUS and MR, an elastic registration based on Demons algorithm is used to warp MR surface to TRUS surface. The generated deformation field could be used to transfer 3D MR preoperative information into the peroperative TRUS volume.

Part II:

Region Based Information Characterization in Ultrasound Image

Chapter 3: Moment invariant based texture analysis

In intensity based registration, the main hypothesis is that a tissue is described by a specific intensity distribution. But in ultrasound images, tissues are characterized by their speckle spatial distribution with huge intensity variation. The main idea is to use a texture description method which is able to translate a specific speckle distribution into a constant value. This value can then be used in an intensity based similarity measurement metric like Mutual Information, etc.

In this chapter, moment invariant based texture descriptors are introduced to characterize the features of ultrasound images. These moment invariant based descriptors could extract texture features from ultrasound image which are invariant to rotation and scaling. This property could be used to compensate the impact of speckle shape rotation and size changing in the ultrasound images. Three kinds of moment invariants with different basis functions will be investigated in our work. First we will give the definitions and principles of invariant moments. The ability to extract a feature from the speckle distribution despite a change in scale and rotation will be evaluate on the Brodatz texture database, a simulated synthetic ultrasound image and a real ultrasound image. Beside this expected property, we have also noticed that the moment invariants based texture descriptors should be able to describe not only regional information but also the boundaries of the objects in texture image. This non expected property can be used in an ultrasound image segmentation scheme. We proved this possibility by combining these regional and boundary information in a graph cut scheme, and give an example of segmentation.

3.1 Texture analysis on ultrasound image

3.1.1 Ultrasound image

Ultrasound has a wide usage in clinical applications, not only as a primary investigation modality but also as a complement to other diagnostic procedures. The principle of ultrasound imaging is to send high frequency sound pulse into the body, then to record the echoes backscattered from the structures and tissues within the body, to process and to display them on the monitor in real time. Ultrasound imaging

plays an important role in the clinic due to its real-time imaging modality, non-ionizing radiation, and the ability of measuring and imaging the blood flow.
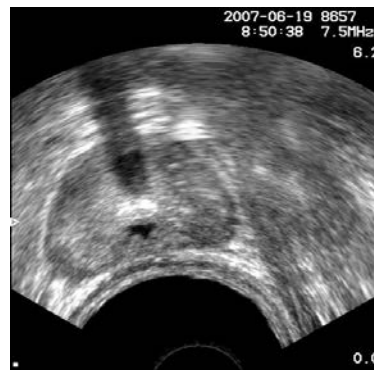

Fig 3.1 Ultrasound image

As a kind of coherent imaging, ultrasound imaging has an inherent characteristic that the tissues are described as a distribution of speckle. Speckle is a random, deterministic, interference pattern in the ultrasound image. It formed from the interferences between the reflected ultrasound beams from sub-resolution scatterers within a tissue. Speckle is usually considered as a negative impact on ultrasound imaging due to its reduction in contrast resolution. It is responsible for the poorer effective resolution of ultrasound compared to other medical images (CT, MRI, etc). But the sub-resolution scatterers (tissues cells, capillaries, blood cells, etc.) distribution is specific to a tissue. So the coherent summation of backscattered signals forms a spatial distribution of speckle that is specific to the density and distribution of the scatterers and thus to the nature of the tissue.

Several speckle spatial distribution models have been proposed in the literature according to the level of organization and the density of the scatterers within the tissues (Rayleigh-, Rician-, K-, Nakagami-distributions, etc). So the speckle has been used in several ways to characterize the tissues (Noble and Boukerroui 2006). Some authors tried to estimate the speckle distribution model by some statistics on the gray level intensities (i.e. (Seabra, Ciompi et al. 2011)), but this class of methods overlooks the spatial nature of the distribution. Treating the speckle distribution as a kind of texture, and processing ultrasound image by using texture analysis method could be a solution.

3.1.2 Texture analysis

Image texture is usually defined as a function of the spatial variation in pixel intensities. The analysis of texture can be useful in a variety of applications and has been a subject of intense study by many researchers, and one of them is the

recognition of image by using texture properties. In some cases, texture is the most important visual cue in identifying the several types of homogeneous regions.

Texture analysis has been traditionally used to characterize the spatial distribution of patterns. Beside studies who aimed at directly estimate the speckle distribution (Shankar 2004), the use of general texture analysis methods had some successes in ultrasound image segmentation (Noble and Boukerroui 2006). However, texture analysis needs relatively large windows to perform the features estimation, this leads to lack of precision, especially on the tissues boundaries. Other US image characteristics can also make the feature extraction more problematic. Because of the ultrasound beam form, the size (or scale) of the speckle increases according to the distance to the ultrasound probe (Fig. 3.1). For circular probes, the speckle also has a concentric organization, so a single speckle has an orientation depending on its position in the image (Fig. 3.1). In these cases, a texture analysis tool should be able to extract features which are invariant to both scale and orientation. Some attempts have been proposed using Gabor filters (Zhang, Tan et al. 2002, Han and Ma 2007).

In ultrasound image analysis, multi-scale and multi-orientation two-dimensional (2-D) Gabor filter banks (composed of six different orientations and two different scales) have been used to characterize the prostate boundaries and incorporate into a Kernel Support Vector machine for texture differentiation (Shen, Zhan et al. 2003, Zhan and Shen 2006). The likelihood obtained by this means is then used to drive a deformable surface model; however, this scheme is relatively complex because it needed a filter bank on one location. We will try to find a new texture indicator which is inherently invariant to rotation and scale which can characterize the speckle distribution in one pass. Moment based methods could be good candidates.

3.2 Moment invariant based texture analysis

Moment-based texture analysis has been introduced in the literature. The main idea of this method is the extraction of some features by computing a set of moments on regions of interests (ROIs) of the texture images (Fig 3.2). For example, low order geometric moments correspond to a geometric meaning of texture in the ROI such as mass, centroid and principal axes. Other classes of moments are not directly related to some specific properties of an image, but their abilities of texture characterization have been confirmed (Bigun and du Buf 1994), (Tuceryan 1994). In his pioneer work, Hu proposed to derive a set of seven 2-D moment invariants from the classical geometrical moments according to translation, rotation and scale (Hu 1962). Hu's moments have been widely used for pattern recognition, but could also be used for texture analysis.

Moments with orthogonal basis functions (e.g. Zernike or pseudo-Zernike polynomials) can represent an image by a set of mutually independent descriptors, and thus have a minimal amount of information redundancy. They were shown to have better image description capability and to be more robust to noise than geometric moments. In the past few years, the construction of orthogonal moment invariants with respect to geometric transformations such as translation, scale and rotation has been investigated (Chen, Shu et al. 2011) (Zhang, Dong et al. 2010) (Zhang, Shu et al. 2010). These moment invariants have been applied to pattern recognition. However, to our knowledge, no work has been performed using these moment invariants for the texture analysis. In this section, we will introduce three moment invariant descriptors. They all satisfy the requirement of ultrasound image texture analysis: invariant to rotation and scaling.
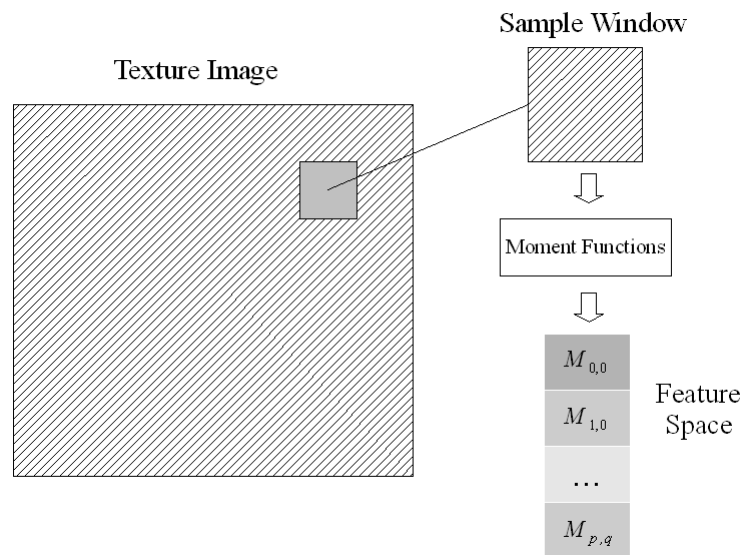
Fig 3.2 Moment based texture analysis

3.2.1 Orthogonal moments

In this section we will explore 3 classes of orthogonal complex moments Zernike, Pseudo-Zernike and Orthogonal Fourier-Mellin moment.

Zernike moments

The Zernike moment of order p with repetition q of $f(r,\theta)$ is defined as:

$$ZM_{p,q}^f = \frac{p+1}{\pi} \int_0^{2\pi} \int_0^1 R_{p,q}(r)e^{-jq\theta}f(r,\theta)rdrd\theta, \quad p \geq 0, \quad |q| \leq p, \quad p-|q| \quad being \quad even$$

(1)

where $R_{p,q}(r)$ is the real-valued radial polynomial given by

$$R_{p,q}(r) = \sum_{k=0}^{(p-|q|)/2} \frac{(-1)^k (p-k)!}{k! \left(\dfrac{p+|q|}{2} - k \right)! \left(\dfrac{p-|q|}{2} - k \right)!} r^{p-2k} \tag{2}$$

Pseudo-Zernike moments

The pseudo-Zernike moment of order p with repetition q of image intensity function $f(r,\theta)$ is defined as (Teh and Chin 1988):

$$PZM_{p,q}^{f} = \frac{p+1}{\pi} \int_0^{2\pi} \int_0^1 V_{p,q}^*(r,\theta) f(r,\theta) r\, dr\, d\theta, \quad p \geq 0, \ |q| \leq p \tag{3}$$

where $*$ denotes the complex conjugate, and $V_{p,q}(r,\theta)$ is the pseudo-Zernike polynomial of order p with repetition q given by:

$$V_{p,q}(r,\theta) = R_{p,q}(r) e^{jq\theta} \tag{4}$$

and the real-valued radial polynomial $R_{p,q}(r)$ is defined as

$$R_{p,q}(r) = \sum_{k=0}^{p-|q|} \frac{(-1)^k (2p+1-k)!}{k!(p+|q|+1-k)!(p-|q|-k)!} r^{p-k} \tag{5}$$

Orthogonal Fourier-Mellin moments

The Orthogonal Fourier-Mellin moment of order p with repetition q of an image intensity function $f(r,\theta)$ is defined as (Sheng and Shen 1994)

$$OFMM_{p,q}^{f} = \frac{p+1}{\pi} \int_0^{2\pi} \int_0^1 R_p(r) e^{-jq\theta} f(r,\theta) r\, dr\, d\theta, \quad p \geq 0, \ |q| \leq p \tag{6}$$

where $R_p(r)$ is a set of radial polynomials given by

$$R_p(r) = \sum_{k=0}^{p} \frac{(-1)^{p+k}(p+k+1)!}{k!(k+1)!(p-k)!} r^k \tag{7}$$

3.2.2 Orthogonal moment invariants

According to (Ghorbel, Derrode et al. 2006), the most important properties to be accessed by image descriptors are:

- Invariance against some geometrical transformations (translation, rotation, scaling);
- Stability to noise, to blur, to non-rigid and small local deformations;
- Completeness.

In the past decades, the construction of moment invariants and their application to pattern recognition have been extensively investigated (Li 1992) (Jin and Tianxu 2004) (Xu and Li 2008) (Chim, Kassim et al. 1999).

Complex moments are inherently invariant under image rotation, as an example with Zernike moments, when an image undergoes a rotation of angle α, the Zernike moments of the transformed image are given by $ZM_{p,q}^{f} \bullet e^{-jq\alpha}$. Thus, the magnitude of the Zernike moment, i.e. $\left| ZM_{p,q}^{f} \right|$, is invariant to rotation. This can be generalized to any complex moments. However, as indicated by Flusser (Flusser 2000), the magnitudes do not generate a complete set of invariants, and completeness is an important property for assessment of image descriptors. Additionally, our three original orthogonal moments are not invariant to image scaling. To solve this problem, the normalization process (Khotanzad and Hong 1990) is often used to achieve the scale invariance. Several moment invariants developed in (Chong, Raveendran et al. 2003) (Chong, Raveendran et al. 2004) (Zhu, Shu et al. 2007) with scale invariance perform better than the classical approaches. But all these moment invariants above do not have completeness property. In (Chen, Shu et al. 2011) (Zhang, Dong et al. 2010) (Zhang, Shu et al. 2010), the complete set of moment invariants are construct based on *ZMs*, *PZMs* and *OFMMs* (a proof of the invariance can be found in appendix A). These image descriptors not only are invariant to image rotation and scaling, but also have property of completeness. Theoretically, they could be good texture descriptors on ultrasound image.

Zernike moment invariants

A complete set of Zernike moment invariants (*ZMIs*) with respect to image rotation and scaling of order p and repetition q (where $p = q + 2m$ with $m \geq 0$) of an image intensity function $f(r, \theta)$ has been constructed as (Chen, Shu et al. 2011):

$$ZMI_{p=q+2m,q}^{f} = e^{-jq\theta_f} \sum_{k=0}^{m} \sum_{l=k}^{m} \Gamma_f^{-(q+2l+2)} c_{m,l}^{q} d_{l,k}^{q} ZM_{q+2k,q}^{f} \tag{8}$$

where ZM_{q+2k}^{f} is the original Zernike moment, $\theta_f = \arg\left(ZM_{1,1}^{f}\right)$, $\Gamma_f = \sqrt{ZM_{0,0}^{f}}$, $c_{m,l}^{q}$ and $d_{l,k}^{q}$ are given by:

$$c_{m,l}^{q} = (-1)^{m-l} \frac{q+2m+1}{\pi} \frac{(q+m+l)!}{l!(m-l)!(q+l)!} \tag{9}$$

$$d_{l,k}^{q} = \pi \frac{l!(q+l)!}{(l-k)!(q+l+k+1)!} \tag{10}$$

Pseudo-Zernike moment invariants

A complete set of pseudo-Zernike moment invariants (*PZMIs*) with respect to rotation and scaling of order p and repetition q (where $p = q + m$ with $m \geq 0$) has been constructed as (Zhang, Dong et al. 2010):

$$PZMI_{p=q+m,q}^{f} = e^{-jq\theta_f} \sum_{k=0}^{m} \sum_{l=k}^{m} \Gamma_f^{-(q+l+2)} c_{m,l}^{q} d_{l,k}^{q} PZM_{q+k,q}^{f} \tag{11}$$

where PZM_{q+k}^{f} is the original pseudo-Zernike moment, $\theta_f = \arg\left(PZM_{1,1}^{f}\right)$, $\Gamma_f = \sqrt{PZM_{0,0}^{f}}$, $c_{m,l}^{q}$ and $d_{l,k}^{q}$ are given by

$$c_{m,l}^{q} = (-1)^{m-l} \frac{q+m+1}{\pi} \frac{(2q+m+1+l)!}{l!(m-l)!(2q+1+l)!} \tag{12}$$

$$d_{l,k}^{q} = 2\pi \frac{l!(2q+l+1)!}{(l-k)!(2q+l+k+2)!} \tag{13}$$

Orthogonal Fourier-Mellin moment invariants

A complete set of Orthogonal Fourier-Mellin moment invariants (*OFMMIs*) with respect to rotation and scaling of order p and repetition q of an image intensity function $f(r,\theta)$ has been constructed as (Zhang, Shu et al. 2010)

$$OFMMI_{p,q}^{f} = e^{-jq\theta_f} \sum_{k=0}^{p} \frac{p+1}{k+1} \left(\sum_{l=k}^{p} \Gamma_f^{-(l+2)} c_{p,l} d_{l,k} \right) OFMM_{k,q}^{f} \tag{14}$$

where $OFMM_{k,q}^{f}$ is the original Orthogonal Fourier-Mellin moment. $\theta_f = \arg\left(OFMM_{1,1}^{f}\right)$, $\Gamma_f = \sqrt{OFMM_{0,0}^{f}}$, $c_{p,l}$ and $d_{l,k}$ are given by:

$$c_{p,l} = (-1)^{p+l} \frac{(p+l+1)!}{l!(p-l)!(l+1)!} \tag{15}$$

$$d_{l,k} = (2k+2) \frac{l!(l+1)!}{(l-k)!(l+k+2)!} \tag{16}$$

3.2.3 Evaluation of the invariance properties of the moments

The invariance of moment invariants have been proved theoretically (see Appendix). Equation (48) of Appendix shows that the complete sets of moment invariants are linear combinations of their original moments. These moment invariants could offer a feature space equivalent to the feature space extract by the original moment functions, but also with some new properties useful for texture analysis. In this section, we will evaluate their texture rotation and scaling invariance abilities on different materials.
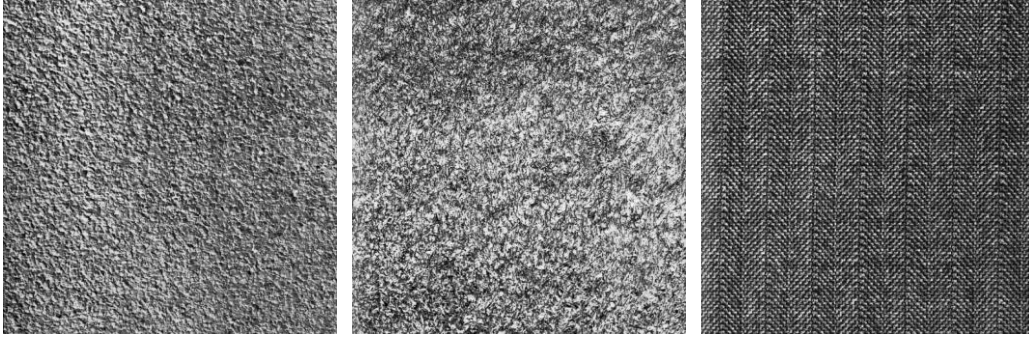
Fig 3.3 Texture images from Brodatz database, from left to right:
D4, D9 and D17 (http://www.ux.uis.no/~tranden/brodatz.html)

We choose the D4, D9 and D17 images from the Brodatz database to evaluate the texture analysis: the first two types offer some random distributed texture, and the last type contains a kind of orientation change (rotation). The size of texture image is 512×512.

In order to prove the rotation invariance property, these texture images are rotated by different angles (0, 45, 90, 135, 180, 225, 270, 315 degrees). Then, 40 sample windows with a 31×31 size are randomly chosen on each rotated image for the moment feature computation. At the end, we take the mean value of the 40 computed features for comparison.

We applied using the framework dispayed in in Fig 3.2 all the three moment classical moments (*ZMs*, *PZMs*, *OFMMs*) and the three moments invariants (*ZMIs*, *PZMIs*, *OFMMIs*) with the same order and repetition Because the moments, are complex number, we used the moments magnitude (the modulus) as the texture feature.

In Fig 3.4, we compare the features estimated using $\left|ZMI_{2,0}\right|$, $\left|PZMI_{3,0}\right|$, $\left|OFMMI_{2,0}\right|$ and $\left|OFMMI_{2,2}\right|$ to their related original moment functions ($\left|ZM_{20}\right|$, $\left|PZM_{3,0}\right|$, $\left|OFMM_{2,0}\right|$, $\left|OFMM_{2,2}\right|$). The result shows that, with the same orders and repetitions, the features estimated by the moment invariants are more stable than these by the original moment functions, .This studies shows also that although the magnitude would ensure the rotation invariance of the original moment, this has not been totally verified in the tests.
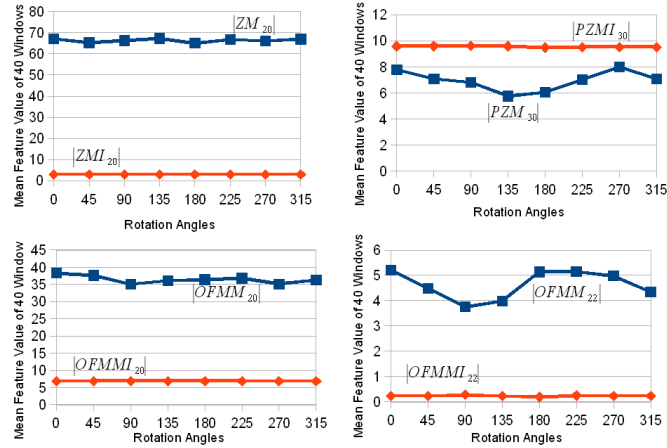
Fig 3.4.1: Rotation invariance evaluation on D4 texture. The red line represents the moment invariant features and the blue line represents the original moment features. Top left: $\left|ZM_{2,0}\right|$ and $\left|ZMI_{2,0}\right|$, top right: $\left|PZM_{3,0}\right|$ and $\left|PZMI_{3,0}\right|$, bottom left: $\left|OFMM_{2,0}\right|$ and $\left|OFMMI_{2,0}\right|$, bottom right: $\left|OFMM_{2,2}\right|$ and $\left|OFMMI_{2,2}\right|$

Fig 3.4.2: Rotation invariance evaluation on D9 texture. The red line represents the moment invariant features and the blue line represents the original moment features. Top left: $\left|ZM_{2,0}\right|$ and $\left|ZMI_{2,0}\right|$, top right: $\left|PZM_{3,0}\right|$ and $\left|PZMI_{3,0}\right|$, bottom left: $\left|OFMM_{2,0}\right|$ and $\left|OFMMI_{2,0}\right|$, bottom right: $\left|OFMM_{2,2}\right|$ and $\left|OFMMI_{2,2}\right|$
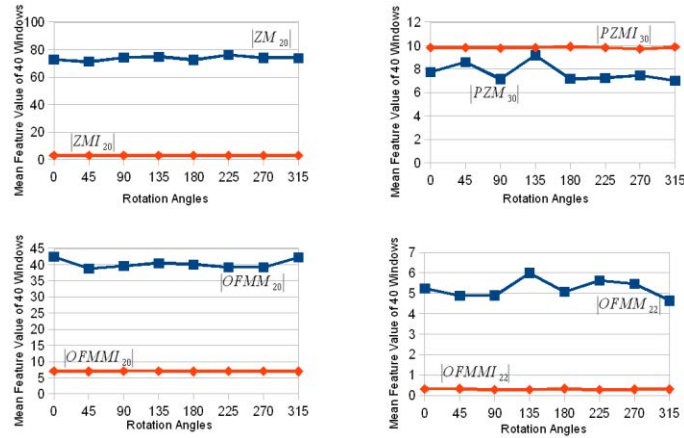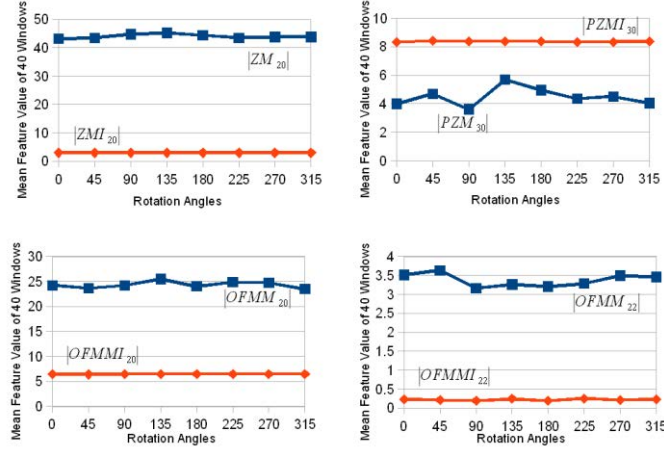
Fig 3.4.3: Rotation invariance evaluation on D17 texture. The red line represents the moment invariant features and the blue line represents the original moment features. Top left: $\left|ZM_{20}\right|$ and $\left|ZMI_{20}\right|$, top right: $\left|PZM_{3,0}\right|$ and $\left|PZMI_{3,0}\right|$, bottom left: $\left|OFMM_{2,0}\right|$ and $\left|OFMMI_{2,0}\right|$, bottom right: $\left|OFMM_{2,2}\right|$ and $\left|OFMMI_{2,2}\right|$

A similar test is made to evaluate the scaling invariance (Fig 3.5). We zoomed the Brodatz texture images by several scaling ratio r: ($1/2$, $3/4$, 1, $5/4$, $3/2$, $7/4$, 2). For each scaled image, 40 sample windows (31×31) are randomly chosen for the moments features estimation. It should be noticed that the sample window size is not changed. So inside a sample window, not only the texture size is scaled, but the content itself also has changes. This is not a strict image scaling situation, but the scaling invariant property will be helpful to keep the texture feature consistency.

Fig 3.5.1: Scaling invariance evaluation on D4 texture. The red line represents the moment invariant features and the blue line represent the original moment features Top left: $\left|ZM_{20}\right|$ and $\left|ZMI_{20}\right|$, top right: $\left|PZM_{3,0}\right|$ and $\left|PZMI_{3,0}\right|$, bottom left: $\left|OFMM_{2,0}\right|$ and $\left|OFMMI_{2,0}\right|$, bottom right: $\left|OFMM_{2,2}\right|$ and $\left|OFMMI_{2,2}\right|$

Fig 3.5.2: Scaling invariance evaluation on D9 texture. The red line represents the moment invariant features and the blue line represent the original moment features. Top left: $\left|ZM_{20}\right|$ and $\left|ZMI_{20}\right|$, top right: $\left|PZM_{3,0}\right|$ and $\left|PZMI_{3,0}\right|$, bottom left: $\left|OFMM_{2,0}\right|$ and $\left|OFMMI_{2,0}\right|$, bottom right: $\left|OFMM_{2,2}\right|$ and $\left|OFMMI_{2,2}\right|$
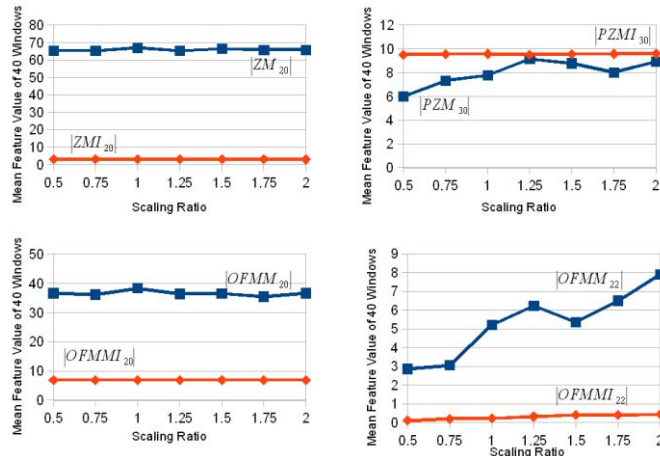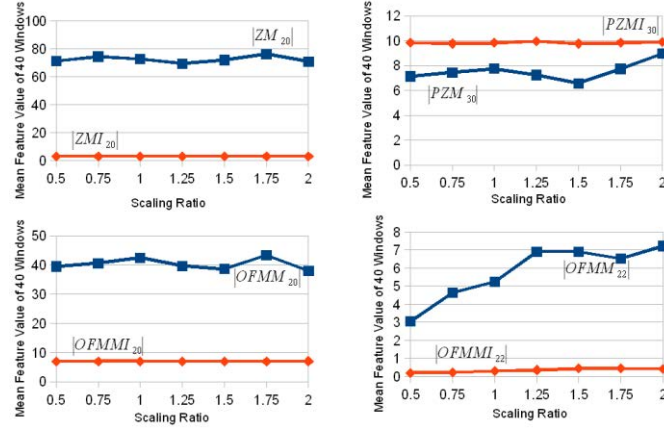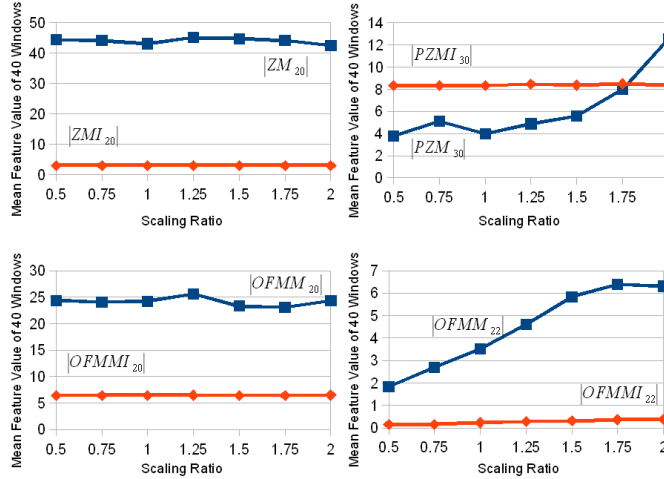

Fig 3.5.3: Scaling invariance evaluation on D17 texture. The red line represents the moment invariant features and the blue line represent the original moment features. Top left: $\left|ZM_{20}\right|$ and $\left|ZMI_{20}\right|$, top right: $\left|PZM_{3,0}\right|$ and $\left|PZMI_{3,0}\right|$, bottom left: $\left|OFMM_{2,0}\right|$ and $\left|OFMMI_{2,0}\right|$, bottom right: $\left|OFMM_{2,2}\right|$ and $\left|OFMMI_{2,2}\right|$

We also give the comparison between moment invariants and the original moment functions. The result shows that, the moment invariants based texture features are more stable in the texture scaling context.

With this series of tests on Brodatz texture images, we found that moment invariants not only can extract texture features, but also are invariant to texture rotation and scaling. The results of these tests indicate that the moment invariants could be a good texture descriptor on ultrasound images. In the following sections, we will try to extract the texture features on simulated and real ultrasound images by using moment invariants, and test the properties of these features.

3.2.4 Evaluation of the invariance properties for texture estimation

In order to evaluate the performance of these moment invariants to extract the speckle distribution feature, we used 2 kind of images: a simulated synthetic ultrasound image and a real transrectal ultrasound image.

- The simulated image is composed by an elliptical shaped region within a background region. The ultrasound simulation is performed by the method described in (Dillenseger, Laguitton et al. 2009). This method predicts the appearance and properties of a B-Scan ultrasound image from acoustical impedances and spatial distributions of point scatterers. In our case, each region is characterized by a specific acoustical impedance and a random spatial distribution of scatterers with a specific probability distribution. The parameters defined in (Dillenseger, Laguitton et al. 2009) for fat and liver were used to differentiate the 2 regions. This scatterers model serves as input for the simulation of an ultrasound image acquired by a circular ultrasound 3.5 MHz probe (Fig 3.6 a). In this image the gray scale values depends only on the scatterer's spatial distribution. The image size is 512×512 with a 0.6 mm pixel size .
- The real data is a transrectal prostate ultrasound (TRUS) image acquired intra-operatively on an Ablatherm device (Fig. 3.6 b). The transrectal ultrasound imaging probe is operating at 7.5 MHz. A slice has 500×490 pixels with a transverse pixel size of 0.154 mm/pixel and a thickness of 2 mm.

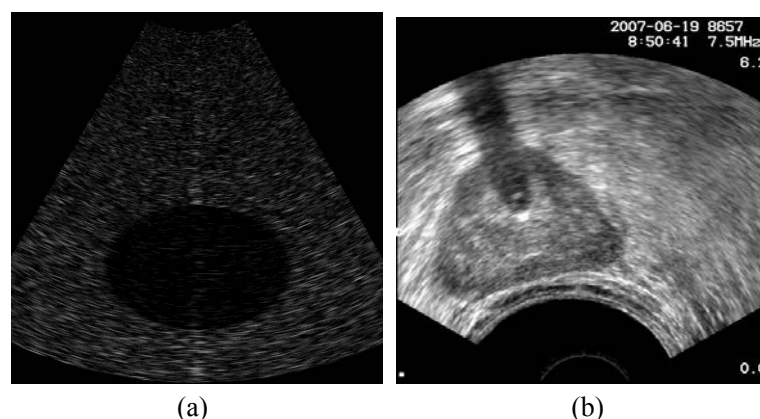(a)   (b)

Fig 3.6 (a) Simulated image (b) Real ultrasound image

As we mentioned before, the speckle orientation and scale depends on its location in the beam. So if the speckle distribution is constant for a same object, the individual speckle patterns have different orientation and size. This situation could be

approximated as texture rotation and scaling.

In order to evaluate the invariance properties for texture estimation, we choose randomly 40 sample windows on respectively the background and object (resp. outside and inside the elliptical region for the simulated image; resp. outside and inside the prostate for the real ultrasound image). Moment invariants and original moment functions are computed on the 40 sample windows (31×31) as we did before. The textures of these sample windows have different orientations and speckle sizes. Comparisons between the moment invariants and the original moments can be seen in Fig 3.7 for the simulated ultrasound image and in Fig 3.8 for the real TRUS image:
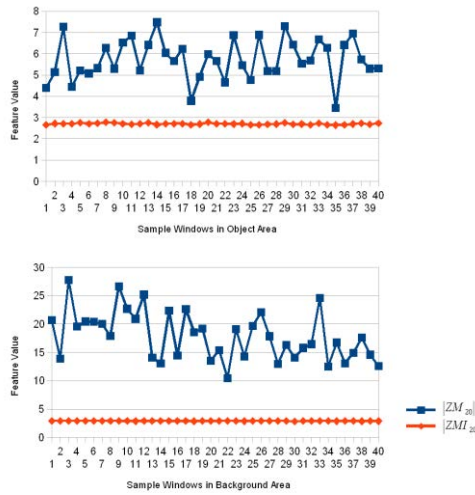
Fig 3.7.1 Features from $\left|ZM_{2,0}\right|$ and $\left|ZMI_{2,0}\right|$ on the simulated image. The red line represents the moment invariant features and the blue line represents the original moment features. The graph on the top shows the features in the object area, and the graph on the bottom the features in the background area.

Fig 3.7.2 Features from $\left|PZM_{3,0}\right|$ and $\left|PZMI_{3,0}\right|$ on the simulated image. The red line represents the moment invariant features and the blue line represents the original moment features. The graph on the top shows the features in the object area, and the graph on the bottom the features in the background area.

Fig 3.7.3 Features from $\left|OFMM_{2,0}\right|$ and $\left|OFMMI_{2,0}\right|$ on the simulated image. The red line represents the moment invariant features and the blue line represents the original moment features. The graph on the top shows the features in the object area, and the graph on the bottom the features in the background area.
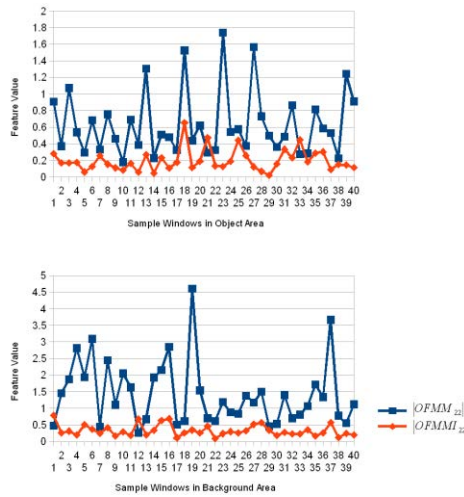
Fig 3.7.4 Features from $\left|OFMM_{2,2}\right|$ and $\left|OFMMI_{2,2}\right|$ on the simulated image. The red line represents the moment invariant features and the blue line represents the original moment features. The graph on the top shows the features in the object area, and the graph on the bottom the features in the background area.
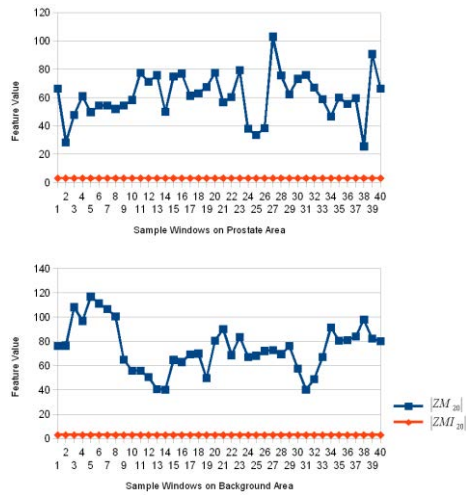
Fig 3.8.1 Features from $\left|ZM_{20}\right|$ and $\left|ZMI_{20}\right|$ on the real image. The red line represents the moment invariant features and the blue line represents the original moment features. The graph on the top shows the features in the object area, and the graph on the bottom the features in the background area.
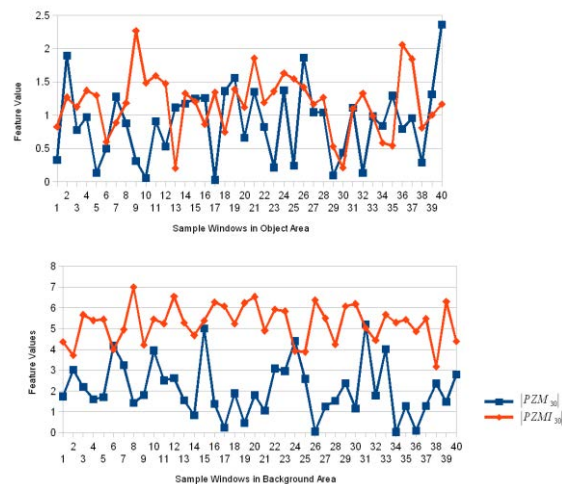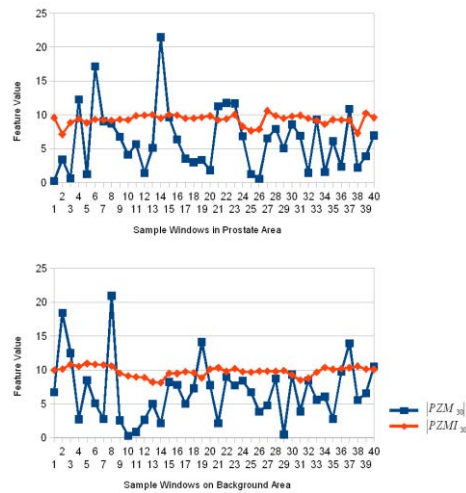

Fig 3.8.2 Features from $\left|PZM_{3,0}\right|$ and $\left|PZMI_{3,0}\right|$ on the real image. The red line represents the moment invariant features and the blue line represents the original moment features. The graph on the top shows the features in the object area, and the graph on the bottom the features in the background area.
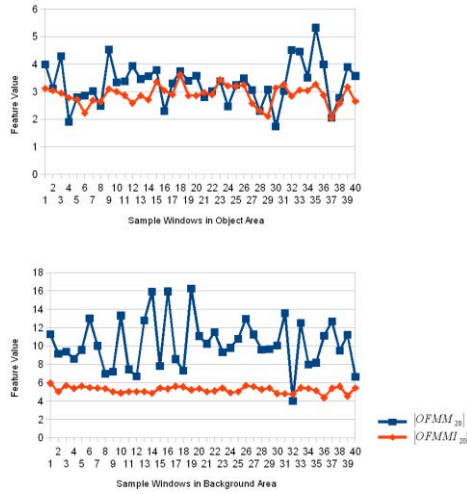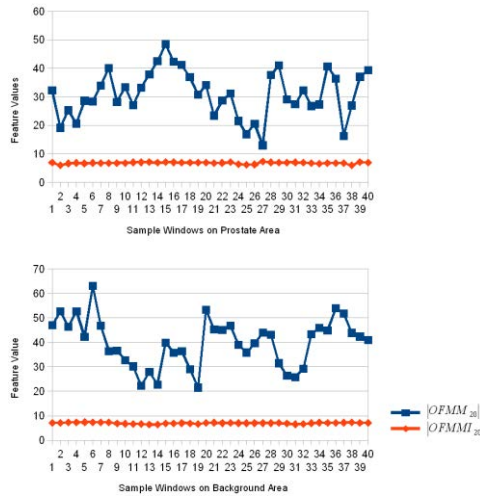
Fig 3.8.3 Features from $\left|OFMM_{2,0}\right|$ and $\left|OFMMI_{2,0}\right|$ on the real image. The red line represents the moment invariant features and the blue line represents the original moment features. The graph on the top shows the features in the object area, and the graph on the bottom the features in the background area.

Fig 3.8.4 Features from $\left|OFMM_{2,2}\right|$ and $\left|OFMMI_{2,2}\right|$ on the real image. The red line represents the moment invariant features and the blue line represents the original moment features. The graph on the top shows the features in the object area, and the graph on the bottom the features in the background area.
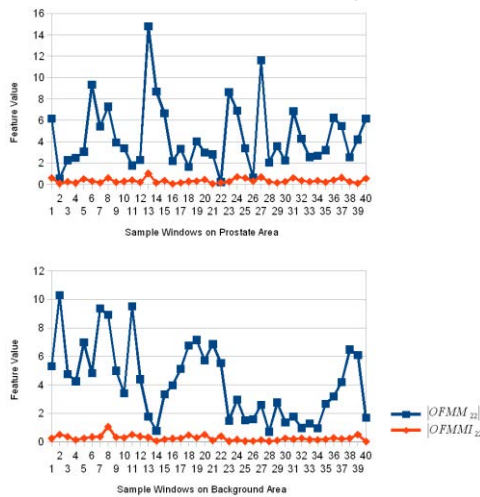
The standard deviation of the different texture feature values measured in all the 40 sample windows are listed in Tab 3.1:

Texture Descriptor	Standard deviation on the simulated image		Standard deviation on the real ultrasound image	
	Object area	Background area	Prostate area	Background area
$\lvert ZM_{2,0} \rvert$	0.9478	4.2589	16.0500	19.5321
$\lvert ZMI_{2,0} \rvert$	0.0351	0.0231	0.0086	0.0068
$\lvert PZM_{3,0} \rvert$	0.5525	1.3114	4.6808	4.5361
$\lvert PZMI_{3,0} \rvert$	0.4512	0.8959	0.7589	0.7033
$\lvert OFMM_{2,0} \rvert$	0.7605	2.7072	8.1953	9.8076
$\lvert OFMMI_{2,0} \rvert$	0.3455	0.3384	0.2798	0.2527
$\lvert OFMM_{2,2} \rvert$	0.3898	0.9620	3.0755	2.6430
$\lvert OFMMI_{2,2} \rvert$	0.1305	0.1708	0.2111	0.1914

Tab 3.1 The standard deviation of different texture feature values

In the simulated ultrasound image case, the moment invariants based feature values are more constant than these estimated using the original moments. Even for the worst case here, the *PZMIs* (Fig 3.7.2), the standard deviation shows better performance than *PZMs* (Tab 3.1).

In the case of real image, the performance to extract stable features decreased because of the non-uniform distribution of texture, This is especially true for the original moments based features. But the moment invariants based features are less affected by this situation and show higher ability to characterize the ultrasound texture

The invariance properties can also be noticed on Fig 3.9. The classical moments are clearly affected by the speckle while the invariants remain mainly constant in the areas sharing a same speckle distribution.
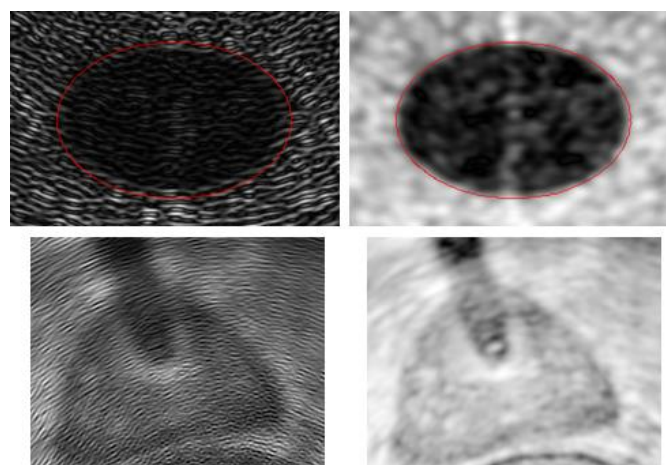

Fig 3.9 $\lvert PZM_{3,0} \rvert$ (left) and $\lvert PZMI_{3,0} \rvert$ (right) features on the simulated image (top) and real image (bottom)

The moment invariants can therefore serve as an indicator of an area sharing a same distribution of speckle. The moment invariants applied to an ultrasound image can be directly integrated into an intensity based similarity measure (Mutual Information, etc.).

3.3 Moment invariants based texture segmentation

3.3.1 Moment window size

Although the moment invariants are scale independent, the window size is an important parameter for any texture feature extraction method. Classically, in texture characterization methods a good windows size must be choosen in order to ensure a good compromise between detection capability and accuracy.

In order to expose the impact of the window size in the texture feature estimation, we make a test on 40 randomly chosen sample windows on the background area of the simulated ultrasound image (Fig 3.10 a). We calculate the moment invariant value of $\left| PZMI_{2,0} \right|$ on these windows, and then we estimate from these windows the features mean value and standard deviation. This work is repeated on different window size from 5×5 to 41×41. The result is shown in Fig 3.10 b. Two facts can be noticed: when the window size is too low (less than 23×23 in our case), the moment invariant values are less uniform distributed in the same texture area (high standard deviation); when the window size is high enough (more than 23×23 in our case), the moment invariant values have an uniform distribution in the same texture area. It is probably because the small window can not contain enough information to describe the speckle distribution, and when the window size is high enough, the duplicate speckles have little contribution to texture features.

The blurring on the transition zone between 2 areas with different texture distributions has been estimated on another test. In the simulated ultrasound image we choose several sample windows along a line going from background area to the object area (Fig 3.11 a). We calculate $\left| PZMI_{2,0} \right|$ on these sample windows along the line. This test will be repeated with different window sizes to estimate its impact on the texture boundary areas. The result shows that, when the window size is too large, the accuracy of boundary information will decrease (Fig 3.11 b).
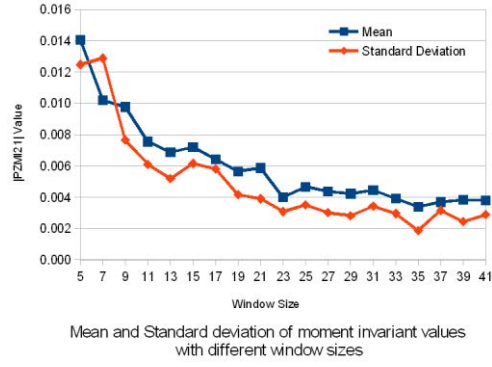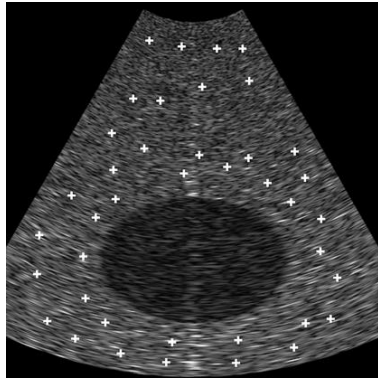
(a)   (b)

Fig 3.10 (a) Position of the 40 randomly sample windows on the
background area of the simulated ultrasound image. The white cross
labeled the center points of these sample windows. (b) The mean

and standard deviation of the 40 $\left|PZMI_{2,0}\right|$ values with different

window sizes from 5×5 to 41×41.
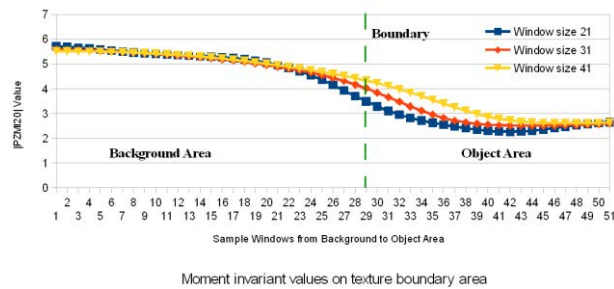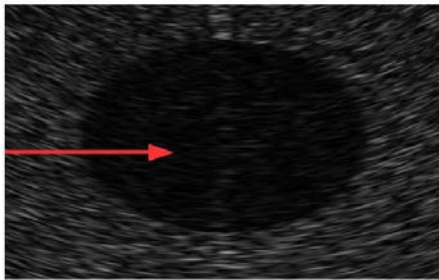
(a)   (b)

Fig 3.11 (a) Location of the sample window center points along the
red line from background area to object area. (b) The $\left|PZMI_{2,0}\right|$
values on these sample windows with different sizes

A compromise must be found between a large window size to capture the feature
and a small window size to accurately locate the information. In our case we think
that the window size should be related to the spatial size of the texture.

We choose to illustrate the impact of the window size on the estimation of the
$\left|PZMI_{2,1}\right|$ feature in the simulated image. This feature presents some fine structures
which will be directly impacted by the window size. In this image, the speckle
longitudinal size was about 20 pixels. Fig 3.12 shows the $\left|PZMI_{2,1}\right|$ feature
computed with window sizes of 11×11, 21×21 and 31×31. It can be clearly notified
that the feature homogeneity increases with the window size but at the expense of the
thinness of the features. In this case, the 21×21 window seemed to be a good
compromise between the homogeneity of the features and the accuracy to extract

some image components. This window size will be used in the rest of this chapter. This behavior was confirmed for the other moment feature measurements.
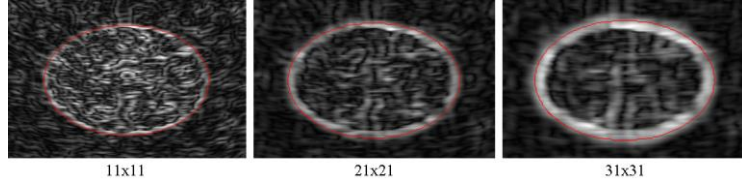
Fig 3.12 $\left|PZMI_{2,1}\right|$ values estimated with 11×11, 21×21 and 31×31 window size. In this figure only a rectangular window around the elliptic region of the simulated image is shown. The elliptic region boundary is shown in red.

3.3.2 Order and repetition characteristics

The behavior of the moment invariants according to the order and the repetition parameter has been evaluated on the simulated image (Fig 3.6 a).

The order p itself has a relatively low influence on the final result. As an example, Fig 3.13 shows the resulting images for $\left|PZMI_{p,0}\right|$ with p increasing from 1 to 3. We can observe that the images are relatively similar. Maybe the images seems to be a bit more irregular for higher orders but the details like then contours are more well defined.
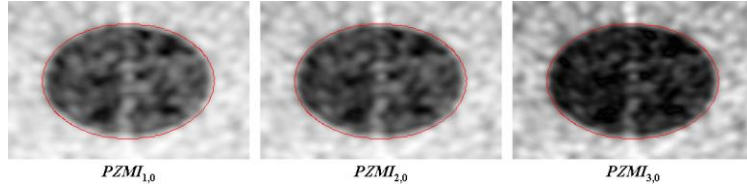
Fig 3.13 Influence of the order p. $\left|PZMI_{p,0}\right|$ with p increasing from 1 to 3.

The repetition q impacts directly the resulting features extracted by the moments. Fig 3.14 shows a selection of extracted features from several kinds of moment invariants at several order p and repetition q. We can notice on this figure that all the 3 classes of moment invariants that:
- for $q = 0$, the moments are sensitive to the regional distribution of texture information
- for $q = 1$, the moments are sensitive to the rupture between two textures (Fig 3.6 center) and can be similar to a "gradient of texture"
- for $q = 2$, the moments can be seen as a "Laplacian of texture".
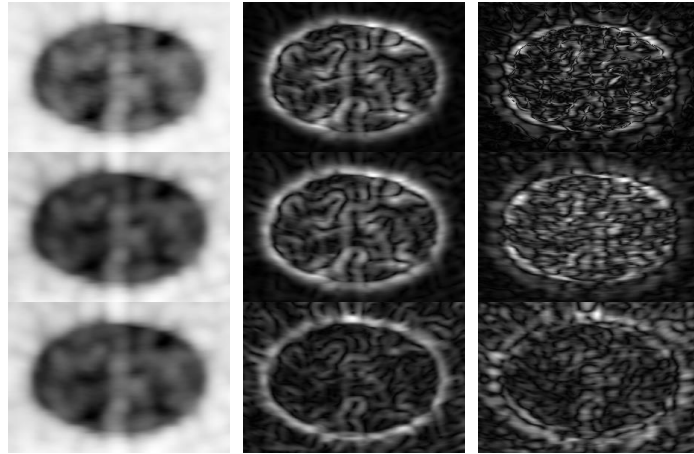
Fig 3.14 Texture features of simulated image. The first row, from left to right: $\left|ZMI_{2,0}\right|$, $\left|ZMI_{3,1}\right|$ and $\left|ZMI_{2,2}\right|$; the second row, from left to right: $\left|PZMI_{2,0}\right|$, $\left|PZMI_{2,1}\right|$, $\left|PZMI_{2,2}\right|$; the third row, from left to right: $\left|OFMMI_{1,0}\right|$, $\left|OFMMI_{0,1}\right|$, $\left|OFMMI_{1,2}\right|$

This regional and boundaries extraction behavior can also be seen on the features estimated from the real transrectal prostate ultrasound data (Fig 3.15). On this figure, the features extracted using the pseudo-Zernike moment invariants are also more homogeneous than those obtained using the classical moments.

$PZM_{3,0}$ $PZM_{2,1}$
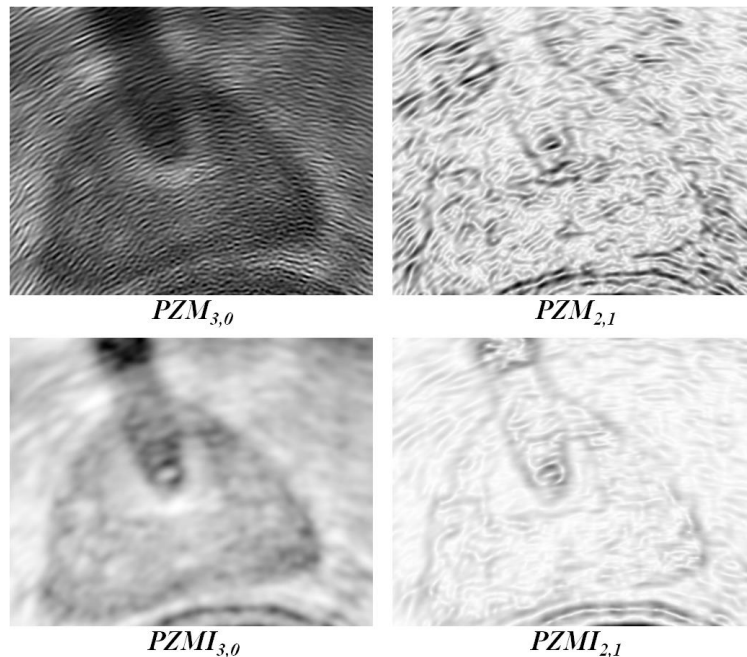
$PZMI_{3,0}$ $PZMI_{2,1}$

Fig 3.15 Features extracted on the transrectal prostate ultrasound image. Top left: $\left|PZM_{3,0}\right|$; top right: $\left|PZM_{2,1}\right|$; bottom left: $\left|PZMI_{3,0}\right|$; bottom right: $\left|PZMI_{2,1}\right|$

In texture analysis, a set of texture features (moments and others) are usually measured on the image, and a classification process is then performed in order to

characterize the objects of interest. However, as the moment-invariant features with repetition $q=0$ provide regional information and those with $q=1$ provide information on the boundaries of a textured region, this allows us to use the texture features differently. In many segmentation techniques, boundary information alone or in combination with regional information is needed, i.e. active contours, deformable models, level sets, etc. Some of these techniques have been adapted to deal with ultrasound images and require boundary information (e.g. (Chen, Lu et al. 2000) where some Gabor based invariants where used to constraint snake models). Our two kinds of moment-invariant features ($q=0$ regional information and $q=1$ boundary information) could be directly used in such a segmentation scheme dealing with ultrasound images.

3.3.3 Graph cut

In order to prove the previous assessment, without loss of generality, we will use the two kinds of moment-invariant features in a min-cut/max-flow graph cut algorithm. So we will show how the features extracted by orthogonal moments can be directly used in a combined region and boundary based segmentation algorithm and how the boundary information can improve the segmentation. However, the goal of this section is neither to evaluate finely the impact of the several parameters used in the graph-cut segmentation nor to compare its performance to other techniques.

The min-cut/max-flow graph cut algorithm popularized by Boykov is able to handle regional and boundary information (Boykov and Funka-Lea 2006). This graph partitioning approach is well adapted to an image binary classification issue. The segmentation problematic is described by a directional flow graph. The link topology and the initial weight assigned to these links are representative of an energy function to minimize. In our case, the segmentation problematic is formulated by the following energy function:

$$E_T = E_{classify} + \lambda \cdot E_{continuity} \qquad (17)$$

where $E_{classify}$ is an energy coding the probability that a pixel belongs to the class "object" or "background", and $E_{continuity}$ is an energy coding the degree of similarity or discontinuity between two neighboring pixels. The coefficient λ controls the balance between these two energy terms.

In the classical min-cut/max-flow graph cut algorithm the energy terms are encoded within the graph as link's weights estimated from the pixels values (Boykov and Funka-Lea 2006), (Esneault, Hraiech et al. 2007). For validating the usability of the moment invariants, we adapted a variant of the min-cut/max-flow graph cut algorithm

presented in (Esneault, Hraiech et al. 2007) in order to use the regional information features (with repetition $q=0$) to encode $E_{classify}$ and the boundaries information features (with $q=1$) to directly encode $E_{continuity}$ (Fig 3.16).
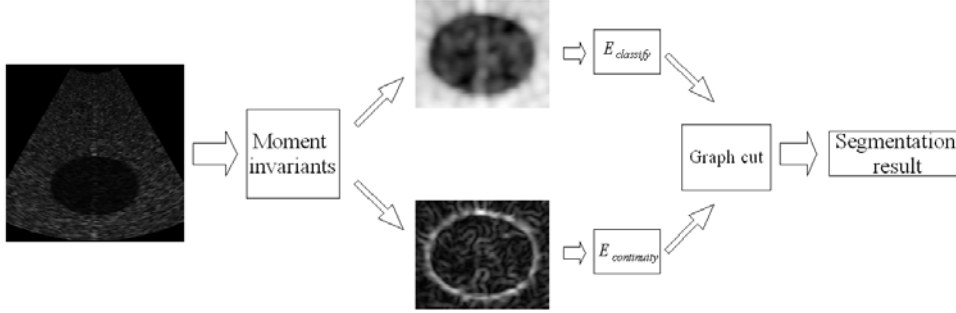
Fig 3.16 Graph cut segmentation scheme

As an example of this method, we will take the case with *ZMI* features. In this method, the user labels interactively some pixels as "object" and others as "background" (e.g. Fig. 3.17 a). The normalized histogram of these pixels in $|ZMI_{p,0}|$ is used to define the probability density function P_{object} (resp. P_{backg}). For a pixel u, the weights $\{u,S\}$ (resp. $\{u,T\}$)[5] associated with the regional energy $E_{classify}$ can be seen in Tab 3.2. $E_{continuity}$ is encoded on the links between two adjacent pixels $\{u,v\}$. This weight should be high between two neighboring pixels within the same region and low on boundaries. We can notice that this it is the opposite of the $|ZMI_{p,1}|$ image (see Fig 3.14). So, we first normalized and inverted $|ZMI_{p,1}|$ to obtain the image $|ZMI'_{p,1}|$ which is representative of the continuity between neighboring pixels (values close to 0 on boundaries, 1 on pixels within a same region). The weight between $\{u,v\}$ is then given by (see Tab 3.2):

$$\frac{\left|ZMI'_{p,1}(u)\right|+\left|ZMI'_{p,1}(v)\right|}{2}$$

The initial weights of the individual graph links are assigned to the graph according to Table 3.2. Once the graph is built, min-cut/max-flow graph cut algorithm is performed in order to segment the object (Boykov and Kolmogorov 2004).

---

[5] *S* and *T* are the two terminal nodes associated with the labels "object" and "background" respectively, see Boykov, Y. and G. Funka-Lea (2006). "Graph cuts and efficient ND image segmentation." International journal of computer vision **70**(2): 109-131.

.

links	weights	condition
$\{u,v\}$	$\lambda \cdot \dfrac{\left|ZMI'_{p,1}(u)\right| + \left|ZMI'_{p,1}(v)\right|}{2}$	for $\{u,v\} \in N$
$\{u,S\}$	∞	for u labeled as "object"
	$P_{object}\left(\left\|ZMI_{p,0}(u)\right\|\right)$	for the other u
$\{u,T\}$	∞	for u labeled as "background"
	$P_{backg}\left(\left\|ZMI_{p,0}(u)\right\|\right)$	for the other u

Tab 3.2 Initial weights for the graph cut segmentation
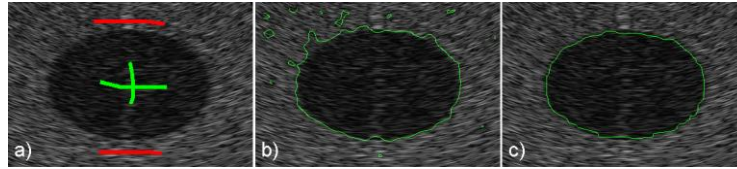
Fig 3.17 Graph cut segmentation results. a) Graph cut seed points (green: "object", red: "background"). The estimated boundaries using *ZMI* features with: b) $\lambda = 0$, with only the regional information, and c) $\lambda = 1$, with a mixture of region and boundary information.

We performed the evaluation for the Hu's moment invariants and the three orthogonal moment invariants on the simulated ultrasound image (Fig 3.6 a). Some small areas of pixels were interactively selected in both the object and background regions (Fig 3.17 a). These areas were used as seed points for the segmentation and also serve as training basis for the $E_{classify}$ related initial weight assignment. After the graph cut segmentation, the extracted region was compared with the real elliptically-shaped region. Each pixel could be classified as true positive (with *TP* the number of true positives), false positive (resp. *FP*), true negative (resp. *TN*) or false negative (resp. *FN*). The performance of our segmentation scheme is presented as:

Fractional Area Difference: $\left(\dfrac{FP-FN}{TP+FN}\right)$,

Sensitivity: $\left(\dfrac{TP}{TP+FN}\right)$,

Accuracy: $\left(\dfrac{TP-FP}{TP+FN}\right)$.

The crucial points of our method are: the choice of the features used to encode the region and boundary information, and the balance coefficient λ.

After some exploratory work we noticed that the more accurate results were obtained by using relatively high order moments for the regional information $\left|Hu_{1}\right|$, $\left|ZMI_{2,0}\right|$, $\left|PZMI_{3,0}\right|$ and $\left|OFMMI_{3,0}\right|$, and for the regional information $\left|Hu_{2}\right|$, $\left|ZMI_{1,1}\right|$, $\left|PZMI_{2,1}\right|$ and $\left|OFMMI_{2,1}\right|$. These features can be seen in Fig 3.18 and are consistent with the remarks made in the previous section about more well defined details for higher moment orders.
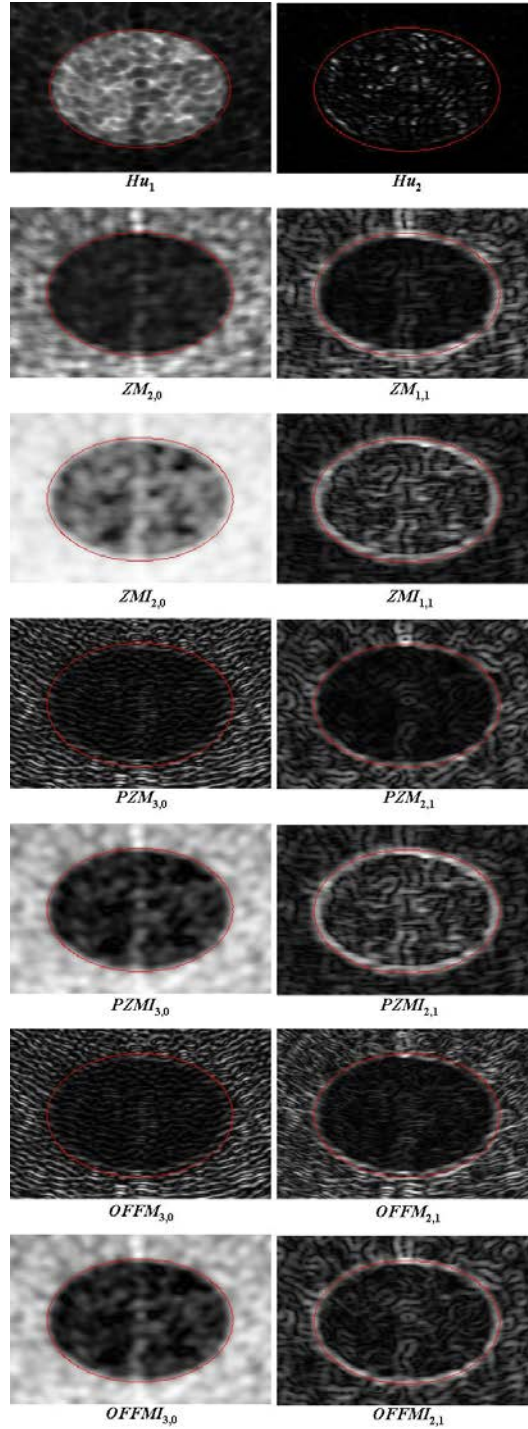
Fig 3.18 Regional and boundary features of simulated ultrasound image

The λ parameter setting was trickier because its influence is not linear and is data dependent. First, in an exploratory study, we interactively tuned λ to analyze its influence. We noticed that, even with a relatively small λ, the continuity term was taken into account within the segmentation. Then, for a relatively large range of variation in λ, the segmentation results remained almost the same, with only some

small changes on the boundaries. Finally, for very high values of λ (over 100) the segmentation accuracy decreased. Fig 3.17 shows the impact of the variation of λ. The presented segmentation results were obtained using the *ZMI* set. For $\lambda = 0$, we only had the influence of the regional information of $\left| ZMI_{2,0} \right|$ (Fig 3.17 b). With $\lambda = 1$, the boundary information of $\left| ZMI_{1,1} \right|$ was mixed with the regional information in order to delineate the region with a higher accuracy (Fig 3.17 c).

Tab 3.3 compares the performance between the segmentation results of the min-cut/maxflow graph cut algorithm with $\lambda = 1$, using methods based on Hu, Zernike, pseudo-Zernike and orthogonal Fourier-Mellin moment invariants and the equivalent classical moments. In all cases (except one), moment invariants gave better results than the classical moments. The classical *PZM* and *OFMM* totally failed to extract the elliptic region because their behavior was too inhomogeneous. Surprisingly, the classical *ZM* gave very good results. Even though its standard deviation was not as good than that of *ZMI* (see Tab 3.1), the contrast (the mean values difference) between the 2 regions in $\left| ZM_{2,0} \right|$ was much higher than in $\left| ZMI_{2,0} \right|$ allowing good regional information. If we compare the results obtained using the four moment-invariant sets we can see that *OFMMI* showed a slightly better performance in the case of the simulated data.

	Fract area diff	Sensitivity	Accuracy
Hu	-7.8%	91.81%	91.42%
ZM	-4.63%	95.0%	94.63%
ZMI	-6.42%	93.47%	93.36%
PZM	-90.87%	9.13%	9.13%
PZMI	-4.22%	95.33%	94.88%
OFMM	-90.83%	9.17%	9.17%
OFMMI	-2.35%	96.99%	96.33%

Tab 3.3 Comparisons of moments-based texture segmentation on
simulated image

We applied our method to the real transrectal prostate image (Fig 3.6 b). In this data, the speckle within and outside the prostate was more heterogeneous than that in the simulated US. Moreover, a urethral catheter was placed to protect the urethra from injury during HIFU ablation, and this catheter projected the classical ultrasonic shadow. However we expected to be able to overcome this problem by interactively setting some well adapted seed points (Fig. 3.19 a). The input images were the same moment features (same order and repetition) as for the simulated data. However, we changed the window size to 11×11 to adjust it to the transrectal prostate speckle dimension. Fig 3.19 compare the segmentation results of the min-cut/max-flow graph

cut algorithm with $\lambda = 1$, using the different moment sets. Because of the non-homogeneity of the speckle within the prostate, all the segmentation results show some gaps within the extracted region. However, two facts can be observed from Fig 3.19. First, the classical moment sets were less efficient than the invariant moment sets for describing the prostate, mainly because they were less capable of expressing the regional information. This was especially true for *PZM* and *OFMM* that have failed to close the boundary of the prostate. Second, it can be seen that the orthogonal moment-invariant sets provided smoother boundaries than the classical sets, probably because they estimated more homogeneous features. Nevertheless it is difficult to significantly compare the different classes of moments on only the graph cut because the final segmentation result is directly dependent on user interaction (variables seed points and λ value). However, in all the cases the segmentation was easier to tune with the orthogonal moment-invariant sets than with the other sets.
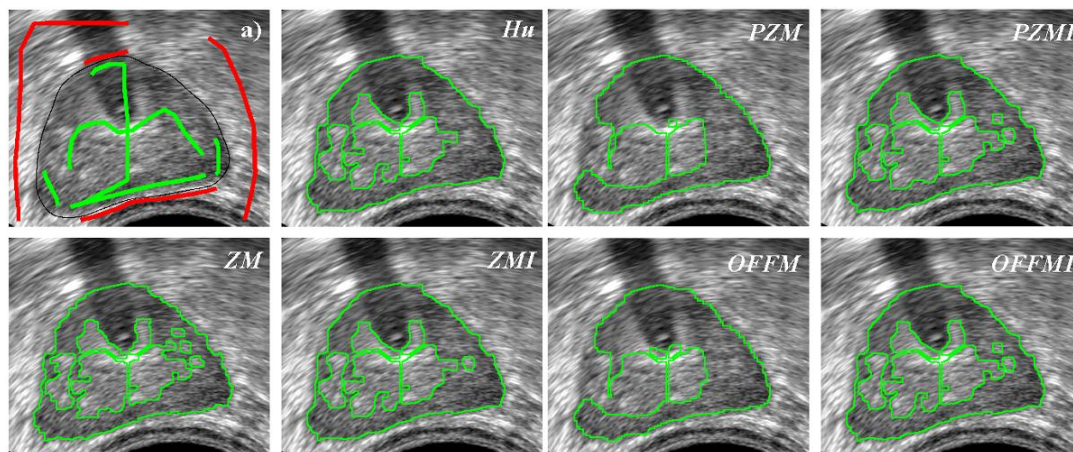
Fig 3.19: Transrectal prostate ultrasound image segmentation. a) the seed points (green: "object", red: "background") and (in black) the contour drawn by an expert. Others: segmentation results.

In conclusion, the purpose of this section was only to demonstrate that the region and boundary information obtained by moment-invariant sets on ultrasound image can be directly used in a classical segmentation method. Within the min-cut/max flow graph-cut framework, moments invariants showed their ability to extract texture information from the ultrasound image. Moreover the fact that moment invariants were able to extract boundary information clearly improved the segmentation results.

3.4 Conclusion

In this chapter, we presented three sets of orthogonal moment invariants that can be used to extract texture features when the texture pattern has a concentric organization or when its scale changes in the image, like the speckle in ultrasound images, for example. The moment invariant features extracted on a simulated circular ultrasound image demonstrated that they are able to extract the global distribution of the speckle and that they are little sensitive to speckle orientation or scale changes. This proved that moment invariants especially with repetition q=0, can be used as feature information in an intensity based similarity measure like Mutual Information, etc.

The results also showed that some features were sensitive to regional texture information and others enhanced the boundaries between two textured regions. The features sensitive to the boundaries between two textured regions can be seen as texture "gradient" and can thus be used in segmentation techniques where the boundary information is needed, i.e. active contours, deformable models, level sets, etc. In order to demonstrate the usability of moment-invariant features, such as region and boundary information, we introduced this joint information into the min-cut/max-flow graph cut algorithm. The resulting segmentations on simulated and real ultrasound images demonstrated the benefits of the joint region- and boundary-sensitive moment-invariant texture features. Moment invariants are so eligible to be used to adapt techniques based on the combination on regional and boundary information to the segmentation of ultrasound images.

Considering our intensity-based registration scheme, we have demonstrated that the moment invariants applied on ultrasound images can be directly used in a similarity measure between the 2 modalities. However, when we tried to include the information (directly the intensities or using the moment invariant) of the T2 MRI in the registration scheme, we get no significant results. This is probably due to the fact that in T2 MRI the prostate is heterogeneous in values (several zone, etc., see chapter 2) and also that some prostatic zone share some common intensity distribution with some neighbor tissues.

We decide then to give up the intensity based registration framework and redirect our work on an alternate surface-based registration scheme.

Part III:

Surface-Based Registration

Chapter 4： OSD based prostate segmentation on T2 MRI

Automatic/semiautomatic prostate segmentation scheme is playing an important role in prostate cancer treatment (eg. diagnosis and treatment planning). For now, 3D Prostate segmentation on T2 MRI is still a challenging task. It is not only because the prostate organ is a soft tissue which usually present a large variation in both shape and size, but also because the prostate is surrounded by other organs (eg. bladder and rectum) which have similar intensity information as the prostate boundary on T2 MRI, even worse, these organs may have serious mutual influence together (Freedman, Radke et al. 2005, Vu and Manjunath 2008) (Song, Liu et al. 2010). In this chapter, an Optimal Surface Detection (OSD) based method is introduced to segment the prostate from T2 MRI. This segmentation scheme uses information of local intensity changes around the prostate surface, and also considers the influence of the surrounding organs. The segmented prostate surface could be used in a surface-to-surface registration scheme between the ultrasound image and the MRI.

4.1 OSD based prostate segmentation

The OSD based segmentation has been originally introduced in (Li, Wu et al. 2004), and has been applied to prostate segmentation on ultrasound images in (Garnier, Bellanger et al. 2011). The main idea of the OSD is to consider the segmentation problem as the computation of a minimum s-t cut in an oriented weighted graph, which is build from the voxels surrounding the surface of an initial mesh and from 2 auxiliary nodes s and t (source and sink respectively) (Li, Wu et al. 2004). The whole OSD scheme contains several steps: mesh initialization, graph construction, weight assignation and graph cut. In following sections, we will give the detailed workflow of the OSD based prostate segmentation on T2 MRI.

4.1.1 Initialization

In order to convert the segmentation problem into a graph cut problem, an oriented weighted graph should be build from the voxels around the object surface. It means that a first surface of the object is needed as an initial state. The initialization method is introduced in (Hu, Downey et al. 2003). Six manual points are positioned

on the prostate surface: 4 of them $\left(p_0^{init}, p_1^{init}, p_2^{init}, p_3^{init}\right)$ are located on the central section, and the remaining 2 points $\left(p_4^{init}, p_5^{int}\right)$ are set at the base and the apex of the prostate.
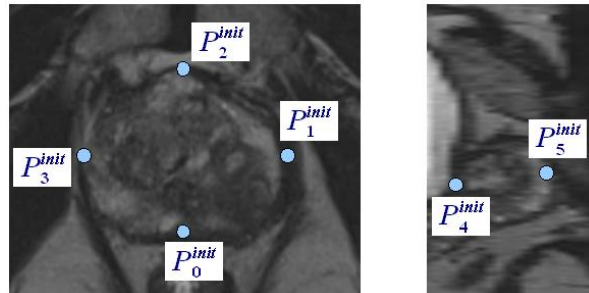
Fig 4.1 Six initial points manually set on the prostate surface. Four
on the central section, one on the base, and the other on the apex.

An ellipsoid mesh, describing the surface of prostate, is generated from the 6 initial points:

$$p_k^{init}\left(x_k, y_k, z_k\right), k = 0, \cdots, 5. \tag{18}$$

The ellipsoid center point $C\left(x_c, y_c, z_c\right)$ and its half axeses s_x, s_y, s_z are defined by:

$$
\begin{aligned}
x_c &= \frac{x_1 + x_3}{2}, & s_x &= \frac{x_1 - x_3}{2}, \\
y_c &= \frac{y_0 + y_2}{2}, & s_y &= \frac{y_2 - y_0}{2}, \\
x_c &= \frac{z_4 + z_5}{2}, & s_z &= \frac{z_5 - z_4}{2}.
\end{aligned}
\tag{19}
$$

The ellipsoid is sampled by longitudes and latitudes angles in order to form a parametric space (a, b):

$$F(\theta, \varphi) \rightarrow F(a, b) \tag{20}$$

The ellipsoid surface defined before, goes not exactly through the six initial points, and sometimes, it can be relatively far from the prostate edge. A 3D transformation by Biharmonic Spline ("Linear Spline") (Bookstein 1989) is used to deform the mesh in direction of the initial points and still maintaining a smooth surface shape (Garnier 2009).

This method finally provides a prostate-liked shape mesh (Fig 4.2). Even if the vertexes of the mesh can be still distant to the real prostate surface, this mesh will be considered as the initial surface. OSD will refine the surface near this initial mesh.
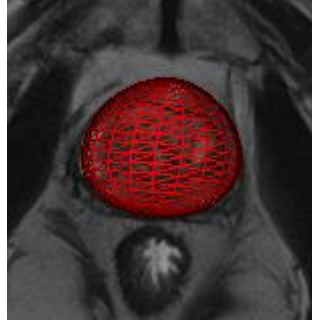
Fig 4.2 Initial surface mesh of prostate

4.1.2 Graph construction

An oriented graph composed by nodes and weighted links is constructed based on the initial mesh, and also defines the relations between the neighboring voxels.

(a) (b) (c)
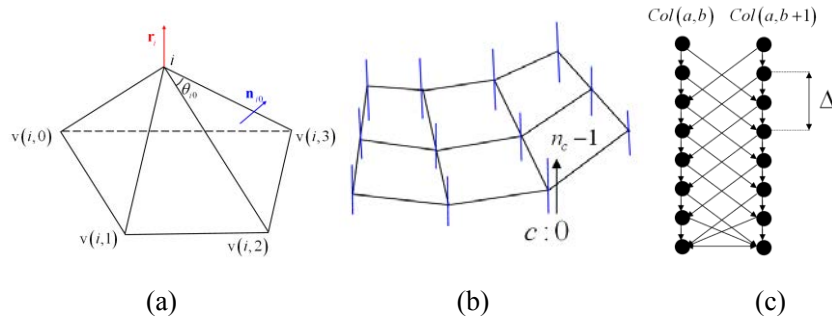
Fig 4.3 Graph construction on prostate: (a) vertex normal definition, (b) nodes columns build on each vertex, (c) inter- and intra-column link definition

The graph is composed by some specific nodes connected by weighted links. We will now develop the graph construction detailing the role of the several nodes and links.

Nodes

According to Boykov's formalism two kinds of nodes are used: object nodes and terminal nodes.

- Objects nodes:

The main idea of OSD is to refine the surface position near the initial surface. For this, we will define a search zone near all the vertexes of the initial surface. In order to constraint the searching zone, we choose to estimate the refined surface position along the normal at each vertex of the initial mesh (Fig 4.3 b). For each vertex $i = (a,b)$ of the mesh, we build a column of nodes. A column $Col(i)$ (or $Col(a,b)$) consist of n_c nodes $N(i,c)$, each of the nodes corresponding to a

value $V\left(x_{ic}, y_{ic}, z_{ic}\right)$ estimated by the closest surrounding voxel value along the normal $\mathbf{R}_i$ (Fig 4.3 c).

The calculation of the normal $\mathbf{R}_i$ is described in (Ghanei, Soltanian-Zadeh et al. 1998). The normal $\mathbf{R}_i$ at the vertex i is the sum of the weighted unit normal from the neighboring facets. The weights correspond to the apex angle of the facet (Fig 4.3 a) and take into account the specific contributions from the different facets.

$$\mathbf{R}_i = \frac{1}{\theta_i} \sum_{k=0}^{M-1} \theta_{i,k} \mathbf{n}_{i,k} \tag{21}$$

here $\theta_i = \sum_{k=0}^{M-1} \theta_{i,k}$, and $\theta_{i,k} = \cos^{-1}\left(\mathbf{e}_{i,k}, \mathbf{e}_{i,k+1}\right)$, $\mathbf{e}_{i,k}$ is an unit vector from vertex $v(i,k)$ to vertex i.

The normal vector of each facet is obtained by the cross product of two of its edges:

$$\mathbf{n}_{i,k} = \frac{\mathbf{e}_{i,k} \wedge \mathbf{e}_{i,k+1}}{\left\|\mathbf{e}_{i,k} \wedge \mathbf{e}_{i,k+1}\right\|} \tag{22}$$

Finally, the outward directed vector $\mathbf{r}_i$, is constructed by normalization:

$$\mathbf{r}_i = \frac{\mathbf{R}_i}{\left\|\mathbf{R}_i\right\|} \tag{23}$$

The future surface will be defined on this node topology. On each column, the refinement process will find the nodes which have the highest probability to be on the surface. The pointed nodes on two adjacent columns will form an edge of the refined surface.

- Terminal nodes:

    2 specific nodes, the source terminal node s and the sink terminal node t, are also inserted into the graph. s is usually associate to the object to segment (the "surface" in our case) and t to the background ("no surface").

Links

The links will encode the information about the data and the relationship between the data. Globally, they are 2 types of links: the t-links (t for terminal) which will links each object nodes to the 2 terminal nodes and the n-links (n for neighbor) which links together 2 objects nodes. The t-links will encode the data term information and the n-links some neighborhood or spatial information between 2 nodes.

- *n-links:*

    This kind of links will define the neighborhood information between nodes (i.e the nodes belonging to a same column) but also some constraint on the

surface continuity or smoothness. Three kinds of *n*-links are added in this work:

1) Column links:

A set of oriented links of infinite weight is created by connecting the nodes in the same column (Fig 4.3 c).

$$\langle N(i,c), N(i,c-1)\rangle, \qquad c > 0 \tag{24}$$

This links ensure that a surface crosses the column of nodes on only one node.

2) Surface links:

This set of infinitive weight provides the connection between 2 adjacent columns:

$$\langle N(i,c), N(j, \max(0, c-\Delta))\rangle, \qquad j \in N_i \tag{25}$$

where N_j is the neighbor of i (Fig 4.3 c). Because the initial mesh is a closed surface, the nodes of index $b = 0$ are also included in their neighborhood index $b = n_b - 1$, and vice versa.

Δ of equation (25) is the hard shape constraint which keeps the surface smooth. The smaller Δ is, the smoother optimal surface will be. Because the distances between two adjacent vertices are not regular over the initial surface, Δ has been adapted according to this distance (in voxel):

$$\Delta_{ij, j\in N_i} = floor\left(\delta \|p_i - p_j\|\right) \tag{26}$$

where p_i and p_j are the positions of vertex i and j, δ is a constant, and *floor* take the integer part of result. This hard shape constraint ensures that a surface can only move from a distance less than Δ from one column to another.

3) Shape constraint links:

A shape constraint (shape-prior penalty) can be added to penalize the shape changes between two neighboring columns (Song, Liu et al. 2010). Additional inter-column links are added between $N(i,c)$ and $N(j, c+h)$, and $h = \Delta_{j,i} + 1, \Delta_{j,i} + 2, \cdots, \Delta_{i,j} - 1$. These links are assigned with a weight equal to the second derivate of a convex function $f(h) = \beta h^2$.

- *t*-links

A link will be set between the terminal source node *s* and each object node. The weight of this links will encode the energy (or probability) that attached an

object node to the "surface" class.

Respectively, a link will also be set between each object node and the terminal sink node t. The weight of this links will encode the energy (or probability) that attached an object node to the "not surface" class.

In our case, for each node $N(i,c)$ of the graph we will first assign a weight $w(i,c)$, which is defined by:

$$w(i,c) = \begin{cases} C(i,c) & if \quad c = 0 \\ C(i,c) - C(i,c-1) & otherwise \end{cases} \qquad (27)$$

here C is the cost function, and it is related to the probability that the node belongs to the target surface.

According to the sign of the nodes weight $w(i,c)$, a weight $|w(i,c)|$ is assigned on the links from s to the node if $w(i,c) < 0$, or on the links from the node to t if $w(i,c) \geq 0$.

Several cost function will be discussed in section 4.1.3. However, a particular cost is assigned to the nodes on the 6 initial points in order to take the practitioner expertise into account. In our case, we used a very high negative cost:

$$C = -1000 \cdot I_{max} \qquad (28)$$

here I_{max} is the maximum value of image. This weight cost forces the surface to go through these initial nodes.

4.1.3 Graph cut

With the previous weighted graph, the position of the future surface will be estimated from the weights assigned on the t-links (the energy or probability that a node belongs to the "surface" and "non surface" class) and from the topology of the surface links (parameter α) and shape constraint links (parameter β). In our case, the optimal surface is obtained with the min-cut/max-flow algorithm (Boykov and Kolmogorov 2004).

After the graph cut, one node of each nodes column will be assigned as surface point. These surface points are the new vertexes of the refined surface mesh.
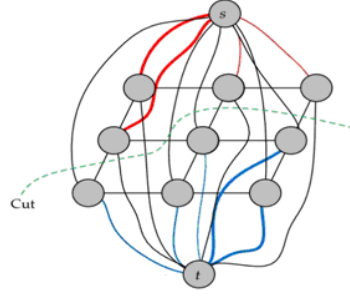
Fig 4.4 The cut of the weighted graph will assign some nodes to belong to the "surface" class

4.1.4 Data term weight assignment.

The key point of the OSD algorithm is the cost function. Three different classes of cost functions have been tested based on different information and models:

Image-based feature: gradients

The image-based surface energy is based on the smoothed gradient of image I :

$$E\left(x,y,z\right)=\left\|\nabla\left(G_{\sigma}*I\left(x,y,z\right)\right)\right\|=\left\|\mathbf{G}\left(x,y,z\right)\right\| \qquad (29)$$

with G_{σ} is a Gaussian filter with standard deviation σ .

Three cost functions, only based on the energy of the current node location, have been tested:

- POS_GDT: Promoting the positive gradients from low to high value transitions, that means the same direction as the surface normal.

$$C_{i,c}=-\left\|\mathbf{G}\left(x_{i,c},y_{i,c},z_{i,c}\right)\right\|\frac{s_{i,c}+1}{2} \qquad (30)$$

$$\text{with } s_{i,c}=\frac{\mathbf{G}\left(x_{i,c},y_{i,c},z_{i,c}\right)\cdot\mathbf{N}_{i}}{\left\|\mathbf{G}\left(x_{i,c},y_{i,c},z_{i,c}\right)\right\|}$$

- NEG_GDT: Promoting negative gradients:

$$C_{i,c}=-\left\|\mathbf{G}\left(x_{i,c},y_{i,c},z_{i,c}\right)\right\|\frac{\left|s_{i,c}-1\right|}{2} \qquad (31)$$

- ALL_GDT: Promoting any directions:

$$C_{i,c}=-\left\|\mathbf{G}\left(x_{i,c},y_{i,c},z_{i,c}\right)\right\| \qquad (32)$$

Shape probability model

A cost function based on a shape probability is build based on a shape probability map. This map is build by the following steps:

1) With a set of 3D T2 MRI volumes as training data, the urologist labeled the prostate contours manually on each case. On these volumes, the prostate surfaces are constructed based on these manual contours.

2) A local prostate based reference system is defined on each prostate volume as Fig 4.5:
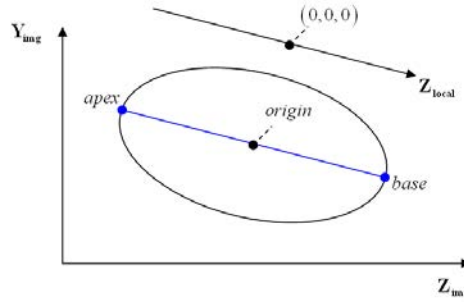
Fig 4.5 The definition of local coordinate system

The first axis is aligned from the apex to the base, the reference origin is set as the middle of the apex-base segment, and the other two axes are adjusted to the prostate surface. These expert surfaces are regularly resampled within their local reference systems in order to form a regular mesh.

3) The meshes of all the surfaces of the training set are aligned using the generalized procustes algorithm (Gower 1975) implemented in VTK. On one hand, this algorithm gives the average shape of all the training data, and on the other hand, all the individual forms aligned on the average shape.

4) A 3D distance map d is built for each training shape, and then it is converted to Gaussian distance map g by:

$$g = \exp\left(-\frac{d^2}{2\sigma_m^2}\right) \tag{33}$$

with σ_m a constant. The shape probability map is finally built by averaging the Gaussian maps of all the aligned shapes (Fig 4.6).

For the segmentation of a new T2 MRI volume, first we align the model average shape onto the initial mesh of the data to be segmented by using the generalized procrustes algorithm (Gower 1975). The estimated rigid transformation matrix

(translation, rotation and scaling) are then applied on the probability map in order to align it on the MRI data to segment (Fig 4.6).
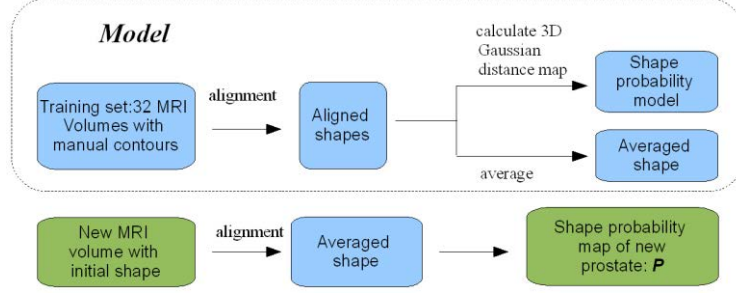
Fig 4.6 cost function constructed based on shape probability model

The shape probability based cost function $C_p(i,c)$ at node $N(i,c)$ is then defined as:

$$C_p(i,c) = P(i,c) * C_g(i,c) \tag{34}$$

here $P(i,c)$ is the probability map, $C_g(i,c)$ is gradient based cost defined in the previous section.

Gradient profile model

The gradient profile model is inspired by the work of Cootes (Cootes and Taylor 2001). The idea is to build a statistical model of the gradient profiles variation from a learning set and then use this model to assign some costs.

The gradient profile model is build from the training set as following steps:

1) As described in the previous section, we align together all the training set surfaces.

2) We resampled regularly all the aligned surface in order to share the same sampling topology for each surface. We are so able to define corresponding points between all the shapes.

3) The gradient profile model is built as described in (Cootes and Taylor 2001): From K training surfaces each sampled on N vertexes, a gradient profile g_{ij} is estimated at each sample i ($i = 1,\ldots,N$) on each training surface j ($j = 1,\ldots,K$). Each gradient profile g_{ij} consists in the gradients (see Equation(29)) estimated at 10 locations on both sides of the surface (Fig 4.7). At each sample i we can construct $\mathbf{g}_i$, a profile of vectors of gradients (a vector is composed by the K gradients computed at the same location on all the K surfaces). For simplicity the profile of vectors of gradients will be called profile vector. The vector $\mathbf{g}_i$ is then be normalized as:

85

$$\mathbf{g}_i \rightarrow \frac{1}{\sum_j \left| g_{ij} \right|} \mathbf{g}_i . \tag{35}$$

If we assume that all the profiles are distributed as a multivariate Gaussian, the appearance on one sample can be modeled by the mean profile $\hat{g}_i$ and the covariance matrix $\mathbf{S_{gi}}$. The quality of the fit of a new profile g_{si} to the model can be estimated by the Mahalanobis distance:

$$f\left(g_{si}\right) = \left(g_{si} - \hat{g}_i\right)^T \mathbf{S_{gi}}^{-1} \left(g_{si} - \hat{g}_i\right) \tag{36}$$

To perform the segmentation of a new volume, the initial mesh of this volume is aligned on its local prostate based reference system (Fig 4.5) and resampled in order to ensure correspondence to the model vertices. It should be notice that, the a-priori information brought by the 6 initial points is lost in this configuration.

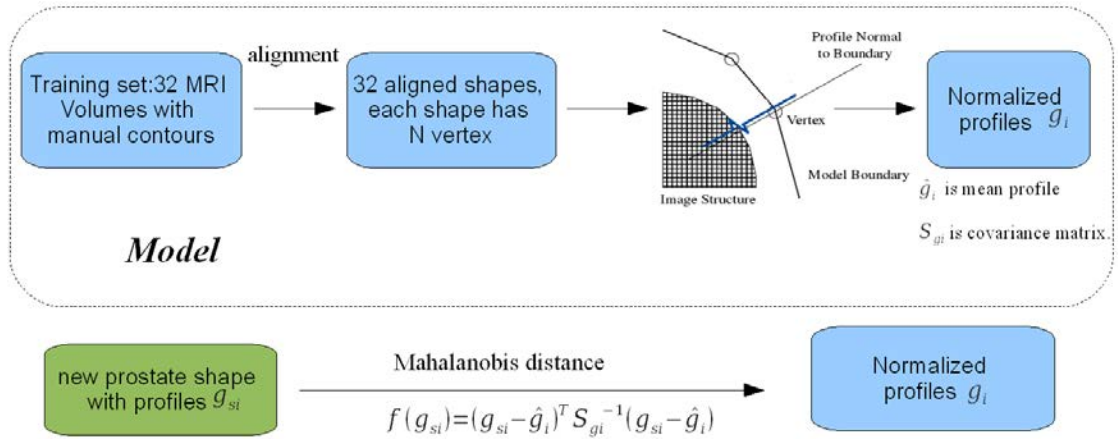**Fig 4.7** cost function constructed based on gradients profile model

The gradients profiles $g_{i,c}$ are computed at the location of all the nodes $N(i,c)$ of the graph. The node cost value is then defined as:

$$C_{i,c} = f\left(g_{i,c}\right) - \max\left(f\left(g_s\right)\right) \tag{37}$$

where $\max\left(f\left(g_s\right)\right)$ is the maximum Mahalanobis distance over all the computed profiles in the current image.

4.1.5 Parameters adjustment

As we mentioned previously, 33 T2 axial MRI volumes are used in our work. These MRI volumes are acquired from 5 different devices with different qualities and image sizes (Tab 4.1). In this section, a series of tests are made on these data and in order to find the parameters which can give the best segmentation performance.

MRI system	Number	Size (voxel)	s_a (mm)	s_t (mm)
3T Philips Achieva	10	$720 \times 720 \times 20$	0.416	4.001
3T Siemsens Vero	5	$320 \times 320 \times 20$	0.625	3.600
1.5T Siemens Magnetom Symphony	16	$256 \times 256 \times 24$	0.781	3.000
3T Philips Achieva	1	$352 \times 352 \times 24$	0.540	2.630
GE Signa HDxt	1	$512 \times 512 \times 16$	0.391	4.500

Tab 4.1 The parameters of T2 MRI training set

We get manual contours for all the 33 T2 MRI volumes so they can be used as test database. For the segmentation of one volume, the values and the contours of the other 32 cases are used as training set to get the average shape and shape probability map, or the gradient profiles model.

The following parameters are tuned sequentially in our work:
- δ : the hard shape constraint from inter-column links
- σ : the Gaussian filter standard deviation
- POS_GDT, NEG_GDT and ALL_GDT: the promoted gradient directions in the gradient-based cost function
- InD and OutD: The search distances inside and outside of surface

For all the database of MRI volumes, we tuned separately each parameter and evaluated the performance of the segmentation scheme with the Volume Overlap metric:

$$VO = \frac{V_M \cap V_A}{V_M \cup V_A} \tag{38}$$

with V_M and V_A respectively the expert (manual) and the OSD (automatic) segmented volume. The *mean* in % and the standard deviation (*std*) of all the 33 VOs serve as global performance metrics. For a specific parameter, the value which gives the best performance is kept for the next parameter tuning.

With $\sigma = 1$, InD $= -20$, OutD $= 20$ and the gradient search direction to ALL_GDT, δ is tested from 1/4 to 1. The best performance is obtained with $\delta = $ 1/2, which will be used as hard shape constraint.

δ	1/4	1/3	1/2	2/3	3/4	1
mean (%)	72.73	75.62	76.90	75.05	73.79	68.29
std	7.06	6.38	5.72	5.11	4.81	6.64

Tab 4.2 choice of hard shape constraint δ

With the fixed InD $= -20$, OutD $= 20$ and the gradient search direction to ALL_GDT, σ is tested from 0 to 5. The best performance is obtained with $\sigma = 1$.

σ	0	1	3	5
mean (%)	76.37	76.90	76.68	75.06
std	6.04	5.72	5.73	5.40

Tab 4.3 choice of Gaussian filter standard deviation σ

Several combinations of InD and OutD have been tested. In this case, the best global performance is obtained for InD $= -5$ and OutD $= 15$.

	OutD	5	10	15	20	25	30
InD = -20	mean (%)	75.10	76.59	76.91	76.90	76.90	76.90
	std	7.54	5.99	5.72	5.72	5.72	5.72
InD = -15	mean (%)	75.10	76.59	76.91	76.90	76.90	76.90
	std	75.10	76.59	76.91	76.90	76.90	76.90
InD = -10	mean (%)	75.15	76.64	76.89	76.88	76.88	76.88
	std	7.47	5.84	5.72	5.72	5.72	5.72
InD = -5	mean (%)	75.63	76.86	77.15	77.14	77.14	77.14
	std	6.87	5.54	5.48	5.48	5.48	5.48

Tab 4.4 choice of inside and outside search distance

It can be seen that ALL_GDT promoting any directions gives the best results.

	POS_GDT	NEG_GDT	ALL_GDT
mean (%)	73.64	71.88	77.15
std	6.83	7.17	5.48

Tab 4.5 choice of promoting directions of gradient based cost function

4.1.6 Cost function evaluation

We also will evaluate the segmentation performance of all the three cost functions on the T2 MRI database. For the model based cost functions, when one volume is segmented, the other 32 cases are used to generate the model.

In the case of shape probability-based cost function, segmentation result depends on the parameter σ_m. The segmentation on 7 volumes with σ_m from 0 to 10 is tested at a first stage, and we found that $\sigma_m = 8$ can obtain the best performance.

The mean and standard deviation of volume overlaps obtained for all the 33 data are shown in Fig 4.8. The global performance of all 33 cases is shown in Tab 4.6.

Cost Function	Gradient	Shape Probability Model	Gradient Profile Model
mean volume overlap (%)	77.15	76.71	74.88
std	5.48	6.17	6.93

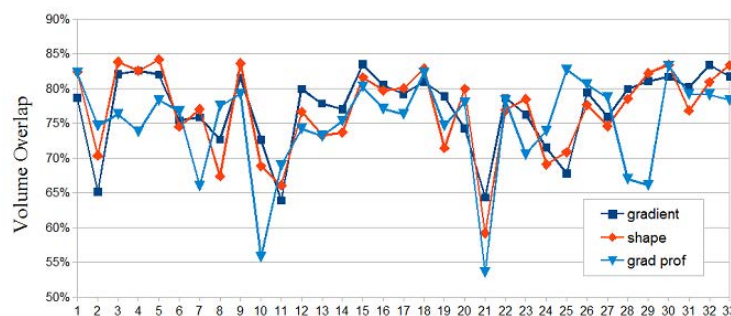**Tab 4.6** global performance of different cost functions

Fig 4.8 volume overlaps of all 33 cases with different cost functions

On Tab 4.6, it can be seen that, comparing to the use of the single gradient-based cost function, the use of a shape probability decreases a bit the global performance. Fig 4.8 shows that the shape probability can slightly increases the overlap in some cases, but globally gives less performing results.

Gradient profile model-based cost function also seems to be less performing with lower global volume overlap (Tab 4.6). In more detail, we can see on Fig 4.8 that the gradient profile model-based cost function gives some high performance increasing in some cases (e.g. cases 8, 11, 25) but also some really performance decreases (e.g. case 10). In fact, the assumption of a Gaussian distribution of the profiles is not always pertinent. Moreover, T2 MRI prostates have a high variability in texture. Tumors may appear a hypo-intense and at different locations, mainly in the peripheral zone whose gray level is high in the healthy part of the prostate and can modify the gradient profiles. Thus, the gradient profile model built from these T2 MRIs has difficulties to separate the prostate boundary between surroundings and the inside of the prostate.

The local gradient cost function that only looks for the strong energy of the boundary is more robust. In the following work, we will only use gradient based cost functions.

4.2 Multiple objects OSD based prostate segmentation

In the previous section, we proposed a T2 MRI prostate surface segmentation scheme based on Optimal Surface Detection (OSD). Globally, the single OSD method can give relatively good results but with some weaknesses, especially on the base and apex. Generally, the false definition of surface on the base and apex is because there, the prostate is imaged on slices parallel to the surface with high partial volumes. Other problems happen near the surrounding organs like the bladder and the rectum. In these areas, the intensities at the prostate surface are closed to these of the surrounding organs. And sometimes, these organs may mutually influence the shape of each other. In this section, a joint multi-objects method (Song, Liu et al. 2010) is introduced in the segmentation scheme. In the multiple objects OSD method, the information of the several organs is competing in order to find the more probable surfaces.

The overall framework of the multiple OSD segmentation is the following:
1) An initial surface mesh is built for each organ
2) Graphs are built for all the organs. These graphs will share some common nodes at the same location. Some competition constraints will be set at these nodes.
3) Graph cut will be used to estimate the surfaces of all the graphs
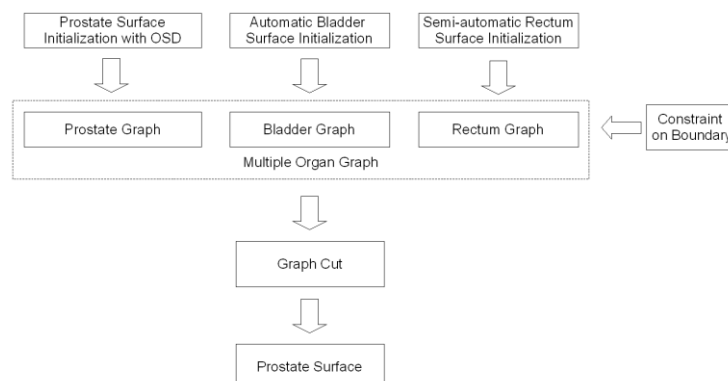4) We keep the prostate surface as segmentation result.

Fig 4.9 framework of the multiple objects OSD segmentation

4.2.1 Initialization of bladder

The bladder is a distensible organ whose shape changes continuously according the amount of collected urine and the position of the surrounding organs. It is placed superior to the prostate base, but sometimes can literally envelop the upper part of the prostate. The variability of the bladder makes it difficult to use a shape model.
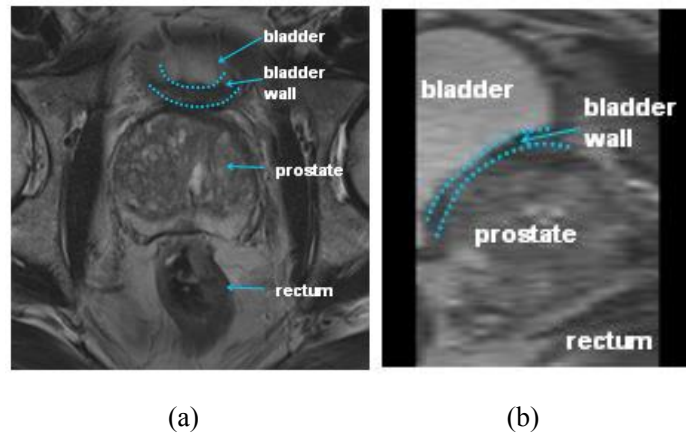
(a)   (b)
Fig 4.10 Prostate and its surrounding organs in T2 MRI

In T2 MRI, the urine is seen as a hyper-signal, while the bladder wall itself presents a hypo-signal with values similar to the prostate capsule (Fig 4.10). In 2D, the wall thickness can appear differently on the several slices, especially when the bladder is tangent to the slice as in (Fig 4.10 a).
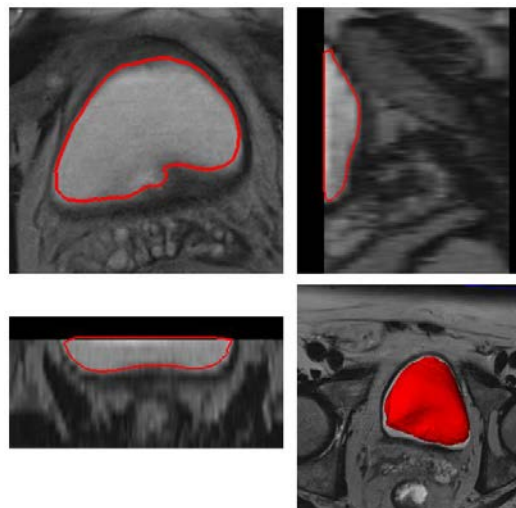
Fig 4.11 a rough segmentation on bladder to obtain initial mesh

An initial bladder segmentation framework based on deformable model has been introduced in (Garnier, Ke et al. 2011). An initial point inside the bladder is located

automatically using some geometrical (location of the bladder with respect to those of the prostate) and image (hyperintensity of the urine) features. Centered on this point, an initial mesh shaped as a small ellipsoid surface is built. The combination of inflation and internal forces, locally adapted according to the gray levels, allow deforming the mesh toward the bladder inner boundaries while overcoming the leakage issues that can occur at weak edges (Fig 4.11).

4.2.2 Initialization of rectum

A precise location of the rectum in therapy is absolutely necessary in order to avoid fistula near the prostate. The rectum has a globally curved form with a wide variability in shape, which depends on its filling and the position of the surrounding organs. In T2 MRI, if the rectal wall presents a relatively low signal, the materials inside can be totally inhomogeneous in shape and values from hypo-signal (gaz) to higher gray level values.

(a)   (b)   (c)
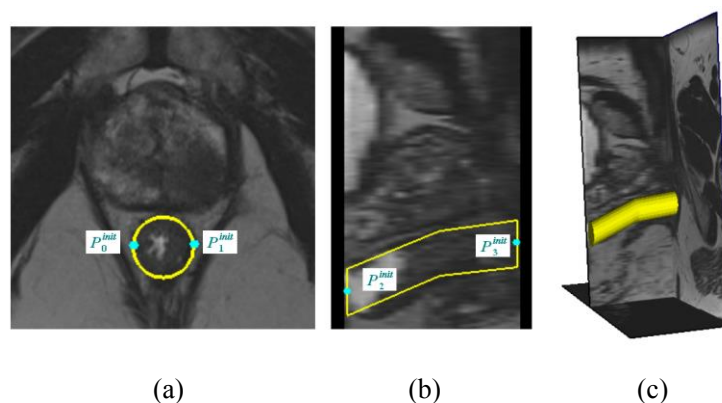
Fig 4.12 Initialization of rectum surface mesh

Because any automatic segmentation method applied on the rectum gave a robust result, we decided to adjust interactively a fast 3D broken tubular model to the data. On a sagittal slice or on a axial slice centered on the prostate, the urologist or radiologist selects two points (P_0^{init} and P_1^{init}) on the lateral diameter of the rectum:. These two points give the rectum central tabular section (position and diameter, Fig 4.12 a). Then the user defines 2 other points in the middle of the rectum (P_2^{init} and P_3^{init}): in the front and in the back of the prostate. These two points give the axes directions of the broken tube (Fig 4.12 b).

4.2.3 Initial mesh resampling

With our previous work, we have the initial meshes of prostate, bladder and rectum. Meanwhile, interacting areas, where the meshes of prostate and of the neignbor organs are closed enough, are estimated before graph construction.
Interacting Area
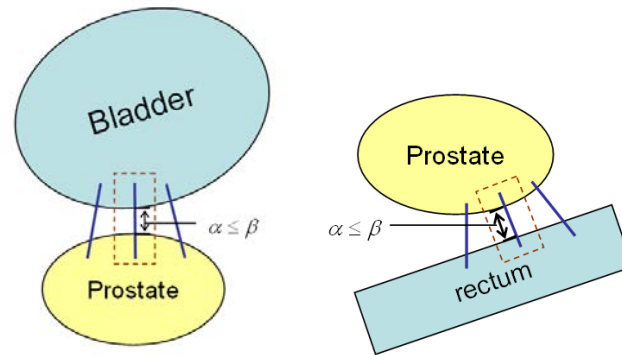
Fig 4.13 The definition of interacting area. The blue line is ray oriented along normal of prostate mesh vertex. When the distance between vertex and surrounding surface mesh is less than a threshold ($\alpha \leq \beta$), the surrounding area (brown dash line surrounded) is defined as interacting area.

For each vertex i of the prostate mesh, a ray oriented along the normal $\mathbf{r}_i$ (see equation (23)) is cast until it crosses the neighbor organ mesh. This gives the distance from vertex i to the neighbor organ mesh (Fig 4.13). When the distance is less than a defined threshold (20 voxels for prostate and 15 voxels for rectum), the vertex i and the ray intersection point with the neighbor surface belong to an interacting area. In this area, some special constraint will be defined to avoid a surface conflict in the segmentation.

In interacting areas, the vertexes of the neighbor organ surface mesh, will be resampled because:
- The surface meshes of the prostate and the neihgbor organs can overlap each other (the neighbor mesh inside the prostate).
- To build a multi-objects graph, the vertex of prostate mesh should have a corresponding vertex on the neighbor organ mesh. This vertex pair will be used to build a common nodes column between the two meshes during the graph construction.

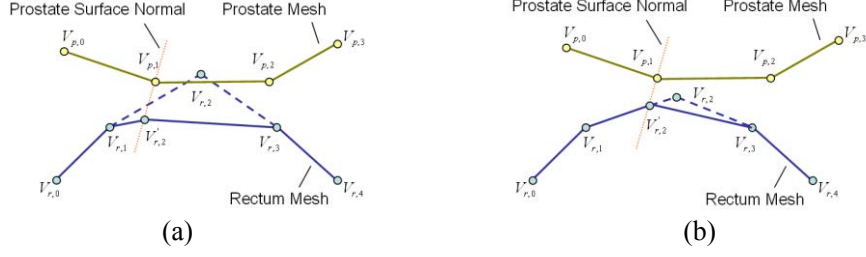**Fig 4.14** Resample process in interacting area (rectum mesh for example): (a) replacement of conflict vertexes on the surrounding organ surface mesh, (b) modify vertex on surround organ to build corresponding vertex pair

The solutions of these situations are similar: on the neighbor organ, we will define the new vertexes along the prostate surface normal, and delete the old vertexes of the surface. In the situation of a surface overlapping (Fig 4.14 - a), we will delete the vertex inside the prostate mesh and define a new vertex along the prostate surface normal. In the other situation, we define the point of intersection between the prostate surface normal and the neighbor organ surface as the new vertex ($V_{r,2}^{'}$ in Fig 4.14 b), and delete the closest vertex ($V_{r,2}$ in Fig 4.14 b). The new vertex of the neighbor organ mesh is given by:

$$V_r^{'} = V_p + \alpha \bullet \mathbf{r}_p \tag{39}$$

here $V_r^{'}$ is the new vertex of surrounding organ mesh, V_p is the closest vertex on the prostate mesh, $\mathbf{r}_p$ is the surface normal defined in (23). In the case of mesh overlapping, α is defined by the end user as the minimal distance between two surfaces on this area (usually $\alpha = 1$); otherwise, α is the distance between vertex V_p and surrounding organ surface.

4.2.4 Multiple objects OSD

In the previous sections, we showed how to obtain the initial meshes of prostate and the neighbor organs (Fig 4.15). The resample processes not only eliminate the conflict between these surfaces, but also define the vertexes interacting areas.

The main idea of the multiple organs OSD is to build a graph for each organ from the three initial meshes. For the graphs construction we will have two cases depending whether or not the surface vertex is outside or inside an interacting area. If the surface mesh vertex is outside an interacting area, the graph is built as in section 4.1.2. If the surface mesh vertex is inside an interacting area, a new way to build the graph is used in order to integrate the spatial relationship between both surfaces:
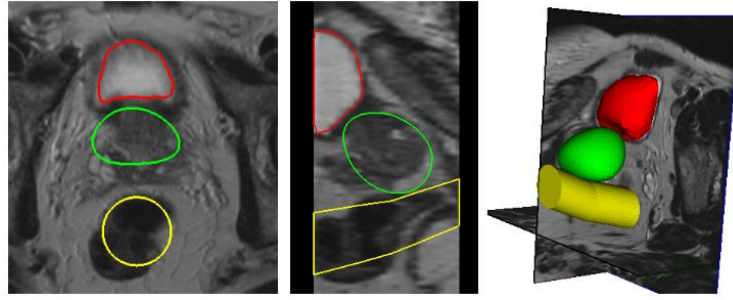
Fig 4.15 the initial surface meshes of prostate (green), bladder (red)
and rectum (yellow)

Nodes

The column of nodes is build between the vertex on the prostate and its corresponding vertex on the surrounding organ (Fig 4.16 a). More nodes of the graph are so distributed on both inside and outside of the surfaces on these columns. It has also to be noticed that according to the definition of the interacting area, the node column in this area is along the normal of the prostate surface and not along the normal of the neignbor organ surface.

In the interacting areas, the columns belonging to different graphs share the same position (Fig 4.16 a).

(a)   (b)
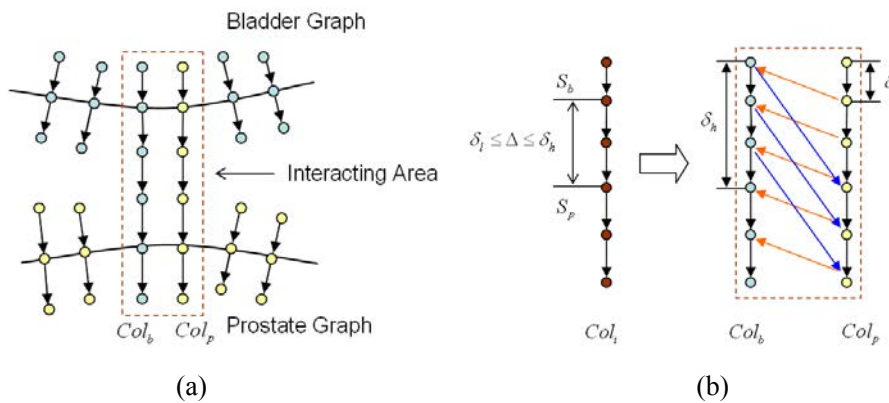
Fig 4.16 Graph construction of multiple objects OSD: (a) Nodes
columns from different graph (blue from bladder graph, yellow from
prostate graph) share the same positions, (b) Surface distance
constraint Δ defined in interacting area

Links

- Column links: They are constructed as the other column links of the graph
- Surface links: They are also constructed as described in section 4.1.2. Different surface hard shape constraint Δ can be used for each organ. This can be done by assigning a specific δ on equation (26) for each

surface.

- Interacting links: In order to prevent the leakage between surfaces in the interacting area, the distance between surfaces should be at least δ_l voxels and at most δ_h voxels. δ_l and δ_h are the surface distance constraints. Because of δ_h and δ_l, new adjacent columns links are added in the interacting area (Fig 4.16 b).

Data term weight assignment

All the nodes on the multiples objects graphs (prostate, bladder and rectum) are assigned to a weight based on the gradient function as we described in section 4.7.2. Some specific weights are defined according to a priori information.

As we know, the bladder organ is a hollow structure filled inside with urine. This make the bladder on T2 MRI image have very high intensity inside where the liquid is, but low intensity on the bladder wall. The initial bladder segmentation gives only the liquid, so the inner prostate wall. For the outer wall surface, because of the hyposignal on the wall itself and the hyposignal on the prostate surface, it is obvious that a gradient based cost function will not be able to distinguish between the bladder wall and the prostate surface (Fig 4.10). To overcome this lack of information, we add the bladder wall thickness (between 3-5 mm depending on the filling) information within the graph. All the nodes outside of the initial bladder mesh but closer to the specified wall thickness (5 mm in our case) will be considered as belonging to the bladder. This information will be encoded as weights on the links to the terminal nodes (Fig 4.17).
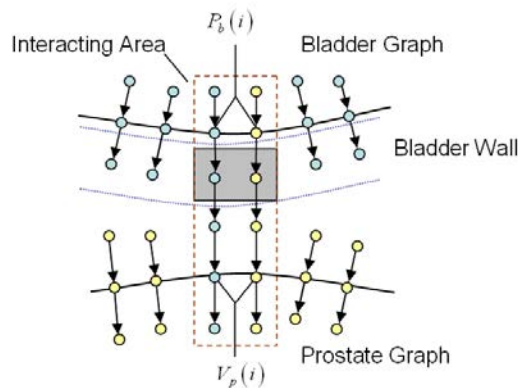

Fig 4.17 The nodes in both interacting area and bladder wall area (gray region) are assigned to a very low weights to make sure it is out of the prostate surface.

At the end, the min-cut/max-flow algorithm is applied on the common graph. The result is an estimate of the prostate, bladder and rectum surfaces.

4.2.5 Parameters adjustment

This multiple objects OSD algorithm has been tested on the 33 cases of T2 MRI database (Tab 4.1). These data with different qualities and image size ranges are used to adjust the parameters of bladder and rectum.

For the **bladder**, the following parameters are important in the segmentation:

- δ_b: the hard shape constraint from inter-column links of bladder graph, which make sure the bladder surface won't change rapidly.

- δ_{lb} and δ_{hb}: the distance constraint in the interacting area of the prostate and the bladder (Fig 4.16). They keep the distance between the surfaces between at least Δ_{lb} and at most Δ_{hb}.

- InDB and OutDB: the search distance inside and outside of bladder surface.

- POS_GDT, NEG_GDT and ALL_GDT: The promoted directions of the gradient based cost function on bladder graph.

The parameters tuning was performed as following:

δ_b and δ_{lb}, δ_{hb} are evaluated together, with δ_b from 1/4, 1/3, 1/2, 2/3 and 3/4, δ_{lb} from 1 to 5 and δ_{hb} from $\delta_{lb}+3$ to $\delta_{lb}+9$. All these parameter combinations have been tested, while the other parameters has been fixed to: InDB = -5, OutDB = 20, the gradient direction is POS_GDT. The best results (which gave the highest volume overlap with the manual designed ground truth volume) have been obtained with $\delta_{lb}=1$ and $\delta_{hb}=4$. The volume overlap with different δ_b are closed to each other. We choose $\delta_b=1/3$ to make a compromise between bladder and prostate.

InDB and OutDB have been tuned together. For InDB, we only tested the value of -5 and -10, because we tend to seek the outer wall of bladder but not inner wall. For OutDB, we tested 10, 15, 20, 25 and 30. As we expected, InDB = -5 gave a better performance than InDB = -10 and also minimized the risk of getting unwanted surface inside bladder. OutDB = 25 and 30 gave both good results, and we choose OutDB = 30 to avoid too thick bladder wall.

For the choice of the gradient promoted directions based cost function, there is a difference here compared to the situation of the prostate: for the vertices outside of the interacting area, the gradient direction must be positive POS_GDT. This is because the inside of the bladder appears with higher intensity than the outer bladder wall. In this case, a negative gradient function would promote the inner wall, but not the outer. For vertices inside the interacting area, we choose ALL_GDT which gave better performance than POS_GDT.

For the **rectum**, the same parameters are adjusted as the bladder:

- δ_r: the hard shape constraint from inter-column links of column graph, which make sure the bladder surface won't change rapidly.

- δ_{lr} and δ_{hr}: the distance constraint in the interacting area of the prostate and the rectum. They keep the distance of surfaces between at least δ_{lr} and at most δ_{hr}.

- InDR and OutDR: the search distance inside and outside the rectum surface.

- POS_GDT, NEG_GDT and ALL_GDT: The promoted directions of the gradient based cost function on rectum graph.

The parameter tuning gave:

The δ_r and δ_{lr}, δ_{hr} are evaluated together, with δ_r chosen between 1/4, 1/3 and 1/2, δ_{lr} between 1 and 5, and δ_{hr} between $\delta_{lr}+3$ and $\delta_{lr}+9$. All these combinations are tested with InDR = -15, OutDR = 30 and a gradient direction ALL_GDT on the whole rectum. The result shows that the $\delta_r = 1/4$ gave the best performance with $\delta_{lr} = 2$ and $\delta_{hr} = 9$.

For InDR, we tested -15, -20, -25 and -30, and for OutDR, we tested 15, 20, 25 and 30. The results with |InDR| and OutDR over 25 gave good performances. Considering the variance of the rectum shape in different situation and the initial mesh which is based on a rough cylinder model, we choose InDR = -30 and OutDR = 30.

Because the rectum mesh initialization is based on a rough cylinder model, the real rectum surface could be on both inside and outside of the initial mesh. So we will choose ALL_GDT for the whole rectum graph.

4.3 Evaluation

We performed the evaluation of the T2 MRI multiple objects OSD segmentation on the MICCAI Grand Challenge: Prostate MR Image Segmentation (PROMISE) 2012 training dataset (MICCAI 2012). From this dataset, we considered only the 11 T2 MR volumes acquired using an external coil. We discarded the volumes acquired using transrectal coils because the intensity inhomogeneity correction was out of our scope. A manual delineated ground truth was available for all the volumes so as recommend by the challenge we choose to evaluate the segmentation using the dice similarity coefficient (DSC) between the segmented data and the manual delineated volume:

$$DSC = 2 \cdot \frac{V_{ref} \cap V_{seg}}{V_{ref} + V_{seg}} \tag{40}$$

where V_{ref} is the reference volume and V_{seg} is the segmented volume. The DSC measures the overlap degree between V_{ref} and V_{seg}.

In the rest of the evaluation we will examine and compare 3 prostate segmentation strategies : 1) single OSD on the prostate (P), 2) multiple objects OSD using the prostate and the bladder information (P&B) and 3) multiple objects OSD using the prostate, the bladder and the rectum information (P&B&R)

We calculated the mean and median DSC of the different results obtained on the PROMISE training data (Tab 4.7). The result shows that, our methods gave almost the same level performance as the best competitor in MICCAI Grand Challenge at that time (Vincent, Guillard et al. 2012).

It should be noticed that, we do not have exactly the same condition as (Vincent, Guillard et al. 2012) in Tab 4.7: we trained our parameters by using the 33 T2 MRI database, but not on the "Leave One Out Cross Validation" (LOOCV) from the MICCAI Grand Challenge training data set. And we only segmented the cases using external coil to avoid intensity inhomogeneity of volume.

	Mean DSC	Median DSC
Single OSD	0.8828 (0.02)	0.8814
Mutiple object OSD (P&B)	0.8862 (0.02)	0.8833
Mutiple object OSD (P&B&R)	0.8884 (0.02)	0.8870
Vincent, et al	0.88 (0.03)	0.89

Tab 4.7 mean and median DSC of PROMISE training set
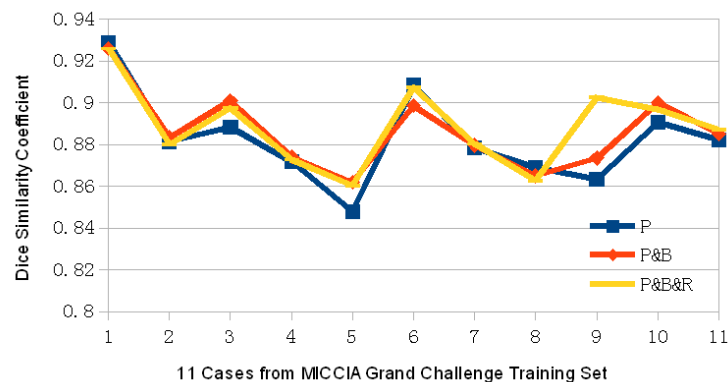

Fig 4.18 Dice similarity coefficients of all cases for single OSD and multiple objects OSD: P (blue) gives single OSD segmentation result with only the prostate information; P&B (red) gives multiple objects OSD segmentation result with prostate and bladder information; P&B&R (yellow) gives multiple objects OSD segmentation result with prostate, bladder and rectum information

Fig 4.18 shows the specific Dice similarity coefficient for each case. We can notice that in most of the cases, the multiple objects OSD segmentation gave better performance than the single OSD segmentation. It can also be seen that when the rectum is incorporate in the OSD scheme, the performance is slightly increased.

Globally the gain on the OSD could be seen as relatively low. But if we look qualitatively, our segmentation results in more details, multiple OSD estimates surfaces are closer to the real topology between the organs. The prostate-bladder OSD segmentation prevents the leakage of the prostate surface to the bladder region (an example is given, Fig 4.19 a-b). The prostate-bladder-rectum OSD segmentation avoids the overgrowing of the prostate surface in the apex area near the rectum (Fig 4.19 c-d).

Many factors may affect the accuracy of the segmentation in our method. One of the factors is the accuracy of manual defined points used for the initialization, especially on the apex and base areas. Because the prostate and neighbor organs overlap in these areas, and these organs have intensities similar to these of the prostate surface, the manual point location will decide the segmentation qualities. Fig 4.20 gives the DSC of base, apex and center part of prostate. Obviously, the DSC on center part of prostate is the highest, and the most stable in all 11 cases. But on apex and base part, the qualities of segmentation are much lower, and more variable in different cases.

The variability of manual defined contours used for the validation needs also to be considered in our result. Lebesque et al. (Lebesque, Bruce et al. 1995) investigated intra-doctor variability for contouring rectum and bladder on CT images, and they found a 2.5-3% and 7-9% variation when considering rectum/bladder and rectum wall/bladder wall volumes. Garnier et al. (Garnier 2009) compared two set of surgeon defined manual contours on TRUS volume, and found that the manual volumes overlap with a coefficient between 82% and 85%. Hodge et al. (Hodge, Fenster et al. 2006) suggest to use the mean of the manual segmentations from different radiologists and/or the same radiologist at different times to reduce inter and intra-observer variations. But in our case, only one manual contour is offered as a ground truth.

During the initialization part of OSD based segmentation, only minimal interactivity (six initial points for prostate, four initial points for rectum) are used to obtain the initial surfaces of the prostate and its neighbor organs (Fig 4.1). In these initialization schemes, the interactivity level is relatively low but absolutely necessary to insert the practitioner expertise into the procedure, especially to define the location of some structures badly imaged in T2 MRI like the base and the apex or to model the form of very complex structures like the rectum.

In order to evaluate the intra-observer variance of our OSD segmentation framework, specifically, the influence of initial points' definition, we make 10 independent multiple-objects (prostate-bladder-rectum) OSD segmentations on one case. The end-user will interactively chose 10 initial points (6 points on prostate, 4 points on rectum) on each segmentation case. We calculate the dice similarity coefficients (DSC) not only on the whole gland, but also the different zones of prostate (Fig. 4.21). The results show that (Tab. 4.8), the mean DSC score of 10 segmentations is 89.71% with a standard deviation 1.23%. When investigating the influence on different zones, we find the center zone with 4 initial points give the highest segmentation accuracy and lowest standard deviation. In apex and base zone, because the T2 MR volume has low resolution in these areas, the initial points' definitions are more difficult. The segmentation accuracy is relatively good in these areas, but also shows more intra-observer variance.

(a)　　　　　　　　(b)

(c)　　　　　　　　(d)
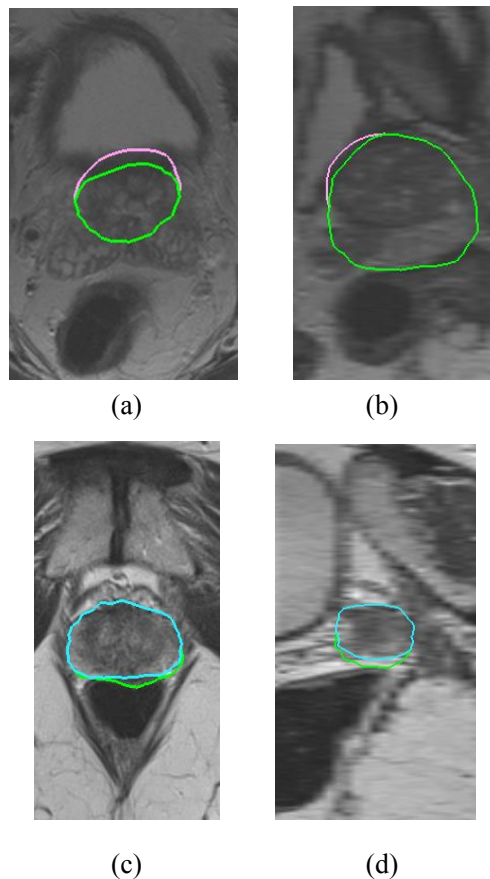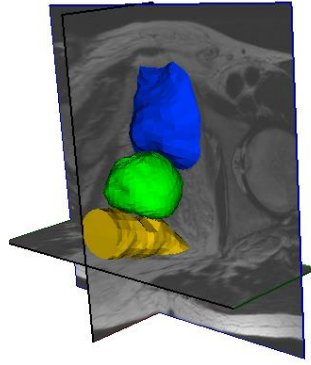
(e)

Fig 4.19 Result contours and surfaces (a - b) The result of single OSD (pink) and Prostate-Bladder OSD (green) on Axial and Sagittal plane of Case 3, (c – d) The result of Prostate-Bladder OSD (green) and Prostate-Bladder-Rectum OSD (cyan) on Axial and Sagittal plane of Case 11, (e) 3D view of the joint prostate, bladder an rectum segmentation of Case 2.
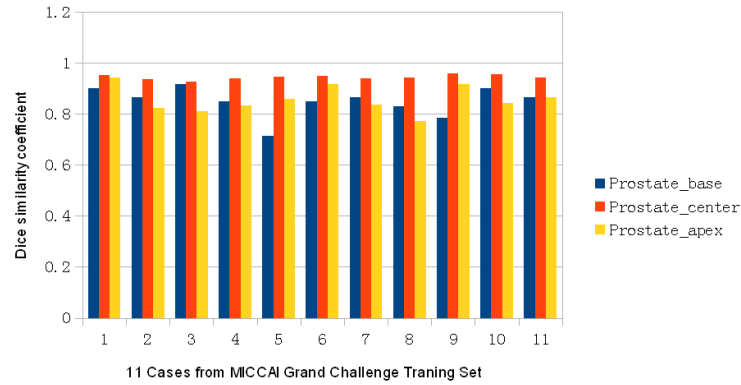

Fig 4.20 Dice similarity coefficients of all cases on different part of prostate: base (blue), center (red) and apex (yellow)
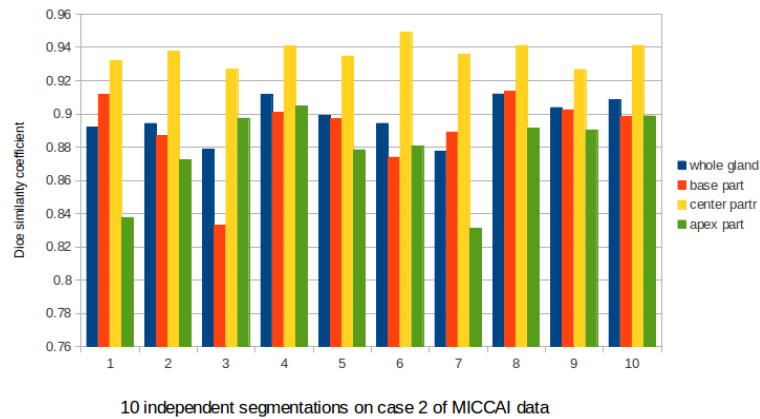

Fig 4.21 Dice similarity coefficients of one case with 10 independent segmentations: whole prostate (blue), base (red), center (yellow) and apex (green)

DSC	Whole gland	Base zone	Center zone	Apex zone
mean	0.8971	0.8906	0.9366	0.8782
std	0.0123	0.0234	0.007	0.0252

Tab 4.8 mean and standard deviation of DSC scores from 10 independent segmentations on the same case.

4.4 Conclusion

In this chapter, the optimal surface detection algorithm has been introduced to segment the prostate surface in T2 MRI volume. With a minimal level of interaction (six initial points picked manually), we are able to obtain an initial mesh of the prostate. Then, an oriented and weighted graph is constructed based on this surface, and by including data value information and shape constraints. The max-flow/min-cut graph cut method estimates the prostate surface. The parameters of the whole scheme have been trained on a 33 cases database with different image size and acquisition quality. To increase the accuracy of segmentation on the prostate apex and base areas, the information of the neighbor organs surface (bladder and rectum in our case) is encoded into the segmentation scheme. The multiple objects OSD segmentation allows us to build a "graph" including all these three organs. Some anatomical and topological information (distance between surfaces, bladder wall thickness) are encoded in these joint graphs. The competition between the surfaces of the three organs will refine the prostate surface estimation near the bladder wall and or on the rectum area.

We evaluated our method on 11 cases from the MICCAI Grand Challenge PROMISE data set, and we found that our segmentation scheme have the same level of performance as the best competitor in this challenge at that time. The result shows that OSD could segment the prostate on T2 MRI relatively accurately and that multiple objects OSD can improve the performance of this segmentation.

When investigate the inter-observer variance of OSD segmentation, we noticed that the segmentation in center part have higher accuracy and lower standard deviation; while in apex and base area, the accuracy is more sensitive to the initial points' definitions. In real surgery case, these initial points are given by surgeon with expertise. We have reason to believe that their expertise will be helpful to improve the accuracy in apex and base zone.

This segmentation scheme on T2 MRI allows us to estimate the surface of the prostate which will be used in a surface-to-surface registration scheme between ultrasound images and T2 MRI.

Chapter 5: Surfaced based registration: a preliminary work

In HIFU therapy, the HIFU device probe is not only used to generate the high intensity focused ultrasound to destroy the tumor, but also is used to scan the prostate gland to generate transrectal ultrasound (TRUS) images. TRUS is used to plan and guide the therapeutical beams. But, because the TRUS images are mainly composed by speckle (Fig 5.1 a), it is hard to identify the tumor from the normal regions. On the other side, the T2 MRI, with high resolution details, could offer the information about the prostate tissues as well as the tumor location (Fig 5.1 b). The registration process could map this information from T2 MRI volume to the TRUS volume, to guide the HIFU therapy.

(a)   (b)
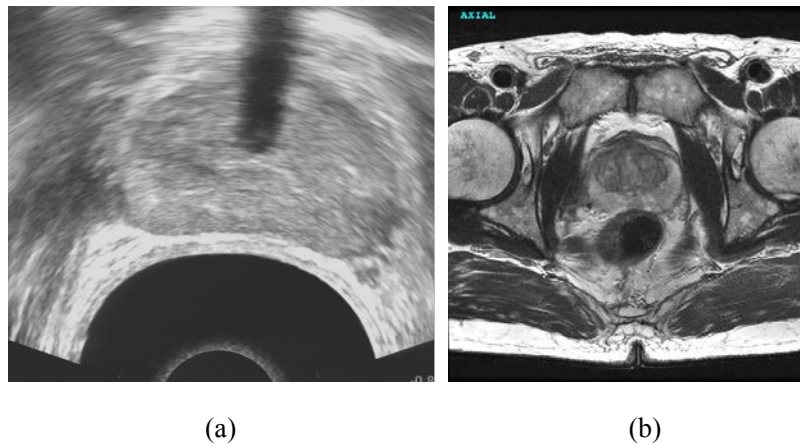
Fig 5.1 (a) TRUS image of the prostate (b) T2 MRI of the prostate.

With the multi-objects OSD segmentation scheme described in chapter 4, the prostate surface can be obtained from a T2 MRI volume. The prostate of the surface on TRUS can also be obtained by OSD (Garnier, Bellanger et al. 2011). A surface based registration can now be applied to register the two surfaces. According to Audette et al. (Audette, Ferrie et al. 2000), surfaces usually provide more redundancy than landmarks, and the redundancy could be an advantages for characterizing non-rigid motions or deformations. Furthermore, a surface-based approach is usually less affected than volume-based one if the information acquired by the two modalities of interest overlap only partially.

In this chapter, we will propose a preliminary work about TRUS/T2 MRI prostate surface-based registration scheme. In order to validate the feasibility of this approach,

we will apply this registration method to real prostate images volumes acquired on the same patient using T2 MRI and TRUS obtained on the Ablatherm device.

5.1 Registration and fusion scheme

As discussed in chapter 2, the prostate is deformed between the pre-operative T2 MRI acquisition and the peroperative US acquisition (transrectal coil in MRI in some cases, therapy probe size, balloon filling or effect of the therapy). A surface-to-surface elastic registration scheme must be considered. In this scheme, the surface of the MRI data will be adjusted on the US surface. An elastic registration scheme is generally decomposed into 2 steps:

- **Rigid registration** between the 2 surfaces in order to find the global transformation (translation, rotation, scale) between the 2 volumes.
- This global transformation is then used as the initial position of the **elastic registration**. The result of this registration step will be a 3D deformation field which adjusts the MRI surface to the US one.

The previous registration steps are then used for the fusion. The information contained in the T2 MRI volumes (gray level, tumor position, annotations …) can now be transferred to the US volume by using the global transformation matrix and the 3D deformation field estimated in the two registration steps. The overall framework can be seen on Fig 5.2
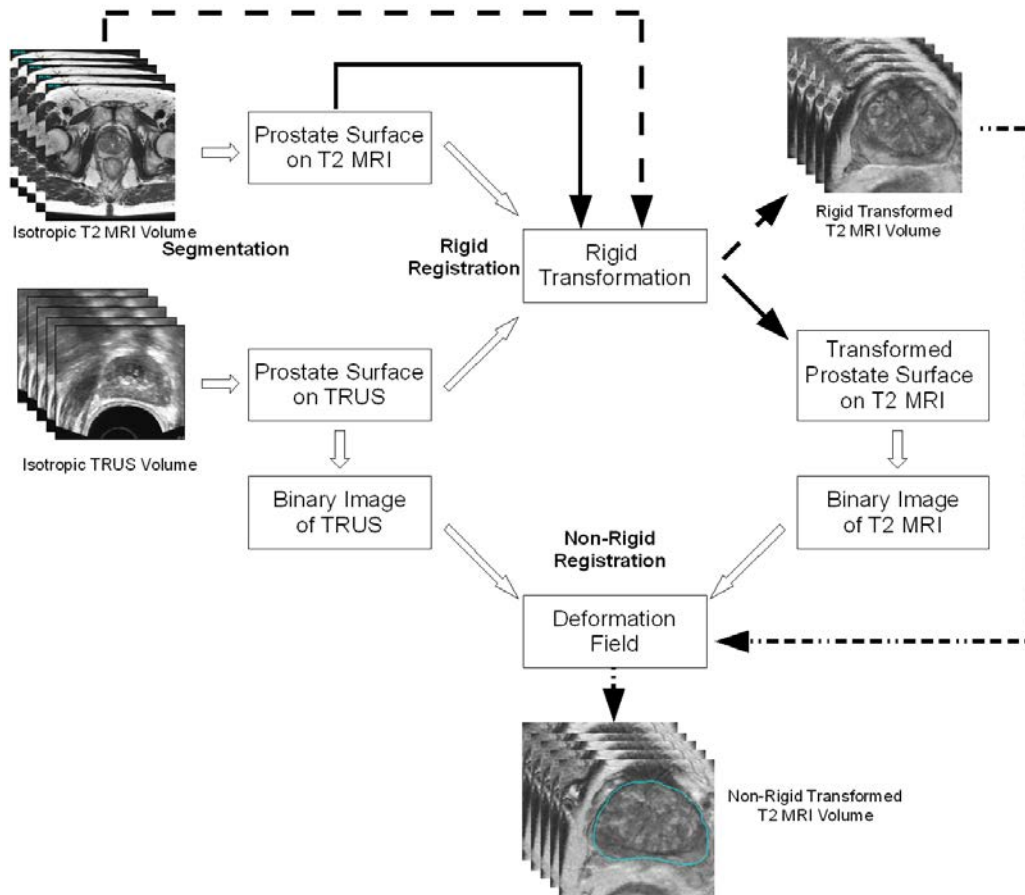
Fig 5.2: The Complete TRUS-MRI registration process by using
surface based registration technique.

5.1.1 Rigid transformation

As we noticed in Fig 5.1, the prostate regions in TRUS and T2 MRI not only have different shapes, but also have a different orientation, size and location in the 3D volumes. A rigid registration must be used to align the prostate surfaces and regions from these different image modalities. This step could offer an initial statement for the elastic registration and accelerate the whole registration process.

The aim of the rigid registration is to find the global transformation matrix (translation, rotation and scaling) which align the 2 forms. Several global registration methods exist in the literature depending on the feature (point, line, volume …) and the similarity hypothesis (minimization of distances, same inertia moments …). Because the forms are not similar, we chose the Iterative Closest Point (ICP) algorithm (Besl and McKay 1992), which is a distance minimization method between non corresponding features. This algorithm, which aimed to first register non corresponding 3D point sets can also be used for other features.

In our case, with the OSD based segmentation, we not only obtain the segmented

surface of the prostate in TRUS and T2 MRI, but also have the surface meshes with vertexes and triangular polygons. If we consider these vertexes as surface points, we get two point sets corresponding respectively to the prostate surfaces of TRUS and MRI. These sets are used as input of the ICP algorithm (Fig 5.3).
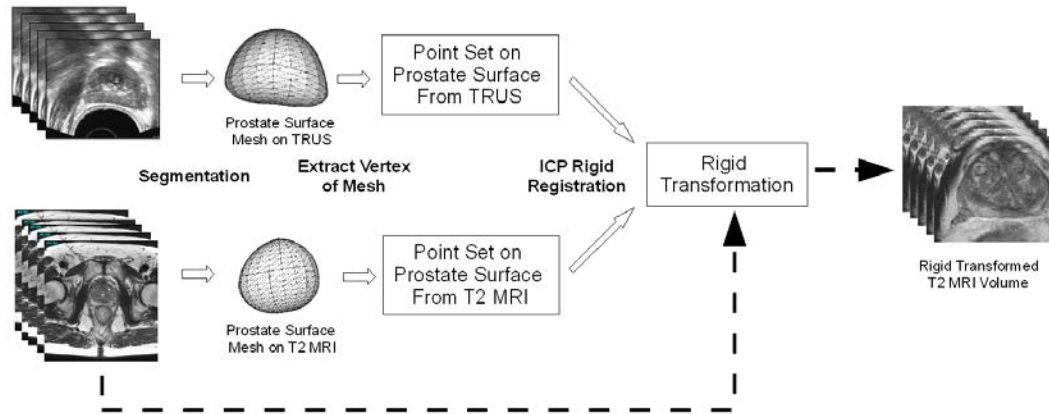
Fig 5.3: ICP based rigid registration between TRUS and T2 MRI

In our specific case, we used the *vtkIterativeClosestPointTransform* class of the VTK library (Schroeder, Avila et al. 2001). Appling the final transformation to both MRI volume and its associated prostate surface, we can obtain the registered 3D T2 MRI volume and prostate surface. This allows to align globally the MRI volume to the TRUS volume (Fig. 5.4).

Fig 5.4 showed that, the rigid registration could make the prostate volume and prostate surface from TRUS and MRI overlap in a common coordinate space. But it could not solve the problem of prostate deformation. A non-rigid registration is necessary in our work.

5.1.2 Non-Rigid registration

Global transformation matrix estimated by the previous surface-to-surface rigid registration scheme can be used to globally align the MRI volume into the US volume. But because the prostate volume is displaced and deformed during the therapy (transrectal therapy probe, edema, etc), the MRI volume should be deformed in order that the prostate in this modality fits the prostate in the US volume. The main idea is to use an elastic volume registration scheme, but based on the prostate surface information, to estimate a 3D deformation field. This 3D deformation field can then be used to transfer the MRI prostate volume information into the US volume.

(a)　　　　　　　　　(b)

(c)　　　　　　　　　(d)
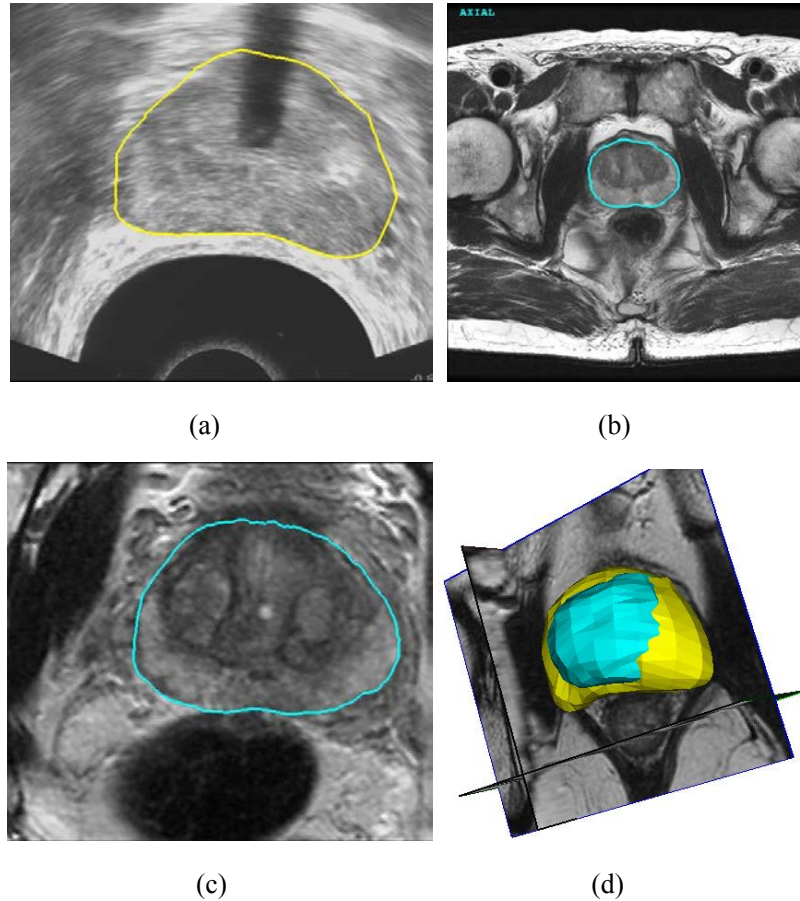
Fig 5.4: Rigid registration between TRUS and T2 MRI
(a) TRUS image with prostate contour (b) T2 MRI with prostate
contour (c) T2 MRI after rigid transformation (d) 3D view of
prostate location in TRUS and T2 MRI after transformation

It should notice that, in our case, the purpose of surface-to-surface elastic registration is not simply fitting surfaces, but more finding a 3D deformation field to deform the surface and also the inside of the prostate volume. From this constraint, we have to choose a 3D elastic volume registration scheme which uses surface information. The demons algorithm (Thirion 1998) is able to perform such a kind of registration. Thirion proposed a possible expression of demons algorithm by using only contour points, and encoded inside/outside information into symmetric forces as demons forces. We will applied an optimized symmetric forces demons algorithm based registration framework (Thirion 1998, Vercauteren, Pennec et al. 2009) to our MRI/TRUS registration problem, and match the prostate from different modalities by using surface information.

In order to speed up the registration speed we will also use a multi-resolution framework in our non-rigid registration (Bajcsy and Kovačič 1989). In this framework, both sources image and target image, are decomposed into an image pyramid. The original images are down-sampled at each level. The coarsest level registration is

obtained first, and then this registration will be improved with the finer resolution registration (Fig 5.5). The result of the elastic multi-resolution is a 3D deformation field (Fig 5.6 c). This deformation field can now be used to transfer the 3D information of the moving image to the fixed image (Fig 5.6 d).

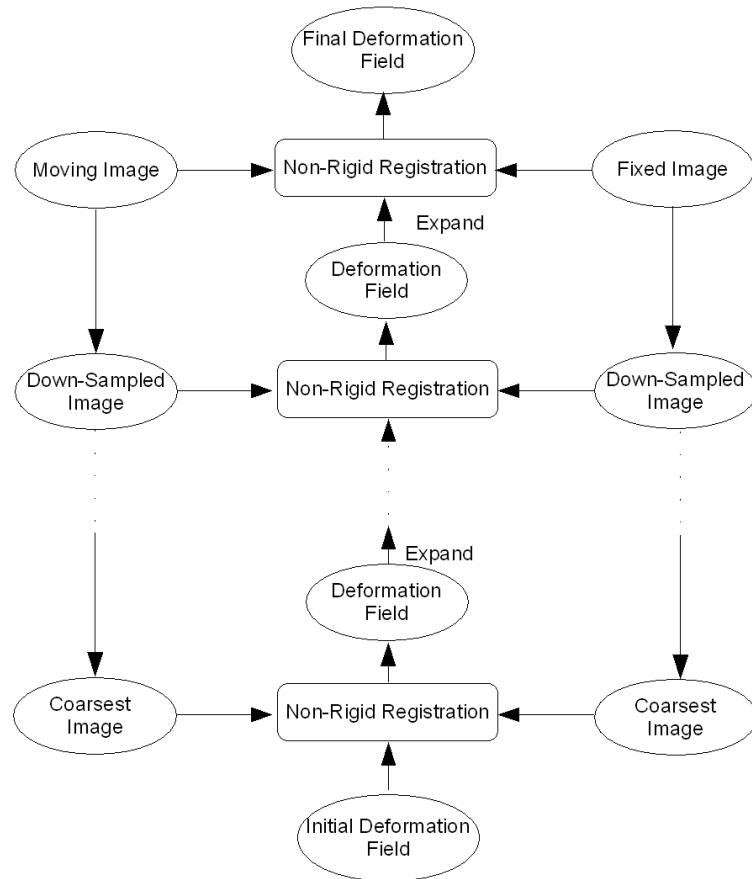**Fig 5.5**: Multi-resolution registration technique for registration

(a)   (b)   (c)   (d)
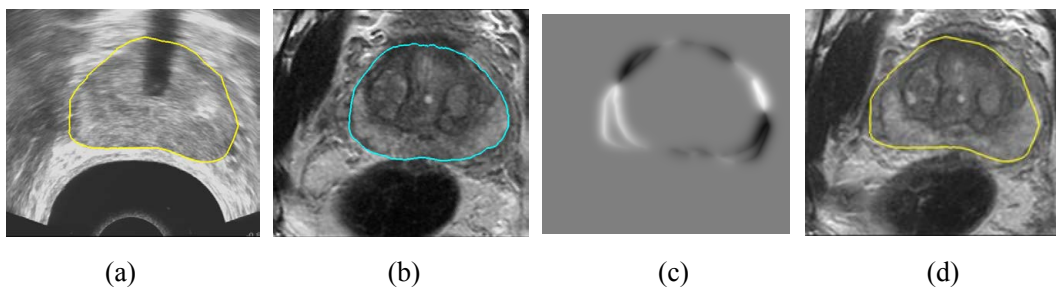
Fig 5.6 The non-rigid registration from TRUS to T2 MRI. (a) TRUS volume with prostate contour. (b) T2 MRI volume after rigid registration with prostate contour. (c) Deformation field obtained by the non-rigid registration. (d) T2 MRI volume after non-rigid registration

In our medical application framework, the question will be: how the elastic registration performed using only the prostate surface information will predict the 3D deformation inside the prostate? Most of the elastic registration methods are based on explicit deformation models (spline, anatomical mechanical model). But in the demons algorithm, the deformation is based on local diffusing model. So, in our case, the deformations imposed by the elastic registration by the surface will be diffused inside prostate.

The simplest way to convert the surface deformation into 3D deformation will be to work on binary volumes build from the prostate surfaces. The idea is to perform the demons elastic registration between the binary volume of the moving image and the binary volume of the fixed image. This method will probably give 3D deformation near the surfaces and no deformation in the center of the prostate. We will call this method as **binary model** in the rest of the Chapter.

In order to take the whole volume information into account, one solution could be to register the distance maps of the two prostate surfaces instead of the binary volumes (Dréan, Acosta et al. 2012). In this method, a 3D distance map is constructed from each prostate surface. These two maps are then normalized together. The demons elastic registration algorithm is then applied on these two normalized distance maps. In this case, we hope also that some deformation field will be estimated inside the prostate to fit the distances together. We will call this method as **normalized distance map model**.

The registration framework we will use is the following:
- Each prostate surface aligned after rigid registration is casted to a binary volume by filling. The binary volume of the TRUS is set as the fixed image, and the binary volume of T2 MRI is set as the moving image.
- If we want to use the normalized distance map model, a distance map is computed from each previous binary volume using the method described in (Maurer Jr, Qi et al. 2003). The two distance maps are then normalized as described in (Dréan, Acosta et al. 2012). The normalized distance map of the TRUS is set as the fixed image, and the normalized distance map of T2 MRI is set as the moving image.
- The demons algorithm calculates the deformation field to transform the moving image to match the fixed image. For this we used the *itkFastSymmetricForcesDemonsRegistrationFilter* class of the ITK library (Schroeder, Avila et al. 2001) in a pyramidal multi-resolution scheme.
- The original T2 MRI volume is first transformed using the global transformation matrix estimated by the rigid registration and then warped

using the deformation field estimated by the elastic registration. The information contained in the T2 MRI (gray level, automatic or manual tumor delineation) is so transferred into the peroperative US volume to help the therapy guidance (Fig. 5.7).

(a) (b) (c) (d)
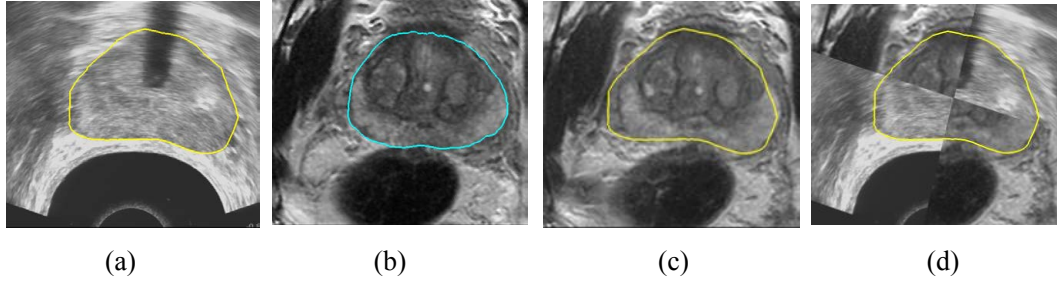
Fig 5.7 Final registration scheme: (a) US peroperative image; (b) T2 MRI volume after rigid transformation; (c) T2 MRI after elastic warping; (d) fusion of information.

5.3 Experiment and discussion

In order to validate the feasibility of the proposed framework, we applied it on a set of 10 patients treated by the Ablatherm device. For each patient we had a pre-operative T2 MRI volume and a peroperative TRUS volume recorded on the Ablatherm device during the treatment planning. The goal of these interventions was to treat the whole prostate, on all these cases a urethra resection has been performed on the prostate before the treatment to prevent the compression by this swelling and a catheter has been introduced to ensure the urine flow. The details of these volumes are shown in Tab 5.1:

Patient	T2 MRI Volume			TRUS Volume		
	Size (voxel)	S_a (mm)	S_t (mm)	Size (voxel)	S_a (mm)	S_t (mm)
HEH0054	512×512×24	0.4297	3.0005	500×470×340	0.1566	0.1566
HEH0055	512×512×24	0.4297	3.0005	500×470×308	0.1566	0.1566
HEH0056	512×512×24	0.4297	3.0005	500×470×207	0.1566	0.1566
HEH0057	512×512×24	0.4297	2.99994	500×470×261	0.1566	0.1566
HEH0061	512×512×24	0.4297	3.0004	500×470×341	0.1566	0.1566
HEH0062	512×512×24	0.4297	3.0005	500×470×275	0.1566	0.1566
HEH0065	512×512×24	0.4297	2.99994	500×470×248	0.1566	0.1566
HEH0068	512×512×24	0.4297	2.99994	500×470×247	0.1566	0.1566
HEH0070	512×512×24	0.4297	2.99994	500×470×261	0.1566	0.1566
HEH0074	512×512×28	0.4297	3.0004	500×470×322	0.1566	0.1566

Tab 5.1: The details of registration database

First of all, for all the MRI volumes an interpolation between the slices has been performed to ensure that the volume data are isotropic. The US volumes were directly isotropic. For each patient, we segmented the TRUS and T2 MRI volumes by the OSD-based prostate segmentation technique. For the TRUS volume, the segmentation has been initialized by 8 manual points. For the T2 MRI volume 10 manual initial points have been set, 6 for the prostate and 4 for the rectum in the multi-objects OSD scheme. After the segmentation scheme, we have two meshes describing the prostate surface in both TRUS and T2 MRI modalities.

The vertexes of the meshes are used in the Iterative Closest Point (ICP) based registration in order to align globally the MR surface to the US surface (Fig 5.4). A binary volume is then generated from each aligned surface. In the case we want to use the normalized distance map model, we converted the binary volumes to normalize distance maps. These 2 volumes (binary or distance map) served as input for the Demons-based elastic registration (Fig 5.6). The rigid transformation matrix and the deformation field are then used to transfer the T2 MRI pre-operative information to the peroperative TRUS volume. The information can be simply the gray level of the MRI (Fig 5.9) or annotation like the tumor (Fig 5.8).

(a)   (b)
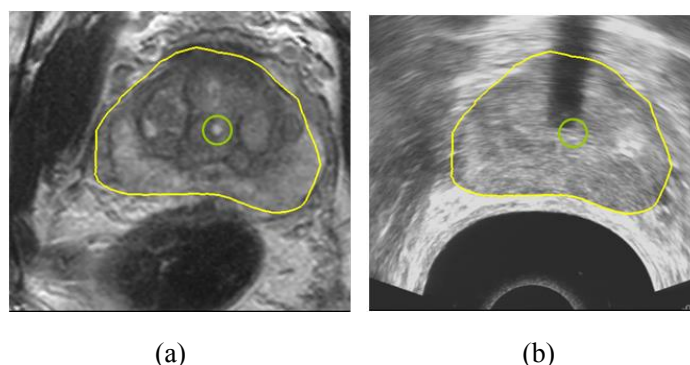
Fig 5.8 (a) T2 MRI transformed volume with a labeled location of
tumor (Simulation) (b) The location of tumor mapped from T2 MRI
to TRUS

We tested the registration process to the whole data set of the 10 different patients, and have deformed MRI volumes (Fig 5.9). With our method (segmentation and registration), we were able to register all the ten couple of clinical data. The overall method seems so to be robust. However, because we had no possibility to evaluate the final accuracy of registration, only some qualitative preliminary conclusions can be assert based on the visual examination of our results.
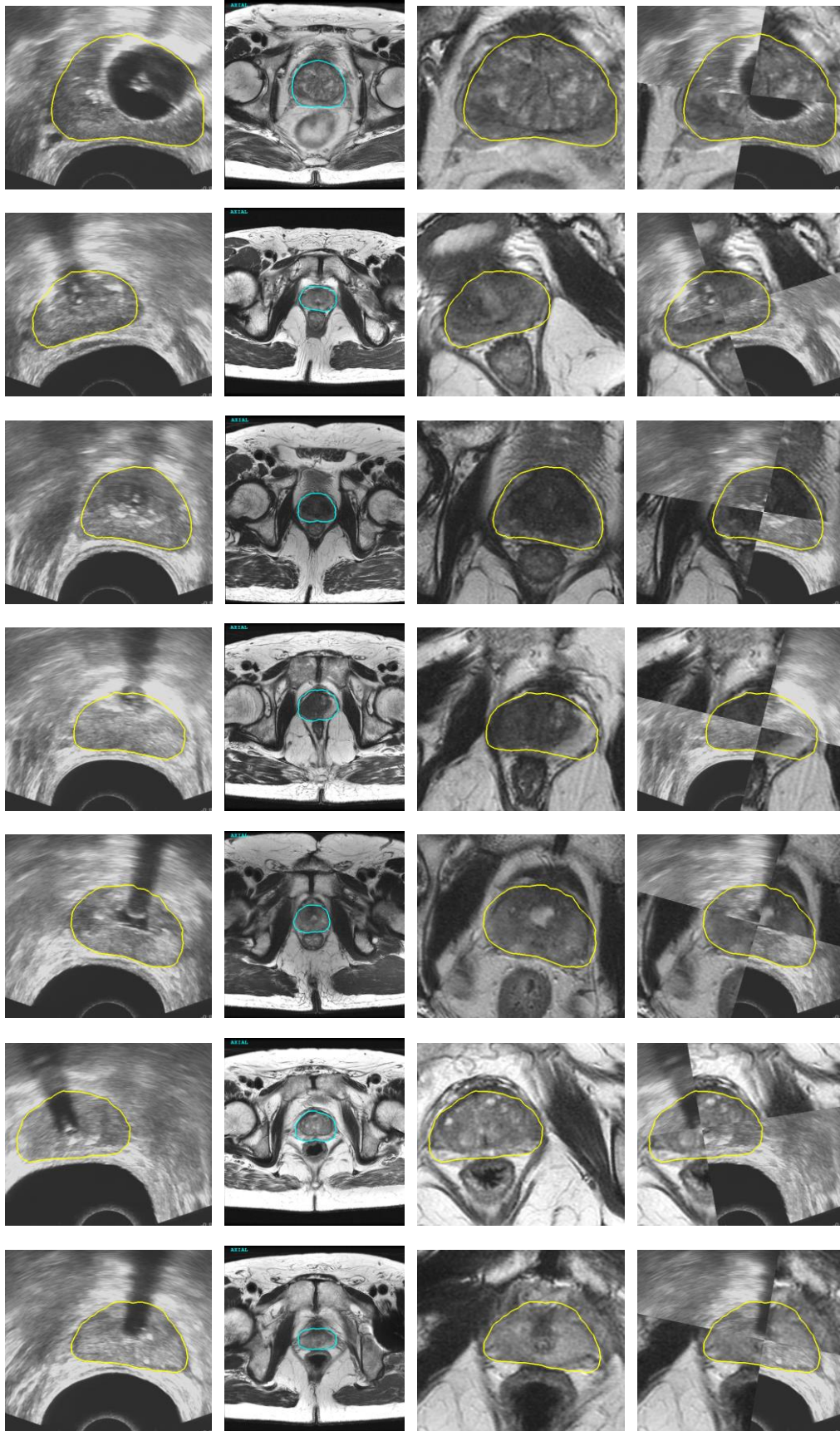
Fig 5.9 Surface-to-surface registration results: Each row show a
registration case with TRUS and MR data from the same patient;

from left to right: original TRUS image with contour, original MR
image with contour, MR image after registration with contour from
TRUS image, fusion of TRUS and MR image.

Influence of the surface segmentation

As we already discussed in chapter 4, the dice similarity coefficient (DSC) of T2 MRI segmented prostate surface is about 88%. And according to (Garnier, Bellanger et al. 2011), the volume overlap (VO) between segmented surface and ground truth on US volume is also about 81~87%. The segmentation results on both MR and US images have usually a good accuracy in the medial prostate zone but a lower accuracy at the apex and base zone. Since the whole surface-to-surface registration process is based on the segmented surfaces from the two different modalities, it is obvious to say that the registration accuracy is highly depending on the surface segmentation accuracy. But in our last work about 10 cases, we have neither expert delineated contours ground truth to evaluate the segmentation, nor gold seed points or manual designed landmarks to evaluate the registration. It is so hard to analyze the influence of the surface segmentation accuracy in the overall registration process. We can only give some registration results in which the segmented surfaces are obviously bad (Fig 5.10). But we think that in HIFU therapy, the experienced surgeon can discard these poor segmentations to avoid wrong registrations.
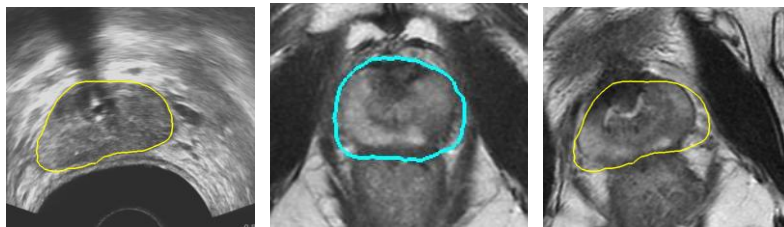
Fig 5.10 registration result with bad MR contours

Influence of the deformation field estimation model

In order to point out the influence of the deformation field estimation model (binary model or normalized distance map model), we performed a simple test to compare the inner deformation of the prostate. Some spherical areas were labeled in the MR image (Fig 5.11 a). We performed the elastic registration between MRI and US using the binary model and the normalized distance map model. The MRI information is then warped according to the estimated 3D deformation field. Fig 5.11 shows the results after warping.

We can notice that, the registration with binary model is able to deform the areas around the prostate surface, but have only little influence on the areas away from the surface (Fig 5.11 b). For example, the sphere in the middle of the prostate got any

deformation. The registration with the normalized distance map model has an influence on all the inner structures of the prostate (Fig 5.11 c). For example, the sphere in the middle of the prostate is deformed. But we can also notice that the deformation of the structures inside of the prostate can have an unnatural aspect.

<div align="center">(a)   (b)   (c)</div>
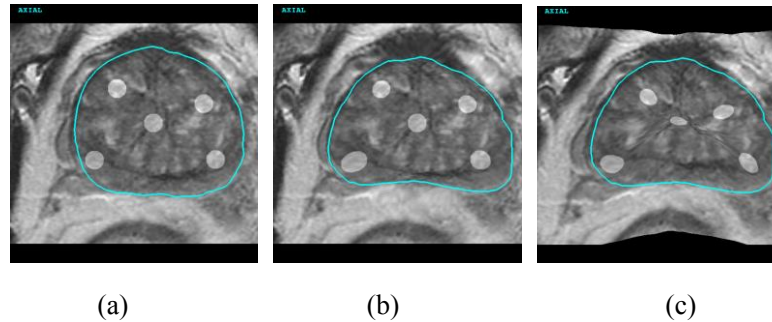
Fig 5.11 The comparison between different demon grid deformation models: (a) T2 MR image after rigid registration with circular areas; (b) Elastic registration result with binary model; (c) Elastic registration result with normalized distance map model

As a conclusion to the deformation field estimation model, we can say that the demons algorithm could give a good deformation around the surface, but we have little warranty to the inside of the prostate.

5.4 Conclusion and perspectives

In this chapter, we performed a first attempt to realize the complete registration framework to fuse the preoperative T2 MRI information to the peroperative TRUS image. This study showed the feasibility of the approach. However, this approach has to be validated more deeply.

Because we had neither the contour ground truth by expert delineations nor the volume ground truth, we were not able to validate the accuracy of the registration. More evaluations need to be performed with more specific criterions, such as annotated prostate zones, or landmarks visible in both modalities as gold seed points. Furthermore, if our method can give realistic results near the prostate surface, we have any warranty on the deformation inside the prostate. Other deformation models, like spline based, anatomical mechanical model …, should be investigated and evaluated according to some ground truth to increase the accuracy of registration inside the prostate.

Finally, according to our medical application, our elastic registration method is able to give a first estimate of the tumor location in the TRUS image. Even if this

location has some incertitude, it could be used in a focal therapy but with some security margins around the reported tumor location.

Chapter 6: Conclusion and future works

6.1 Conclusions

HIFU therapy is an efficient treatment for prostate cancer. The HIFU device probe is not only able to generate precise focused ultrasound waves to treat accurately the tumor within prostate, but also can image the prostate with ultrasound to guide the treatment process. Because of its low sensitivity and the presence of speckle, the peroperative TRUS image can not offer enough information to locate spatially the tumor area. On the other hand, pre-operative T2 MRI with its high resolution and discrimination capability is helpful to locate the tumors within the prostate. The fusion by registration of the preoperative T2 MRI information into the peroperative TRUS image becomes an important issue in HIFU therapy. In this thesis, we tried to solve the registration problem by two different strategies: intensity-based registration and feature-based registration.

For intensity-based registration, one of the problems is that the ultrasound images rarely have uniform intensity because of the speckle distribution. We considered the speckles as a kind of texture, and proposed a moment invariants based texture descriptor to convert the texture distribution to an intensity distribution. We proved the rotation and scaling invariance of the new descriptor theoretically and practically. Moreover, we find the interesting property of moment invariants based texture descriptor: the features extracted by moment invariants with different repetitions were sensitive to regional texture information while others enhanced the boundaries between two textured regions. The features sensitive to the boundaries between two textured regions can be seen as texture "gradient" and can thus be used in segmentation techniques where the boundary information is needed, i.e. active contours, deformable models, level sets, etc. In order to demonstrate the usability of moment-invariant features, such as region and boundary information, we introduced this joint information into the min-cut/max-flow graph cut algorithm. Moment invariants are so eligible to be used to adapt techniques based on the combination on regional and boundary information to the segmentation of ultrasound images. Although we were able to convert the speckle distribution of ultrasound image to intensity distribution, we were not able to find a similar intensity/texture distribution in T2 MRI. We did not continue the intensity-based registration in our Thesis.

For feature-based registration, we intend to find some common features which could be detected in both imaging modalities. In this Thesis, we choose the prostate

surface as a common feature for the registration. The registration problem is so converted into a segmentation problem. An OSD based method was proposed to segment the prostate surface in T2 MRI from six manual defined points. Furthermore, we extend the OSD based segmentation by including the bladder and rectum information. In this multiple object OSD segmentation process, some prior knowledge, such as the thickness of bladder wall, are used to prevent the prostate surface to the bladder or rectum and so we improved the segmentation accuracy. These OSD based methods were evaluated on 33 cases from clinical T2 MRI volumes and also 11 cases from MICCAI Grand Challenge PROMISE 2012 database. Our segmentation scheme has the same level accuracy as the best competitor from this challenge.

With the OSD based T2 MRI segmentation method and the TRUS segmentation method proposed by our colleague (Garnier, Bellanger et al. 2011), we are able to extract the prostate surface in both T2 MRI and TRUS images. A surface-to-surface elastic registration is then applied to align the preoperative MRI volume to the peroperative TRUS volume. We applied the surface-based registration on 10 cases of MRI/TRUS data from different patients. This study showed the feasibility of the approach. However, this approach has to be validated more deeply.

6.2 Future works

MRI/US registration is an important research topic in the medical image processing area. In this Thesis, we introduced a moment invariants based texture descriptor for ultrasound image, proposed an OSD based prostate segmentation method on T2 MRI, and performed a surface-to-surface registration between T2 MRI and TRUS images. Several research lines can be considered:

1) The prostate surface is the only information used in surface-based registration. Meanwhile, the segmentation accuracies are various on both T2 MRI and TRUS images, especially on the apex and base area. The influence of segmentation accuracy to registration should be considered in future work.

2) The demons based elastic registration could fit the surfaces of prostate. But the inside deformation of prostate is still not clear. More evaluations need to be performed with more specific criterions, such as annotated prostate zones, or landmarks visible as gold seed points in both modalities.

3) The moment invariants showed their ability to characterize the ultrasound images. But because of the complexity of the prostate, in T2 MRI, we were not able to prove the usability of the moment invariants in an intensity-based registration scheme. A future work could be to use the moment invariants based descriptor for the registration from US to another modality of organs

which are more homogeneous.

4) The ability of the moment invariants to characterize region and also boundaries in US image should be used in other segmentation algorithm such as active contours.

References

Abbou, C.-C., et al. (2001). "Laparoscopic radical prostatectomy with a remote controlled robot." The Journal of urology **165**(6): 1964-1966.

Ahmed, H. U., et al. (2012). "Focal therapy for localised unifocal and multifocal prostate cancer: a prospective development study." The lancet oncology **13**(6): 622-632.

Aigner, F., et al. (2007). "Value of magnetic resonance imaging in prostate cancer diagnosis." World journal of urology **25**(4): 351-359.

Alexander, D. D., et al. (2010). "A review and meta-analysis of prospective studies of red and processed meat intake and prostate cancer." Nutrition journal **9**: 50-50.

Alonzi, R., et al. (2007). "Dynamic contrast enhanced MRI in prostate cancer." European journal of radiology **63**(3): 335-350.

Andriole, G. L., et al. (2009). "Mortality results from a randomized prostate-cancer screening trial." New England Journal of Medicine **360**(13): 1310-1319.

Audette, M. A., et al. (2000). "An algorithmic overview of surface registration techniques for medical imaging." Medical Image Analysis **4**(3): 201-217.

Ayala, A. G., et al. (1989). "The prostatic capsule: does it exist?: Its importance in the staging and treatment of prostatic carcinoma." The American journal of surgical pathology **13**(1): 21-27.

Baade, P. D., et al. (2009). "International epidemiology of prostate cancer: geographical distribution and secular trends." Molecular nutrition & food research **53**(2): 171-184.

Badiei, S., et al. (2006). Prostate segmentation in 2D ultrasound images using image warping and ellipse fitting. Medical Image Computing and Computer-Assisted Intervention–MICCAI 2006, Springer**:** 17-24.

Bahn, D. K., et al. (2002). "Targeted cryoablation of the prostate: 7-year outcomes in the primary treatment of prostate cancer." Urology **60**(2): 3-11.

Bajcsy, R. and S. Kovačič (1989). "Multiresolution elastic matching." Computer vision, graphics, and image processing **46**(1): 1-21.

Besl, P. J. and N. D. McKay (1992). Method for registration of 3-D shapes. Robotics-DL tentative, International Society for Optics and Photonics.

Betrouni, N., et al. (2005). "Segmentation of abdominal ultrasound images of the prostate using a priori information and an adapted noise filter." Computerized Medical Imaging and Graphics **29**(1): 43-51.

Beyersdorff, D., et al. (2005). "MRI of prostate cancer at 1.5 and 3.0 T: comparison of image quality in tumor detection and staging." American Journal of Roentgenology **185**(5): 1214-1220.

Bigun, J. and J. H. du Buf (1994). "N-folded symmetries by complex moments in Gabor space and their application to unsupervised texture segmentation." Pattern Analysis and Machine Intelligence, IEEE Transactions on **16**(1): 80-87.

Bill-Axelson, A., et al. (2005). "Radical prostatectomy versus watchful waiting in early prostate cancer." New England Journal of Medicine **352**(19): 1977-1984.

Bookstein, F. L. (1989). "Principal warps: Thin-plate splines and the decomposition of deformations." Pattern Analysis and Machine Intelligence, IEEE Transactions on **11**(6): 567-585.

Boykov, Y. and G. Funka-Lea (2006). "Graph cuts and efficient ND image segmentation." International journal of computer vision **70**(2): 109-131.

Boykov, Y. and V. Kolmogorov (2004). "An experimental comparison of min-cut/max-flow algorithms for energy minimization in vision." Pattern Analysis and Machine Intelligence, IEEE Transactions on **26**(9): 1124-1137.

Bray, F., et al. (2010). "Prostate cancer incidence and mortality trends in 37 European countries: an overview." European Journal of Cancer **46**(17): 3040-3052.

Breslow, N., et al. (1977). "Latent carcinoma of prostate at autopsy in seven areas. Collaborative study organized by the International Agency for Research on Cancer, Lyons, France." International journal of cancer **20**(5): 680-688.

Bro-Nielsen, M. (1997). Rigid registration of CT, MR and cryosection images using a GLCM framework. CVRMed-MRCAS'97, Springer.

Chen, B., et al. (2011). "Combined invariants to similarity transformation and to blur using orthogonal Zernike moments." Image Processing, IEEE Transactions on **20**(2): 345-360.

Chen, C.-M., et al. (2000). "An early vision-based snake model for ultrasound image segmentation." Ultrasound in medicine & biology **26**(2): 273-285.

Chim, Y., et al. (1999). "Character recognition using statistical moments." Image and vision computing **17**(3): 299-307.

Chong, C.-W., et al. (2003). "The scale invariants of pseudo-Zernike moments." Pattern Analysis & Applications **6**(3): 176-184.

Chong, C.-W., et al. (2004). "Translation and scale invariants of Legendre moments." Pattern Recognition **37**(1): 119-129.

Cinquin, P., et al. (1995). "Computer assisted medical interventions." Engineering in Medicine and Biology Magazine, IEEE **14**(3): 254-263.

Cool, D. W., et al. (2011). Fusion of MRI to 3D TRUS for mechanically-assisted targeted prostate biopsy: system design and initial clinical experience. Prostate Cancer Imaging. Image Analysis and Image-Guided Interventions, Springer**:** 121-133.

Cootes, T. F., et al. (1994). "Use of active shape models for locating structures in medical images." Image and vision computing **12**(6): 355-365.

Cootes, T. F. and C. J. Taylor (2001). Statistical models of appearance for medical image analysis and computer vision. Medical Imaging 2001, International Society for Optics and Photonics.

Cornud, F., et al. (2006). "IRM et bilan d'extension du cancer de la prostate." Journal de Radiologie **87**(2): 228-241.

de Crevoisier, R., et al. (2009). "Image-guided radiotherapy: rational, modalities and results]." Bulletin du cancer **96**(1): 123.

Dillenseger, J.-L., et al. (2009). "Fast simulation of ultrasound images from a CT volume." Computers in Biology and Medicine **39**(2): 180-186.

Ding, M., et al. (2003). Prostate segmentation in 3D US images using the cardinal-spline-based discrete dynamic contour. Medical Imaging 2003, International Society for Optics and Photonics.

Ding, M., et al. (2006). "Needle and seed segmentation in intra-operative 3D ultrasound-guided prostate brachytherapy." Ultrasonics **44**: e331-e336.

Dréan, G., et al. (2012). Inter-individual organ-driven CT registration for dose mapping in prostate cancer radiotherapy. Biomedical Imaging (ISBI), 2012 9th IEEE International Symposium on, IEEE.

Eggener, S. E., et al. (2007). "Focal therapy for localized prostate cancer: a critical appraisal of rationale and modalities." The Journal of urology **178**(6): 2260-2267.

Esneault, S., et al. (2007). Graph cut liver segmentation for interstitial ultrasound therapy. Engineering in Medicine and Biology Society, 2007. EMBS 2007. 29th Annual International Conference of the IEEE, IEEE.

Essink-Bot, M.-L., et al. (1998). "Short-term effects of population-based screening for prostate cancer on health-related quality of life." Journal of the National Cancer Institute **90**(12): 925-931.

Flores-Tapia, D., et al. (2008). Semi automatic MRI prostate segmentation based on wavelet multiscale products. Engineering in Medicine and Biology Society, 2008. EMBS 2008. 30th Annual International Conference of the IEEE, IEEE.

Flusser, J. (2000). "On the independence of rotation moment invariants." Pattern Recognition **33**(9): 1405-1410.

Frank, S. J., et al. (2007). "An assessment of quality of life following radical prostatectomy, high dose external beam radiation therapy and brachytherapy iodine implantation as monotherapies for localized prostate cancer." The Journal of urology **177**(6): 2151-2156.

Freedman, D., et al. (2005). "Model-based segmentation of medical imagery by matching distributions." Medical Imaging, IEEE Transactions on **24**(3): 281-292.

Friedenreich, C. M., et al. (2010). "State of the epidemiological evidence on physical activity and cancer prevention." European journal of cancer (Oxford, England: 1990) **46**(14): 2593.

Gallagher, R. P. and N. Fleshner (1998). "Prostate cancer: 3. Individual risk factors." CMAJ: Canadian Medical Association Journal **159**(7): 807.

Galloway, R. and R. J. Maciunas (1990). "Stereotactic neurosurgery." Critical reviews in biomedical engineering **18**(3): 181.

Garnier, C. (2009). Segmentation de la prostate pour la thérapie par Ultrasons Haute Intensité guidée par l'image, Université Rennes 1.

Garnier, C., et al. (2011). "Prostate segmentation in HIFU therapy." Medical Imaging, IEEE Transactions on **30**(3): 792-803.

Garnier, C., et al. (2011). Bladder segmentation in MRI images using active region growing model. Engineering in Medicine and Biology Society, EMBC, 2011 Annual International Conference of the IEEE, IEEE.

Gerst, S. R., et al. (2005). "The importance of MRI evaluation in the preoperative work-up of prostate cancer." Nature Clinical Practice Urology **2**(11): 565-571.

Ghanei, A., et al. (1998). "A 3D deformable surface model for segmentation of objects from volumetric data in medical images." Computers in Biology and Medicine **28**(3): 239-253.

Ghorbel, F., et al. (2006). "Image reconstruction from a complete set of similarity invariants extracted from complex moments." Pattern Recognition Letters **27**(12): 1361-1369.

Ghose, S., et al. (2012). "A survey of prostate segmentation methodologies in ultrasound, magnetic resonance and computed tomography images." Computer Methods and Programs in Biomedicine.

Gleason, D. and G. Mellinger (1974). "the Veterans Administration Cooperative Urological Research Group: Prediction of prognosis for prostatic adenocarcinoma by combined histological grading and clinical staging." J Urol **111**(4): 58-64.

Gong, L., et al. (2004). "Parametric shape modeling using deformable superellipses for prostate segmentation." Medical Imaging, IEEE Transactions on **23**(3): 340-349.

Gower, J. C. (1975). "Generalized procrustes analysis." Psychometrika **40**(1): 33-51.

Gupta, R. T., et al. (2013). "The State of Prostate MRI in 2013." ONCOLOGY **27**(4): 1.

Haider, M. A., et al. (2007). "Combined T2-weighted and diffusion-weighted MRI for localization of prostate cancer." American Journal of Roentgenology **189**(2): 323-328.

Haigron, P., et al. (2009). "Issues in image-guided therapy [A Look at...]." Engineering in Medicine and Biology Magazine, IEEE **28**(4): 96-98.

Hajnal, J. V., et al. (1995). "Detection of subtle brain changes using subvoxel registration and subtraction of serial MR images." Journal of computer assisted tomography **19**(5): 677-691.

Hajnal, J. V., et al. (1995). "A registration and interpolation procedure for subvoxel matching of serially acquired MR images." Journal of computer assisted tomography **19**(2): 289-296.

Hall, M. A., et al. (2012). "Imaging prostate cancer lymph node metastases with a multimodality contrast agent." The Prostate **72**(2): 129-146.

Han, J. and K.-K. Ma (2007). "Rotation-invariant and scale-invariant Gabor features for texture image retrieval." Image and vision computing **25**(9): 1474-1481.

Hankey, B. F., et al. (1999). "Cancer surveillance series: interpreting trends in prostate cancer—part I: evidence of the effects of screening in recent prostate cancer incidence, mortality, and survival rates." Journal of the National Cancer Institute **91**(12): 1017-1024.

Hodge, A. C., et al. (2006). "Prostate boundary segmentation from ultrasound images using 2D active shape models: Optimisation and extension to 3D." Computer Methods and Programs in Biomedicine **84**(2): 99-113.

Hoffman, R. M., et al. (2001). "Racial and ethnic differences in advanced-stage prostate cancer: the Prostate Cancer Outcomes Study." Journal of the National Cancer Institute **93**(5): 388-395.

Holden, M. (2008). "A review of geometric transformations for nonrigid body registration." Medical Imaging, IEEE Transactions on **27**(1): 111-128.

Hu, M.-K. (1962). "Visual pattern recognition by moment invariants." Information Theory, IRE Transactions on **8**(2): 179-187.

Hu, N., et al. (2002). Prostate surface segmentation from 3D ultrasound images. Biomedical Imaging, 2002. Proceedings. 2002 IEEE International Symposium on, IEEE.

Hu, N., et al. (2003). "Prostate boundary segmentation from 3D ultrasound images." Medical physics **30**: 1648.

Huang, X., et al. (2006). Rapid registration of multimodal images using a reduced number of voxels. Medical Imaging, International Society for Optics and Photonics.

Huang, X., et al. (2009). "Dynamic 2D ultrasound and 3D CT image registration of the beating heart." <u>Medical Imaging, IEEE Transactions on</u> **28**(8): 1179-1189.

Jemal, A., et al. (2011). "Global cancer statistics." <u>CA: a cancer journal for clinicians</u> **61**(2): 69-90.

Jin, L. and Z. Tianxu (2004). "Fast algorithm for generation of moment invariants." <u>Pattern Recognition</u> **37**(8): 1745-1756.

Kaplan, I., et al. (2002). "Real time MRI-ultrasound image guided stereotactic prostate biopsy." <u>Magnetic resonance imaging</u> **20**(3): 295-299.

Key, T. (2010). "Fruit and vegetables and cancer risk." <u>British journal of cancer</u> **104**(1): 6-11.

Khotanzad, A. and Y. H. Hong (1990). "Invariant image recognition by Zernike moments." <u>Pattern Analysis and Machine Intelligence, IEEE Transactions on</u> **12**(5): 489-497.

Kvåle, R., et al. (2007). "Interpreting trends in prostate cancer incidence and mortality in the five Nordic countries." <u>Journal of the National Cancer Institute</u> **99**(24): 1881-1887.

Ladak, H. M., et al. (2000). "Prostate boundary segmentation from 2D ultrasound images." <u>Medical physics</u> **27**: 1777.

Langer, D. L., et al. (2009). "Prostate cancer detection with multi‐parametric MRI: Logistic regression analysis of quantitative T2, diffusion‐weighted imaging, and dynamic contrast‐enhanced MRI." <u>Journal of magnetic resonance imaging</u> **30**(2): 327-334.

Lavallée, S., et al. (1997). "Computer integrated surgery and therapy: State of the art." <u>STUDIES IN HEALTH TECHNOLOGY AND INFORMATICS</u>: 239-309.

Lawson, K. A., et al. (2007). "Multivitamin use and risk of prostate cancer in the National Institutes of Health–AARP Diet and Health Study." <u>Journal of the National Cancer Institute</u> **99**(10): 754-764.

Lazzeri, M. and G. Guazzoni (2010). "Focal therapy meets prostate cancer." <u>The Lancet</u> **376**(9746): 1036-1037.

Lebesque, J. V., et al. (1995). "Variation in volumes, dose-volume histograms, and estimated normal tissue complication probabilities of rectum and bladder during conformal radiotherapy of T3 prostate cancer." International Journal of Radiation Oncology* Biology* Physics **33**(5): 1109-1119.

Leissner, K.-H. and L.-E. Tisell (1979). "The weight of the human prostate." Scandinavian journal of urology and nephrology **13**(2): 137-142.

Li, K., et al. (2004). Efficient optimal surface detection: theory, implementation, and experimental validation. Medical Imaging 2004, International Society for Optics and Photonics.

Li, Y. (1992). "Reforming the theory of invariant moments for pattern recognition." Pattern Recognition **25**(7): 723-730.

Lichtenstein, P., et al. (2000). "Environmental and heritable factors in the causation of cancer—analyses of cohorts of twins from Sweden, Denmark, and Finland." New England Journal of Medicine **343**(2): 78-85.

Lobregt, S. and M. A. Viergever (1995). "A discrete dynamic contour model." Medical Imaging, IEEE Transactions on **14**(1): 12-24.

Maes, F., et al. (1997). "Multimodality image registration by maximization of mutual information." Medical Imaging, IEEE Transactions on **16**(2): 187-198.

Maintz, J. and M. A. Viergever (1998). "A survey of medical image registration." Medical Image Analysis **2**(1): 1-36.

Makni, N., et al. (2009). "Combining a deformable model and a probabilistic framework for an automatic 3D segmentation of prostate on MRI." International journal of computer assisted radiology and surgery **4**(2): 181-188.

Mari, J.-M., et al. (2013). "Study of a dual-mode array integrated in a multi-element transducer for imaging and therapy of prostate cancer." IRBM.

Martin, R. M., et al. (2010). "Blood pressure and risk of prostate cancer: Cohort Norway (CONOR)." Cancer Causes & Control **21**(3): 463-472.

Maurer Jr, C. R., et al. (2003). "A linear time algorithm for computing exact Euclidean distance transforms of binary images in arbitrary dimensions." Pattern Analysis and Machine Intelligence, IEEE Transactions on **25**(2): 265-270.

McNeal, J. (1968). "Regional morphology and pathology of the prostate." American journal of clinical pathology **49**(3): 347.

MICCAI (2012). "MICCAI grand challenge: Prostate MR Image segmentation 2012." from http://promise12.grand-challenge.org/.

Miller, D. C., et al. (2003). "Prostate carcinoma presentation, diagnosis, and staging." Cancer **98**(6): 1169-1178.

Moore, K. L. (2013). Clinically oriented anatomy, Lippincott Williams & Wilkins.

Mukundan, R. and K. Ramakrishnan (1998). Moment functions in image analysis: theory and applications, World Scientific.

Nag, S., et al. (1999). "American Brachytherapy Society (ABS) recommendations for transperineal permanent brachytherapy of prostate cancer." International journal of radiation oncology, biology, physics **44**(4): 789-799.

Narayanan, R., et al. (2009). MRI-ultrasound registration for targeted prostate biopsy. Biomedical Imaging: From Nano to Macro, 2009. ISBI'09. IEEE International Symposium on, IEEE.

Natarajan, S., et al. (2011). Clinical application of a 3D ultrasound-guided prostate biopsy system. Urologic Oncology: Seminars and Original Investigations, Elsevier.

Noble, J. A. and D. Boukerroui (2006). "Ultrasound image segmentation: a survey." Medical Imaging, IEEE Transactions on **25**(8): 987-1010.

Ornish, D., et al. (2005). "Intensive lifestyle changes may affect the progression of prostate cancer." The Journal of urology **174**(3): 1065-1070.

Otto, K. (2008). "Volumetric modulated arc therapy: IMRT in a single gantry arc." Medical physics **35**: 310.

Pantuck, A. J., et al. (2006). "Phase II study of pomegranate juice for men with rising prostate-specific antigen following surgery or radiation for prostate cancer." Clinical Cancer Research **12**(13): 4018-4026.

Partin, A., et al. (1993). "The use of prostate specific antigen, clinical stage and Gleason score to predict pathological stage in men with localized prostate cancer." The Journal of urology **150**(1): 110-114.

Perez, C. A., et al. (1993). "Localized carcinoma of the prostate (stages T1B, T1C, T2, and T3). Review of management with external beam radiation therapy." Cancer **72**(11): 3156-3173.

Pluim, J. P. and J. M. Fitzpatrick (2003). "Image registration." Medical Imaging, IEEE Transactions on **22**(11): 1341-1343.

Raychaudhuri, B. and D. Cahill (2008). "Pelvic fasciae in urology." Annals of The Royal College of Surgeons of England **90**(8): 633.

Reynier, C., et al. (2004). "MRI/TRUS data fusion for prostate brachytherapy. Preliminary results." Medical physics **31**: 1568.

Richard, W. D. and C. G. Keen (1996). "Automated texture-based segmentation of ultrasound images of the prostate." Computerized Medical Imaging and Graphics **20**(3): 131-140.

Roche, A., et al. (1998). The correlation ratio as a new similarity measure for multimodal image registration. Medical Image Computing and Computer-Assisted Intervention—MICCAI'98, Springer**:** 1115-1124.

Rogelj, P., et al. (2003). "Point similarity measures for non-rigid registration of multi-modal data." Computer vision and image understanding **92**(1): 112-140.

Rouvière, O., et al. (2012). "Prostate focused ultrasound focal therapy—imaging for the future." Nature Reviews Clinical Oncology **9**(12): 721-727.

Saad, F., et al. (2002). "A randomized, placebo-controlled trial of zoledronic acid in patients with hormone-refractory metastatic prostate carcinoma." Journal of the National Cancer Institute **94**(19): 1458-1468.

Samiee, M., et al. (2006). Semi-automatic prostate segmentation of MR images based on flow orientation. Signal Processing and Information Technology, 2006 IEEE International Symposium on, IEEE.

Sandoval, Z. and J.-L. Dillenseger (2013). "Intensity-based similarity measures evaluation for CT to ultrasound 2D registration." IRBM **34**(4): 278-282.

Sandoval Z, D. J.-L. (2013). Evaluation of Computed Tomography to Ultrasound 2D Image Registration for Atrial Fibrillation Treatment. Computing in Cardiology. Zaragoza.

Sara Mahdavi, S., et al. (2011). "Semi-automatic segmentation for prostate interventions." Medical Image Analysis **15**(2): 226-237.

Saroul, L., et al. (2008). Prostate segmentation in echographic images: a variational approach using deformable super-ellipse and Rayleigh distribution. Biomedical Imaging: From Nano to Macro, 2008. ISBI 2008. 5th IEEE International Symposium on, IEEE.

Schröder, F. H., et al. (2009). "Screening and prostate-cancer mortality in a randomized European study." New England Journal of Medicine **360**(13): 1320-1328.

Schroeder, W. J., et al. (2001). "The Visualization Toolkit-User's Guide." Kitware, Inc.

Sciarra, A., et al. (2011). "Advances in magnetic resonance imaging: how they are changing the management of prostate cancer." European urology **59**(6): 962-977.

Seabra, J. C., et al. (2011). "Rayleigh mixture model for plaque characterization in intravascular ultrasound." Biomedical Engineering, IEEE Transactions on **58**(5): 1314-1324.

Shankar, P. (2004). "The use of the compound probability density function in ultrasonic tissue characterization." Physics in medicine and biology **49**(6): 1007.

Shen, D., et al. (2003). "Segmentation of prostate boundaries from ultrasound images using statistical shape model." Medical Imaging, IEEE Transactions on **22**(4): 539-551.

Sheng, Y. and L. Shen (1994). "Orthogonal Fourier-Mellin moments for invariant pattern recognition." JOSA A **11**(6): 1748-1757.

Singh, A. K., et al. (2008). "Initial clinical experience with real‐time transrectal ultrasonography‐magnetic resonance imaging fusion‐guided prostate biopsy." BJU international **101**(7): 841-845.

Smith Jr, J., et al. (2007). "ENDOUROLOGY & LAPAROSCOPY _." J Urol **178**: 2385-2389.

Smith, R. A., et al. (2002). "American Cancer Society guidelines for the early detection of cancer." CA: a cancer journal for clinicians **52**(1): 8-22.

Sobin, L. H. and I. D. Fleming (1997). "TNM classification of malignant tumors, (1997)." Cancer **80**(9): 1803-1804.

Song, Q., et al. (2010). Graph search with appearance and shape information for 3-D prostate and bladder segmentation. Medical Image Computing and Computer-Assisted Intervention–MICCAI 2010, Springer**: 172-180.

Spiegel, E., et al. (1947). "Stereotaxic apparatus for operations on the human brain." Science **106**(2754): 349-350.

Studholme, C., et al. (1999). "An overlap invariant entropy measure of 3D medical image alignment." Pattern Recognition **32**(1): 71-86.

Tan, N., et al. (2012). "Radical prostatectomy: value of prostate MRI in surgical planning." Abdominal imaging **37**(4): 664-674.

Tannock, I. F., et al. (2004). "Docetaxel plus prednisone or mitoxantrone plus prednisone for advanced prostate cancer." New England Journal of Medicine **351**(15): 1502-1512.

Teh, C.-H. and R. T. Chin (1988). "On image analysis by the methods of moments." Pattern Analysis and Machine Intelligence, IEEE Transactions on **10**(4): 496-513.

Thirion, J.-P. (1998). "Image matching as a diffusion process: an analogy with Maxwell's demons." Medical Image Analysis **2**(3): 243-260.

Troccaz, J. (2009). "Computer and robot-assisted medical intervention." Springer Handbook of Automation: 1451-1466.

Tsai, A., et al. (2003). "A shape-based approach to the segmentation of medical imagery using level sets." Medical Imaging, IEEE Transactions on **22**(2): 137-154.

Tuceryan, M. (1994). "Moment-based texture segmentation." Pattern Recognition Letters **15**(7): 659-668.

Uchida, T., et al. (2006). "Five years experience of transrectal high‐intensity focused ultrasound using the Sonablate device in the treatment of localized prostate cancer." international Journal of Urology **13**(3): 228-233.

van der CRUIJSEN-KOETER, I. W., et al. (2005). "Comparison of screen detected and clinically diagnosed prostate cancer in the European randomized study of screening for prostate cancer, section Rotterdam." The Journal of urology **174**(1): 121-125.

Venkateswaran, V. and L. H. Klotz (2010). "Diet and prostate cancer: mechanisms of action and implications for chemoprevention." Nature Reviews Urology **7**(8): 442-453.

Vercauteren, T., et al. (2009). "Diffeomorphic demons: Efficient non-parametric image registration." NeuroImage **45**(1): S61-S72.

Vikal, S., et al. (2009). Prostate contouring in MRI guided biopsy. SPIE Medical Imaging, International Society for Optics and Photonics.

Vincent, G., et al. (2012). "Fully automatic segmentation of the prostate using active appearance models." Medical Image Computing and Computer Assisted Intervention (MICCAI) Grand Challenge: Prostate MR Image Segmentation **7**.

Vu, N. and B. Manjunath (2008). Shape prior segmentation of multiple objects with graph cuts. Computer Vision and Pattern Recognition, 2008. CVPR 2008. IEEE Conference on, IEEE.

Wei, Z., et al. (2004). "Robot-assisted 3D-TRUS guided prostate brachytherapy: system integration and validation." Medical physics **31**: 539.

Wigle, D. T., et al. (2008). "Role of hormonal and other factors in human prostate cancer." Journal of Toxicology and Environmental Health, Part B **11**(3-4): 242-259.

Woods, R. P., et al. (1992). "Rapid automated algorithm for aligning and reslicing PET images." Journal of computer assisted tomography **16**(4): 620-633.

Woods, R. P., et al. (1998). "Automated image registration: I. General methods and intrasubject, intramodality validation." Journal of computer assisted tomography **22**(1): 139-152.

Woods, R. P., et al. (1993). "MRI-PET registration with automated algorithm." Journal of computer assisted tomography **17**(4): 536-546.

Wu, H., et al. (2004). "Watchful waiting and factors predictive of secondary treatment of localized prostate cancer." The Journal of urology **171**(3): 1111-1116.

Wu, K., et al. (2010). A preliminary study of moment-based texture analysis for medical images. Engineering in Medicine and Biology Society (EMBC), 2010 Annual International Conference of the IEEE, IEEE.

Wu, K., et al. (2013). "Prostate segmentation on T2 MRI using Optimal Surface Detection." IRBM **34**(4): 287-290.

Wu, K., et al. (2013). "Region and boundary feature estimation on ultrasound images using moment invariants." Computer Methods and Programs in Biomedicine.

Xu, D. and H. Li (2008). "Geometric moment invariants." Pattern Recognition **41**(1): 240-249.

Zaim, A. (2005). Automatic segmentation of the prostate from ultrasound data using feature-based self organizing map. Image Analysis, Springer**:** 1259-1265.

Zeegers, M., et al. (2003). "Empiric risk of prostate carcinoma for relatives of patients with prostate carcinoma." Cancer **97**(8): 1894-1903.

Zelefsky, M. J., et al. (2002). "High-dose intensity modulated radiation therapy for prostate cancer: early toxicity and biochemical outcome in 772 patients." International Journal of Radiation Oncology* Biology* Physics **53**(5): 1111-1116.

Zhan, Y. and D. Shen (2003). Automated segmentation of 3D US prostate images using statistical texture-based matching method. Medical Image Computing and Computer-Assisted Intervention-MICCAI 2003, Springer**:** 688-696.

Zhan, Y. and D. Shen (2006). "Deformable segmentation of 3-D ultrasound prostate images using statistical texture matching method." Medical Imaging, IEEE Transactions on **25**(3): 256-272.

Zhang, H., et al. (2010). Object recognition by a complete set of pseudo-Zernike moment invariants. Acoustics Speech and Signal Processing (ICASSP), 2010 IEEE International Conference on, IEEE.

Zhang, H., et al. (2010). "Construction of a complete set of orthogonal Fourier–Mellin moment invariants for pattern recognition applications." Image and vision computing **28**(1): 38-44.

Zhang, J., et al. (2002). Invariant texture segmentation via circular Gabor filters. Pattern Recognition, 2002. Proceedings. 16th International Conference on, IEEE.

Zhu, H., et al. (2007). "Translation and scale invariants of Tchebichef moments." Pattern Recognition **40**(9): 2530-2542.

Zhu, Y., et al. (2007). "A hybrid ASM approach for sparse volumetric data segmentation." Pattern Recognition and Image Analysis **17**(2): 252-258.

Zitova, B. and J. Flusser (2003). "Image registration methods: a survey." Image and vision computing **21**(11): 977-1000.

Appendix

Invariance of moment invariants

The rotation and scaling invariance of the three moment invariants can be proved mathematically (Chen, Shu et al. 2011) (Zhang, Dong et al. 2010) (Zhang, Shu et al. 2010). Here, we take *ZMIs* as an example (Chen, Shu et al. 2011):

The radial moment of order p with repetition q of image intensity function $f(r,\theta)$ is defined as (Mukundan and Ramakrishnan 1998):

$$D_{p,q}^f = \int\limits_0^{2\pi}\int\limits_0^1 r^p e^{-jq\theta} f(r,\theta) r\,dr\,d\theta, \quad j=\sqrt{-1}, \quad 0\le r\le 1, \quad p\ge 0, \quad q=0,\pm1,\pm2,\ldots$$

(41)

The Zernike moment of order p with repetition q of $f(r,\theta)$ is defined as:

$$ZM_{p,q}^f = \frac{p+1}{\pi}\int\limits_0^{2\pi}\int\limits_0^1 R_{p,q}(r) e^{-jq\theta} f(r,\theta) r\,dr\,d\theta, \quad p\ge 0, \quad |q|\le p, \quad p-|q| \ \ being \ \ even$$

(42)

where $R_{p,q}(r)$ is the real-valued radial polynomial given by

$$R_{p,q}(r) = \sum_{k=0}^{(p-|q|)/2} \frac{(-1)^k (p-k)!}{k!\left(\dfrac{p+|q|}{2}-k\right)!\left(\dfrac{p-|q|}{2}-k\right)!} r^{p-2k}$$

(43)

Let $f^{"}$ and f be two images having the same content but a different orientation (β) and scale (λ), that is, $f^{"}(r,\theta)=f(r/\lambda,\theta-\beta)$, the Zernike moment of the transformed image is given by:

$$\begin{aligned}
ZM_{q+2m,q}^{f^{"}} &\\
&= \frac{q+2m+1}{\pi}\times\int\limits_0^{2\pi}\int\limits_0^1 R_{q+2m,q}(r) e^{-jq\theta} f(r/\lambda,\theta-\beta) r\,dr\,d\theta\\
&= e^{-jq\beta}\frac{q+2m+1}{\pi}\lambda^2\times\int\limits_0^{2\pi}\int\limits_0^1 R_{q+2l,q}(\lambda r) e^{-jq\theta} f(r,\theta) r\,dr\,d\theta
\end{aligned}$$

(44)

With the definition of Zernike moment and radial moment in equation (41)，(1) and (2), we will have the relationship between them:

$$ZM_{q+2m,q}^{f}$$

$$= \frac{q+2m+1}{\pi} \times \int_{0}^{2\pi}\int_{0}^{1} \left[\sum_{l=0}^{m}(-1)^{l} \frac{(q+2m-l)!}{l!(q+m-l)!(m-l)!} r^{q+2(m-l)} \right] \times e^{-jq\theta} f(r,\theta) r dr d\theta$$

$$= \frac{q+2m+1}{\pi} \times \int_{0}^{2\pi}\int_{0}^{1} \left[\sum_{l=0}^{m}(-1)^{m-l} \frac{(q+m+l)!}{l!(q+l)!(m-l)!} r^{q+2k} \right] \times e^{-jq\theta} f(r,\theta) r dr d\theta$$

$$= \sum_{k=0}^{m}(-1)^{m-l} \frac{q+2m+1}{\pi} \frac{(q+m+l)!}{l!(q+l)!(m-l)!} \times \int_{0}^{2\pi}\int_{0}^{1} r^{q+2k} e^{-jq\theta} f(r,\theta) r dr d\theta$$

$$= \sum_{l=0}^{m} c_{m,l}^{q} D_{q+2l,q}^{f}$$

(45)

Meanwhile, the radial moments can also be expressed as series of Zernike moments:

$$D_{q+2m,q}^{f} = \sum_{l=0}^{m} d_{m,l}^{q} Z_{q+2l,q}^{f}$$

(46)

So we can make equation (45) to:

$$ZM_{q+2m,q}^{f''}$$

$$= e^{-jq\beta} \sum_{l=0}^{m} \lambda^{q+2l+2} c_{m,l}^{q} D_{q+2l,q}^{f}$$

$$= e^{-jq\beta} \sum_{l=0}^{m}\sum_{k=0}^{l} \lambda^{q+2l+2} c_{m,l}^{q} d_{l,k}^{q} Z_{q+2k,q}^{f}$$

$$= e^{-jq\beta} \sum_{k=0}^{m}\sum_{l=k}^{m} \lambda^{q+2l+2} c_{m,l}^{q} d_{l,k}^{q} Z_{q+2k,q}^{f}$$

(47)

This equation also can be written in a matrix form as:

$$\begin{pmatrix} ZM_{q,q}^{f''} \\ ZM_{q+2,q}^{f''} \\ \vdots \\ ZM_{q+2m,q}^{f''} \end{pmatrix} = e^{-jq\beta} C_{m}^{q} diag\left(\lambda^{q+2}, \lambda^{q+4}, \cdots, \lambda^{q+2m+2}\right) D_{m}^{q} \begin{pmatrix} ZM_{q,q}^{f} \\ ZM_{q+2,q}^{f} \\ \vdots \\ ZM_{q+2m,q}^{f} \end{pmatrix}$$

(48)

Applying the *ZMIs* to this transformed image f'', it can also be expressed in matrix form as:

$$\begin{pmatrix} ZMI_{q,q}^{f''} \\ ZMI_{q+2,q}^{f''} \\ \vdots \\ ZMI_{q+2m,q}^{f''} \end{pmatrix} = e^{-jq\theta_{f''}} C_{m}^{q} diag\left(\Gamma_{f''}^{-(q+2)}, \quad \Gamma_{f''}^{-(q+4)}, \quad \cdots \quad \Gamma_{f''}^{-(q+2m+2)}\right) D_{m}^{q} \begin{pmatrix} ZM_{q,q}^{f''} \\ ZM_{q+2,q}^{f''} \\ \vdots \\ ZM_{q+2m,q}^{f''} \end{pmatrix}$$

Based on the definition of Γ_f and θ_f, it can be verified that

$$\Gamma_{f'} = \lambda \Gamma_f, \quad \theta_{f'} = \theta_f - \beta \tag{50}$$

According to (48), (49), (50) and using the identity $D_m^q C_m^q = I$, we can get:

$$
\begin{pmatrix} ZMI_{q,q}^{f''} \\ ZMI_{q+2,q}^{f''} \\ \vdots \\ ZMI_{q+2m,q}^{f''} \end{pmatrix} = e^{-jq\theta_f} C_m^q diag\left(\Gamma_f^{-(q+2)}, \quad \Gamma_f^{-(q+4)}, \quad \cdots \quad \Gamma_f^{-(q+2m+2)} \right)
$$

$$
\times diag\left(\lambda^{-(q+2)}, \lambda^{-(q+4)}, \cdots, \lambda^{-(q+2m+2)} \right) D_m^q C_m^q
$$

$$
\times diag\left(\lambda^{q+2}, \lambda^{q+4}, \cdots, \lambda^{q+2m+2} \right) D_m^q \begin{pmatrix} ZM_{q,q}^f \\ ZM_{q+2,q}^f \\ \vdots \\ ZM_{q+2m,q}^f \end{pmatrix}
$$

$$
= e^{-jq\theta_f} C_m^q diag\left(\Gamma_f^{-(q+2)}, \quad \Gamma_f^{-(q+4)}, \quad \cdots \quad \Gamma_f^{-(q+2m+2)} \right) D_m^q \begin{pmatrix} ZM_{q,q}^f \\ ZM_{q+2,q}^f \\ \vdots \\ ZM_{q+2m,q}^f \end{pmatrix}
$$

$$
= \begin{pmatrix} ZMI_{q,q}^f \\ ZMI_{q+2,q}^f \\ \vdots \\ ZMI_{q+2m,q}^f \end{pmatrix}
$$

$$\tag{51}$$

The rotation and scaling invariance has been proved.

Résumé

Les travaux de cette Thèse porte sur des éléments de guidage d'une thérapie focale du cancer de la prostate par Ultrasons Focalisés Haute Intensité (HIFU). Actuellement l'IRM est la seule technique d'imagerie qui permet de localiser la tumeur dans la prostate. Par contre, la tumeur n'est pas visible dans l'échographie qui est l'imagerie utilisée pour la planification et le guidage de la thérapie. L'objectif de la Thèse est de proposer des techniques de recalage de l'IRM T2 vers l'échographie. Deux approches ont été explorées :

- une approche basée région et plus particulièrement une méthode de descripteurs de la texture en échographie basée sur des moments invariants en rotation et en échelle. Ces descripteurs sont sensibles à la distribution du speckle quelle que soit son échelle ou son orientation. Certains de ces descripteurs permettent de caractériser les régions présentant une même distribution de speckle, mais nous avons également constaté que certains autres de ces descripteurs étaient sensibles aux contours de ces régions. Cette caractéristique nous semble très utile pour les méthodes de segmentation intégrant à la fois l'information de contours et l'information de régions (contours actifs, graph cut, etc.).

- une approche basée surface. Nous avons adapté une méthode de Détection Optimale de la Surface (OSD) à la segmentation de la prostate en IRM T2. Et plus particulièrement une segmentation concurrente de la prostate, de la vessie et du rectum par OSD multi-objets. Les surfaces de la prostate extraites du volume échographique et du volume IRM T2 nous ont permis d'envisager une première tentative de recalage surface/surface par la méthode des démons.

Abstract

The work of this Thesis is focused on image guided focal therapy of prostate cancer by High Intensity Focused Ultrasound (HIFU). Currently MRI is the only imaging technique that can locate the tumor in prostate. In contrast, the tumor is not visible in the ultrasound image which is used to guide the HIFU planning and therapy. The aim of the Thesis is to provide registration techniques of T2 MRI to ultrasound. Two approaches were explored:

- Region-based registration. More particularly, we studied an ultrasound texture descriptors based on moments invariant to rotation and scaling. These descriptors are sensitive to speckle distribution regardless of the scale or the orientation. As we expected, some of these descriptors can be used to characterize regions sharing a similar speckle spatial distribution. But, we also found that some other descriptors were sensitive to the contours of these regions. This property seems very useful to adapt the classical boundary-based or mixed region/boundary-based segmentation methods (active contours, graph cut, etc.) to process US images.

- Surface-based registration approach.. We adapted the Optimal Surface Detection (OSD) method to the segmentation of the prostate in T2 MRI, Furthermore, we proposed the multiple-objects OSD which is a concurrent segmentation of the prostate, bladder and rectum. Finally we used the prostate surface extracted from the ultrasound volume and from T2 MRI in a surface-to-surface elastic registration scheme. This registration allowed us to merge the preoperative MR information in the peroperative US volume.